TWO-DIMENSIONAL METAL-INSULATOR TRANSITION

By

JUNREN SHI

Bachelor of Science
Fujian Normal University
Fuzhou, P. R. China
1993

Submitted to the Faculty of the
Graduate College of the
Oklahoma State University
in partial fulfillment of
the requirements for
the Degree of
DOCTOR OF PHILOSOPHY
May, 2002

TWO-DIMENSIONAL METAL-INSULATOR TRANSITION

Thesis Approved:

Thesis Advisor

Dean of the Graduate College

ACKNOWLEDGMENTS

I wish to express my deepest gratitude to my advisor Prof. X. C. Xie for his constructive guidance, constant encouragement, kindness and great patience. Without his guidance and collaboration, I would not have been able to finish this work.

I also would like to express my sincere appreciation to Prof. Paul Westhaus for his assistance during these years of my study at Oklahoma State University.

My appreciation extends to my other committee members Prof. T. M. Wilson and Prof. D. L. Thompson, whose encouragement has also been invaluable.

TABLE OF CONTENTS

Chapter Page

1. Introduction 1

1.1. Weak Localization and Scaling Theory of Localization 1
1.1.1. Weak Localization 1
1.1.2. Scaling Theory of Localization 3
1.2. Two-Dimensional Metal-Insulator Transition 6
1.2.1. Temperature Dependence of Resistivity 7
1.2.2. Nonlinear Effects 11
1.2.3. Scaling 11
1.2.4. Parallel Magnetic Field Effects 15
1.2.5. Measurements Other Than Resistivity 19
1.2.6. Quantum Phase Transition or Not? 21
1.3. Theory 23
1.3.1. Quantum Mechanisms 25
1.3.2. Semi-classical Theories 27
1.4. Percolation Model 28
1.4.1. Temperature Dependence of The Resistivity 28
1.4.2. Scaling and Duality 29
1.4.3. Electric-Field Dependence of The Resistivity 30
1.4.4. Effects of An In-Plane Magnetic Field 31
1.4.5. Further Works 33

2. Droplet State 34

2.1. Energetics Consideration 35
2.1.1. Model 35
2.1.2. Ground State Energy 36
2.1.3. Electrostatic Energy 38
2.1.4. Shrinking Without Disorder 39
2.1.5. Disorder Effect 41
2.1.6. Conclusion 43
2.2. LDA Calculation And Compressibility 45
2.2.1. Model 45
2.2.2. Density Distribution 48
2.2.3. Compressibility 52

Chapter Page

2.2.4. Conclusion 55

3. Quantum and Semi-Classical Transportation 56

3.1. The Classical Model 56

3.1.1. Model 56

3.1.2. Results 59

3.1.3. Conclusion 59

3.2. Quantum Effects: One-Dimensional System 60

3.2.1. Model 61

3.2.2. Conductance 64

3.2.3. Connection With Experiments 66

3.2.4. Discussion 70

3.3. Semi-classical Percolation In 2D Systems 71

3.3.1. Model 71

3.3.2. Conductance 73

3.3.3. Scaling Properties 75

3.3.4. Remarks 77

4. In-Plane Magnetic Field Effects And Spin Polaron 79

4.1. Analysis 79

4.2. Electron Distribution And Resistivity 82

4.3. Discussions and Summary 86

BIBLIOGRAPHY 88

LIST OF FIGURES

Figure Page

1.1. A propagation path of the electron and its time reversal.................... 2

1.2. β-functions of the disordered systems 5

1.3. Temperature dependence of the resistivity in Si MOSFET 8

1.4. The resistivity of a p-GaAs/AlGaAs heterostructure.......................... 10

1.5. Resistivity as a function of electric field 12

1.6. Scaling behavior of the resistivity for a Si MOSFET.......................... 13

1.7. Scaling with the electric field 14

1.8. Resistivity response to parallel magnetic field.................................. 16

1.9. Resistivity response to parallel magnetic field for a p-GaAs/AlGaAs heterostructure.. 17

1.10. Temperature dependence of resistivity for different parallel magnetic fields. 18

1.11. The density dependence of the compressibility................................. 20

1.12. Weak localization effect in p-GaAs/AlGaAs sample........................... 22

1.13. Temperature thresholds in the ρ vs T plane for a Si MOSFET 24

1.14. In-plane magnetic field dependence of the resistivity.......................... 32

2.1. A simple model to investigate the shrinking of the electron distribution.. 35

2.2. The ground state energy of electron system 37

2.3. The shrinking distance of an electron disc without disorder................ 40

2.4. The shrinking of an electron disc with disorder................................... 42

Figure Page

2.5. Phase diagram for the electron disc shrinking 44

2.6. Density distribution in a 2D system 50

2.7. The density distribution for a non-interacting 2D system 51

2.8. Compressibility of a disordered 2D system 53

3.1. Mapping from an inhomogeneous 2D system to a resistance network 57

3.2. Temperature dependence of the resistance of the model resistance network 58

3.3. 1D model with dephasing and disorder 61

3.4. Dephasing scatter 62

3.5. The conductance vs. dephasing rate 65

3.6. The localization length and dephasing length at turning point 67

3.7. Temperature dependence of Resistivity 68

3.8. The crossing point on conductance-disorder plane 69

3.9. Lattice model for 2 2D system with dephasing 72

3.10. Conductance of a 2D percolation system with dephasing 74

3.11. Scaling properties of the conductance 76

3.12. P_v versus P_c. 77

4.1. The ground state energy per particle depending on the spin polarization 81

4.2. The temperature dependence of the resistivity for different in-plane magnetic field strengths 85

4.3. The resistivities depending on the in-plane magnetic field for different temperatures 86

CHAPTER 1

Introduction

The metal-insulator transition is one of the most interesting topics in the condensed matter physics. The modern theory of the metal-insulator transition is based on the scaling theory of localization, which was proposed by Abrahams *et al.* [1], and concludes that all one-dimensional and two-dimensional systems are insulators, and the metal-insulator transition only exists in the three-dimensional systems.

However, the recent discovery of the metal-insulator transitions (MIT) in dilute two-dimensional (2D) electron (hole) systems has raised the question concerning the existence of the metallic phase in 2D systems. While contradicting to the prediction of the scaling theory, the experiments deserve a theoretical explanation. Since the electron-electron interaction is important for the experimental systems, and the scaling theory of localization is initially developed in non-interacting systems, the validity of the scaling theory in strongly interacting systems deserves further study.

1.1 Weak Localization and Scaling Theory of Localization

1.1.1 Weak Localization

In the classical theory, the finite conductance arises due to the electron-impurity scattering, where the electrons and impurities are considered as particle-like classical objects. While this is true in general, the quantum interference effect can not be ignored for a system at low temperatures due to the wave-nature of electrons. It turns out to have profound effects on the behavior of a conductance.

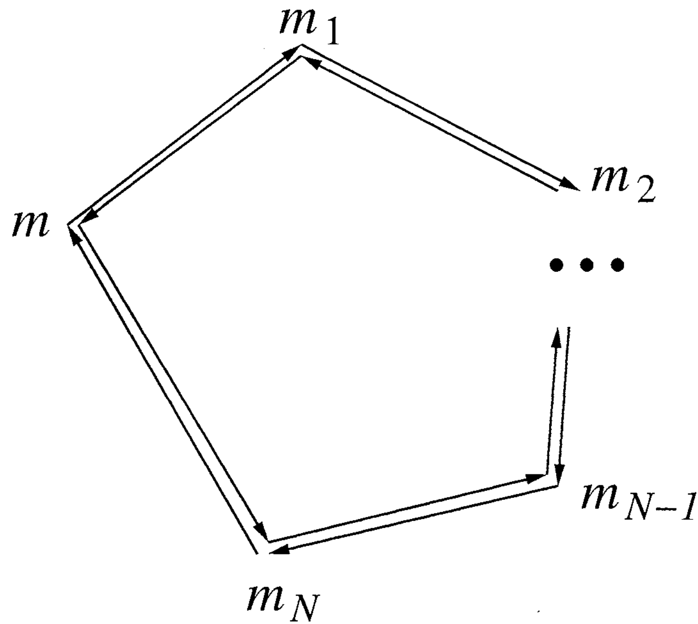

Figure 1.1. A propagation path of the electron and its time reversal.

The most important effect of the quantum interference in terms of transport property is weak localization. Due to the interference between the different propagation paths of the electrons, the quantum system has higher backscattering probability comparing to its classical counterpart. It leads to an interesting behavior for the quantum system which has no classical counterpart: all one-dimensional and two-dimensional systems are localized.

To demonstrate the basic idea, let us consider a simple process. We would like to calculate the probability $R(m \to m)$ that the electron in position (or state) m is scattered back to the position (or state) m. From the basic quantum mechanics, the probability could be calculated by squaring the sum of the amplitude of all possible Feymann paths,

$$R(m \to m) = |\sum_i A_i(m \to m)|^2,$$

where A_i denotes the amplitude for the different path of the propagation.

To simplify the discussion, we just consider a specific path P, as shown in Fig. 1.1,

$$m \to m_1 \to m_2 \to \cdots \to m_{N-1} \to m_N \to m$$

and its time-reversed path $\bar{P}$.

$$m \to m_N \to m_{N-1} \to \cdots \to m_2 \to m_1 \to m$$

Supposing that the scatter is elastic and there is no magnetic field, It can be proved that the time-reversed path has same amplitude and phase as the original path, so the total probability is,

$$R(m \to m) = |A_P + A_{\bar{P}}|^2 = |A_P|^2 + |A_{\bar{P}}|^2 + A_P A_{\bar{P}}^* + A_P^* A_{\bar{P}} = 4|A_P|^2,$$

while the corresponding classical system has

$$R_c(m \to m) = |A_P|^2 + |A_{\bar{P}}|^2 = 2|A_P|^2.$$

The backscattering probability of a quantum system is twice larger than the corresponding classical system.

The higher backscattering probability has profound effect on the conductance behavior of a quantum system. It is the origin of the localization behavior of the quantum system.

1.1.2 Scaling Theory of Localization

The scaling theory of localization provides an unify prediction of the behavior of the conductance for a quantum system. The theory is based on an observation by Thouless [2],

$$g(L) = \frac{\Delta E}{dE/dN},$$

where $g(L)$ is the dimensionless conductance of a d-dimensional supercube with size L in the quantum unit of conductance $2e^2/h$,

$$g(L) = \frac{G(L)}{2e^2/h},$$

dE/dN is the mean spacing of the energy levels, and ΔE is the geometric mean of the fluctuation in energy level caused by replacing periodic to antiperiodic boundary conditions. The dimensionless conductance $g(L)$ is the dimensionless ratio measuring the change of energy levels in changing the boundary conditions.

Contemplating that combining γ^d cubes into a system with size γL, the conductance of the larger system will be determined by the new energy levels of the larger system, which in turn is determined by the energy levels of the building blocks and their responses to the change of boundary conditions. If supposing that the dimensionless conductance $g(L)$ for the smaller systems is the only relevant quality for the scaling process, we have the single-parameter scaling relation of the conductance,

$$g(\gamma L) = f(\gamma, g(L))$$

The scaling function f is independent on the detail disorder profile in the system. The assumption was verified numerically by MacKinnon and Weger [3].

The scaling relation can be rewritten as the continuous form,

$$\frac{d \ln g(L)}{d \ln L} = \beta(g) \tag{1.1}$$

$\beta(g)$ only depends on the conductance g.

The asymptotic behavior of the β function could be determined by simple argument. For the limit $g \to 0$, the system is expected to be strongly localized, and the conductance exponentially decays with the size of the system,

$$g(L) = g_0 e^{-\alpha L}.$$

Thus,

$$\lim_{g \to 0} \beta(g) = \ln \left(\frac{g}{g_0} \right).$$

The limit $g \to \infty$ corresponds to the macroscopic case, and follows Ohm's law,

$$g(L) = \sigma L^{d-2},$$

and

$$\lim_{g \to \infty} \beta(g) = d - 2.$$

The determination of β-function between the two limits is beyond the capability of the theory. One has to make assumption in this region. A reasonable plot of β function is depicted in Fig. 1.2. Apparently we are making assumption that the β function is an increasing function of the conductance.

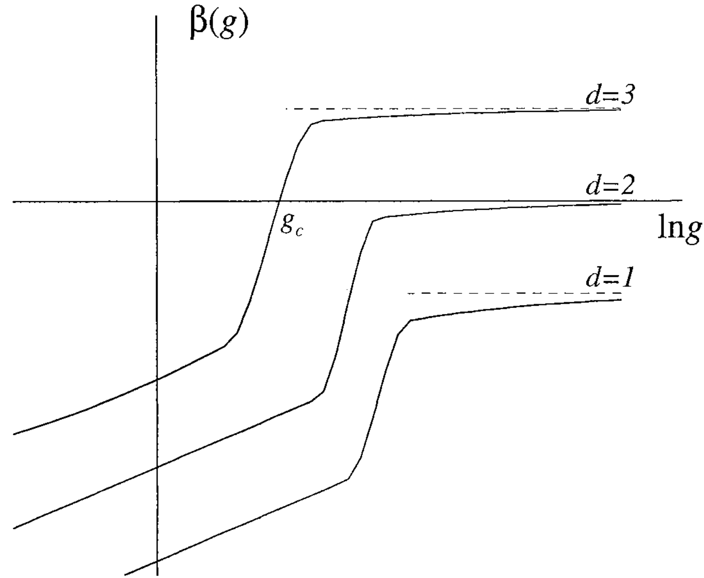

Figure 1.2. β-functions of the disordered systems. g_c denotes the critical point of the metal-insulator transition of the three-dimensional system.

For large g, when taking account of the weak localization effect discussed in Sec. 1.1.1, the β-function has a perturbation expansion about $1/g$,

$$\beta(g) \approx d - 2 - \frac{a}{g} + \cdots, \tag{1.2}$$

where a is a positive constant.

Integrating the scaling equation 1.1, one gets the quantum correction to the conductance,

$$g(L) = \begin{cases} \sigma_0/L - a, & d = 1 \\ \sigma_0 - a\ln L, & d = 2 \\ \sigma_0 L + a, & d = 3 \end{cases} .$$

And the conductivity is,

$$\sigma(L) = g(L)L^{2-d} = \begin{cases} \sigma_0 - aL, & d = 1 \\ \sigma_0 - a\ln L, & d = 2 \\ \sigma_0 + aL, & d = 3 \end{cases} .$$

For the one-dimensional and two-dimensional systems, the conductivity is a decreasing function of the system size. For a macroscopic system, the size is so large that the conductivity will finally decrease to zero. It follows the main conclusion of

the scaling theory of localization: *all one-dimensional and two-dimensional systems are insulators.*

Few notes concerning the theory:

(i) The scaling theory of localization is based on the scaling assumption. Besides that, other assumptions such as Eq. 1.2 are also implied. While these assumptions are confirmed for non-interacting systems, their validity for interacting system is generally unknown.

(ii) The system is supposed to be in zero temperature in the discussion. However, the temperature dependence of the conductance can be readily inferred from the size dependence of the conductance. In a real system, it is generally agreed that the size of system could be replaced by the phase coherence length L_φ, beyond which the electron loses its phase memory and has no quantum interference. The dephasing length is a function of the temperature, normally goes as $L_\varphi \sim 1/T^\nu$. For instance, by substituting the size of system to the phase coherence length, the temperature dependence of the conductivity of a two dimensional system is:

$$\sigma(T) = \sigma_0 - \sigma_1 \ln T \tag{1.3}$$

1.2 Two-Dimensional Metal-Insulator Transition

According to the scaling theory of localization presented in Sec. 1.1.2, the conductance of a two-dimensional system should logarithmically decrease (weak localization, Eq. 1.3) with the decreasing temperature, and is reduced to zero at absolute zero temperature. No metal-insulator transition is expected. This behavior is indeed confirmed in the high density MOSFET systems [4,5], which could be well considered as the non-interacting systems.

However, when the electron density becomes lower, the situation is less clear since the electron-electron interaction becomes important. On the other hand, in the limit of extremely low density, the electron system is expected to form a new phase: Wigner crystal [6]. The Wigner crystal lattice is pinned by disorder, the system is strongly localized and the conducting is through the hopping between the lattice

sites. So the conductivity is expected to decrease exponentially with the decreasing temperature in this limit.

In the low density (strongly interacting) and high density (weakly interacting) limits, the two-dimensional systems are expected to be insulator. One may jump to conclusion that the two-dimensional electron systems will always be insulating systems in all density regimes and interaction strengths.

However, the recent studies on the temperature dependences of the resistance of dilute 2D systems in the zero magnetic field show that the conclusion may be incorrect. The metallic behavior, *i.e.*, the resistance of the system decreases with a decreasing temperature, is observed in a variety of dilute, high mobility 2D systems. These experiments incite the new interests on whether the metallic phase exists in 2D systems, especially in those strongly correlated systems.

In this section, the basic experimental facts will be reviewed. The existing theories are also discussed. A full review of the topic can be found in Abrahams *et al.* [7].

1.2.1 Temperature Dependence of Resistivity

The first experiment that claims a metallic phase in 2D system is by Kravchenko *et al.* [8,9]. They measured the temperature dependence of the resistivity on the high mobility (low disorder) silicon MOSFETs. The mobility of the samples is so high that the measurement can be carried out in the density below 10^{11}cm^{-2}.

Fig. 1.3 shows a typical behavior of the temperature dependence of the resistivity in Si MOSFET systems. At high density, the resistivity drops rapidly with decreasing temperature, indicating a metal-like behavior. The drop of the resistivity could be several orders of magnitude. The temperature dependence of resistivity can be fitted reasonably well by the formula [10],

$$\rho(T) = \rho_1 + \rho_2 \exp\left(-\frac{\Delta}{T}\right). \tag{1.4}$$

ρ_1 and ρ_2 are the functions of the density, but are independent on the temperature. The fitting breaks down at a certain temperature T^*, above which the resistivity

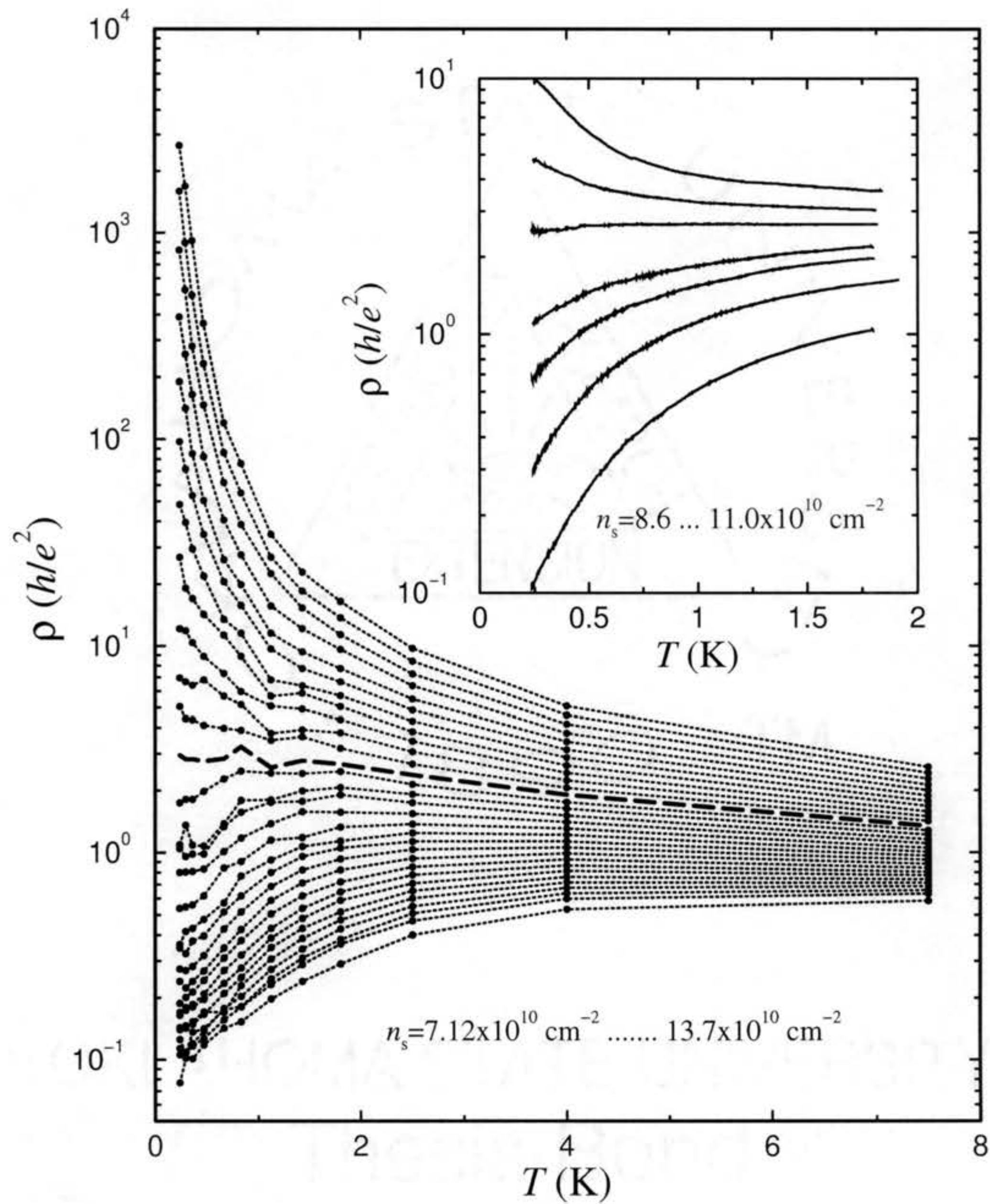

Figure 1.3. Temperature dependence of the resistivity in a silicon MOSFET for 30 different electron densities [9]. The inset shows behavior of the resistivity close to the critical density [10]. From Abrahams *et. al.* [7].

decreases with the increasing temperature again (insulating behavior). The exponential dependence on the temperature usually associates with the energy gap in the excitation spectrum.

At lower densities, the system becomes insulating. The resistivity could be fitted by the formula [11],

$$\rho(T) = \rho_0 \exp\left(\sqrt{\frac{T_1}{T}}\right). \tag{1.5}$$

The behavior is known to associate with the variable-range hopping between localized states under the influence of the Coulomb interaction (Efros-Shklovskii hopping) [12]. ρ_0 is a temperature independent constant and is close to the quantum unit of the resistance, h/e^2 [11,13]. This is in contrast to the normal Efros-Shklovskii hopping, where ρ_0 weakly depends on the temperature.

There exists a critical density which separates the insulating and metallic regimes. At this density, the resistivity is found to be independent of temperature to the lowest accessible temperature [14,15], and the resistivity is of the order of the quantum resistance unit, h/e^2.

The qualitatively similar behavior is observed in a variety of electron and hole systems, including Si MOSFETs with different geometry and oxide thicknesses [16], p-SiGe heterostructures [17,18], p-GaAs/AlGaAs heterostructures [19–22], n-AlAs heterostructures [23] and n-GaAs/AlGaAs heterostructures [24]. It indicates that the observed metal-insulator transition is a universal behavior instead of a special property associated with a specific material.

Fig. 1.4 shows the behavior of a hole system, p-GaAs/GaAlAs heterostructure. It shares many qualitative features as the Si MOSFET systems, although the resistivity drop at the metallic side is much weaker than the drop in Si MOSFETs. The resistivity at the critical density is also order of the h/e^2. Eq. 1.4-1.5 are still valid for this system.

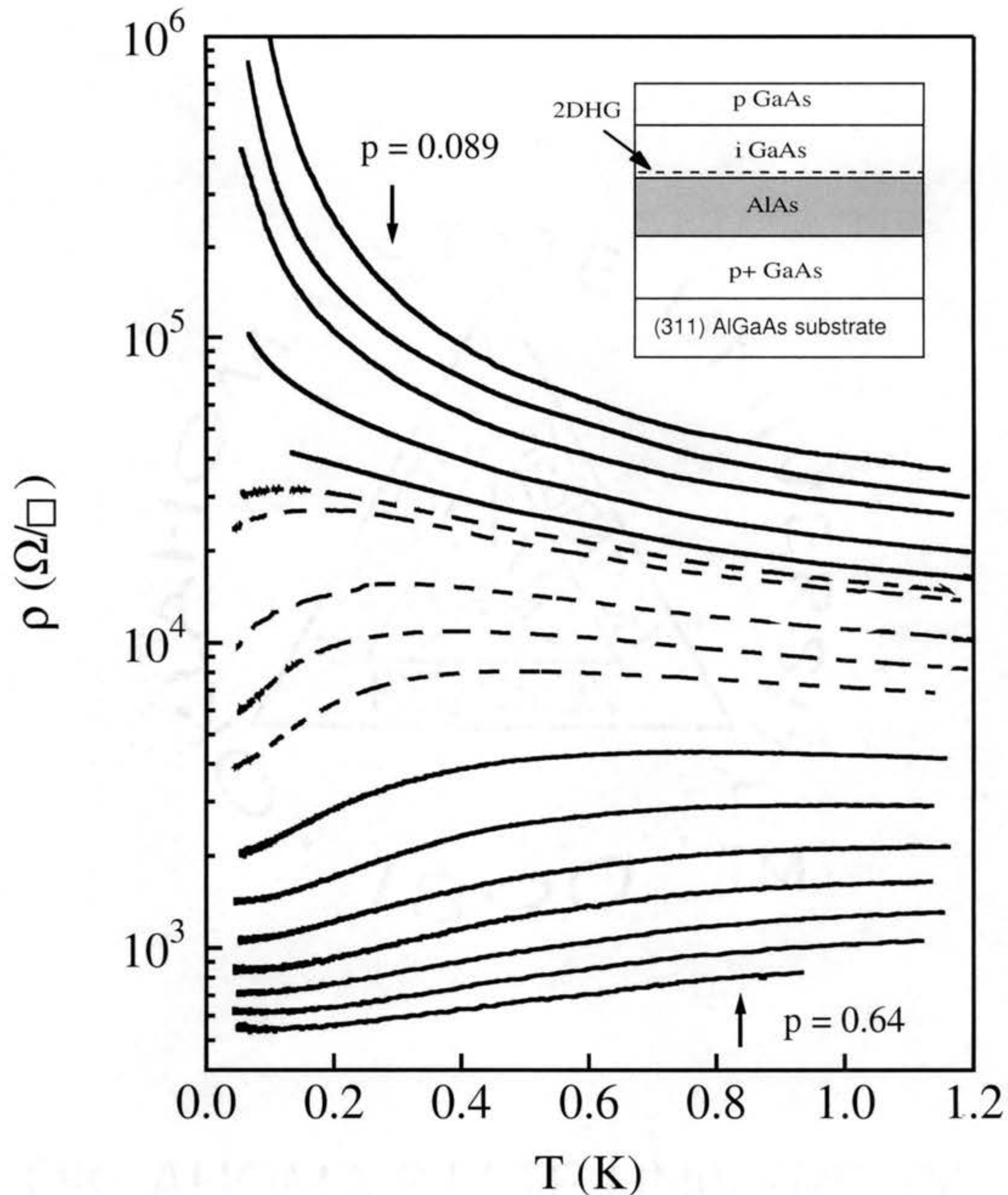

Figure 1.4. Resistivity as a function of temperature at $B = 0$ at various fixed densities for a p-GaAs/AlGaAs heterostructure. p =0.089, 0.94, 0.99, 0.109, 0.119, 0.125, 0.13, 0.15, 0.17, 0.19 0.25, 0.32, 0.38, 0.45, 0.51, 0.57 and $0.64 \cdot 10^{11}$ cm^{-2}. Inset: Schematic presentation of the p-type ISIS structure grown on semi-insulating (311)A GaAs substrate, consisting of a thick p^+ buffer, a 300 nm undoped AlAs barrier, a 150 nm undoped GaAs channel layer, and a top 50 nm GaAs layer which is p doped. The 2DHS forms at the lower interface of the channel layer upon application of negative bias to the p^+ conducting layer. From Hanein *et al.* [19].

1.2.2 Nonlinear Effects

The resistivity mentioned above is obtained in the linear regime, *i. e.*, the electric field strength is close to zero, $E \to 0$. If the electric field strength is increased in the measurement, the interesting nonlinear resistivity-electric field dependence analogous to the resistivity-temperature behavior is observed.

Fig. 1.5 shows the electric field dependence of the resistivity in a Si MOSFET system [25]. The resistivity is defined as $\rho = (V/I)(W/L)$, where V is the voltage across the sample and I is the electric current measured. As seen in the Fig. 1.3, the electric field dependence of the resistivity also shows different behaviors for different carrier densities. At the high density, the resistivity is an increasing function of the electric field, indicating a metal-like behavior. At low density, the resistivity decreases with the the increasing electric field, as expected in an insulating system. There also exists a critical density on which the resistivity is nearly independent on the electric field.

The phenomena have connection with behavior of the temperature dependence of the resistivity. We will discuss it in the next subsection.

1.2.3 Scaling

A striking feature of the 2D MIT is that the resistivity can be scaled with density and temperature in a wide range of density and a certain range of temperature (below T^*). The resistivity can be written as,

$$\rho(n_s, T) = f(T/T_0(n_s)), \tag{1.6}$$

where n_s is the carrier density, $T_0(n_s)$ is the scaling function which is a function of the density.

It can be clearly seen from Fig. 1.6 that the temperature dependence of the resistivity can be well scaled into two branches. Near the critical density, the scaling function $T_0(n_s)$ has the density dependence,

$$T_0(n_s) \propto |n_s - n_c|^\beta, \tag{1.7}$$

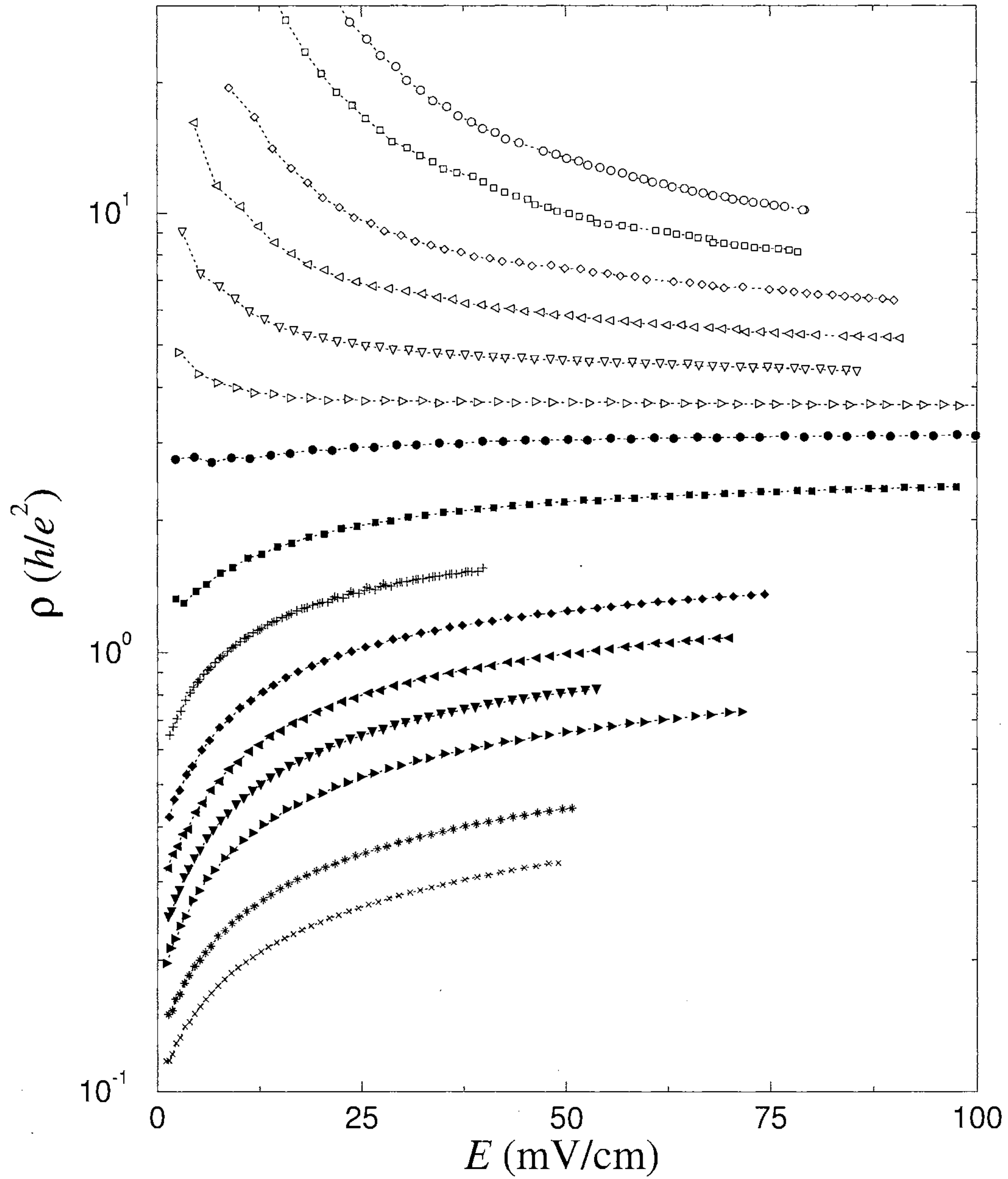

Figure 1.5. Resistivity as a function of electric field at $n_s = 7.81$, 7.92, 8.03, 8.14, 8.25, 8.36, 8.47, 8.70, 8.91, 9.13, 9.35, 9.57, 9.79, 10.34, and 10.78×10^{10} cm^{-2} at $T = 0.22$ K. From Kravchenko *et al.* [25].

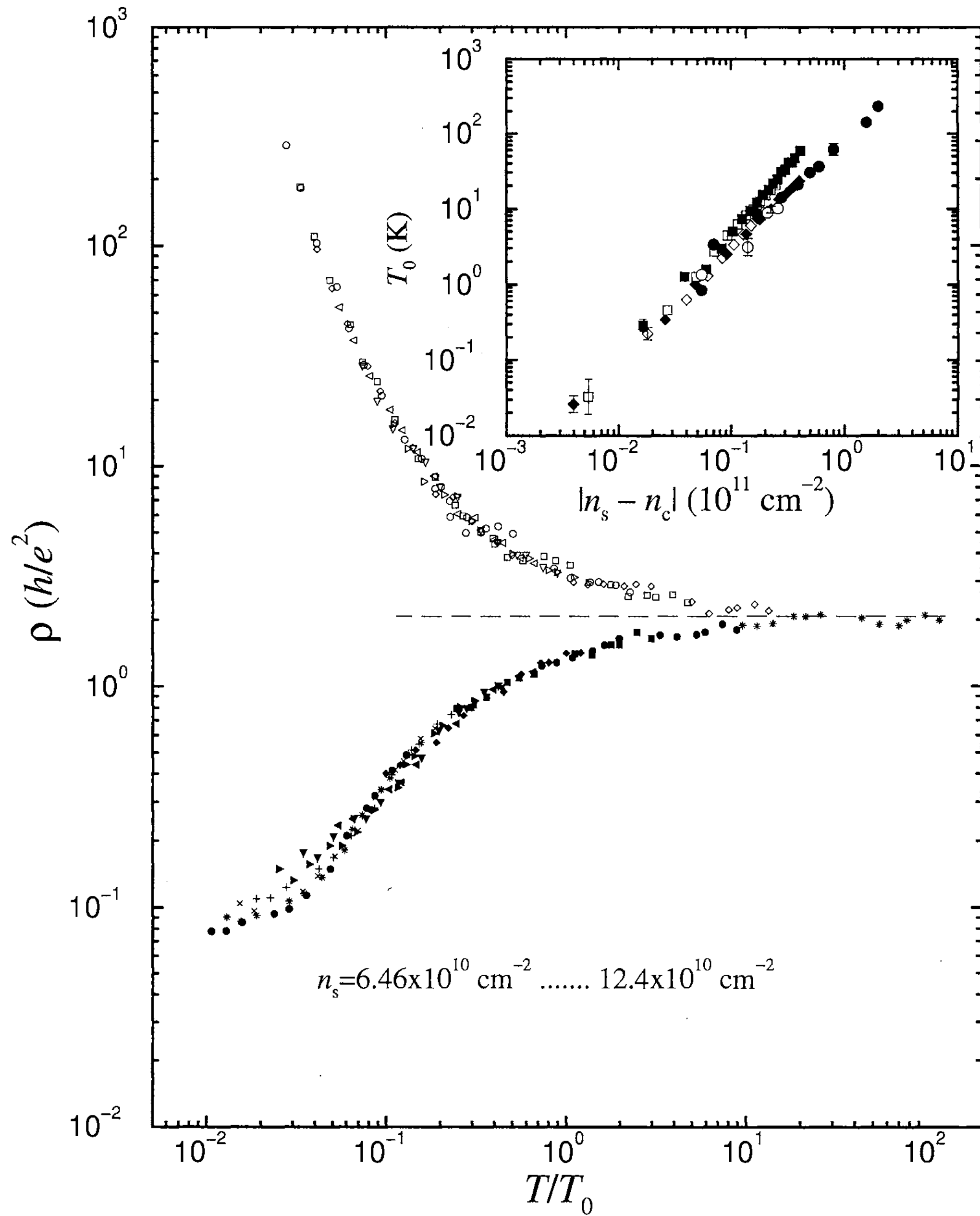

Figure 1.6. Scaling behavior of the resistivity for a Si MOSFET. Inset shows density dependence of the scaling parameter, T_0. From Kravchenko *et al.* [9].

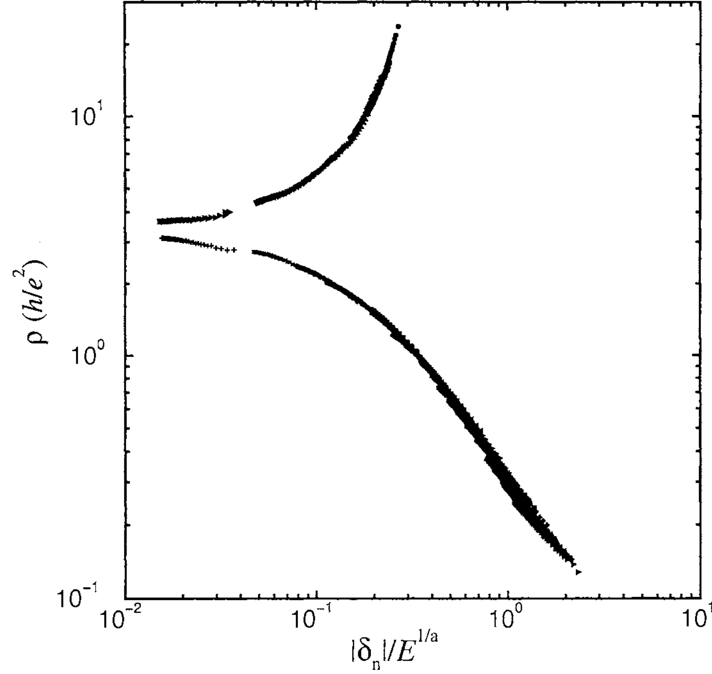

Figure 1.7. The scaling with the electric field. $\delta_n = (n - n_c)/n_c$, $a = 2.7$. From Kravchenko *et al.*. [25].

which is independent on the sign of $n_s - n_c$, where n_c is the critical density. The scaling exponent β was found to be 1.6 ± 0.1 for Si MOSFETs [9,16].

However, the scaling in other systems are not as successful as in Si MOSFETs. For those systems with weak metallic behavior, such as p-GaAs/AlGaAs heterostructures and low mobility Si MOSFETs, the scaling may fail entirely [19,21]. For those systems do scale successfully, the scaling exponents may not be of the same value as for Si MOSFETs [17].

Another scaling behavior observed in the Si MOSFET is the duality, *i. e.*,

$$\rho^*(n_c - \delta, T) = 1/\rho^*(n_c + \delta, T),$$

where $\rho^* = \rho/\rho_c$, ρ_c is the resistivity at the critical density. To get the duality, the density have to be limited in a certain range. The duality is proved to be a generic feature of the critical region [26] for a continuous quantum phase transition [27].

Corresponding to the scaling behavior of the density dependence of resistivity, there is similar scaling behavior for the electric field dependence. Fig. 1.7 shows the scaling behavior of the resistivity for Si MOSFET with the electric field [25]. The

resistivity has the scaling form,

$$\rho(n_s, E) = \tilde{\rho}(\delta_n / E^{1/a}).$$

Following the generic argument for a continuous quantum transition [27], scaling with the electric field is related to scaling with the temperature. The scaling exponents are related by,

$$\begin{aligned} \beta &= z\nu_1 \\ a &= (z+1)\nu_1 \,, \end{aligned}$$

where ν_1 is the critical exponent for the correlation length, and z is the dynamical exponent. Derived from the experimental data, the correlation exponent $\nu_1 = 1.5 - 1.9$ [25,28], and $z = 0.8 - 1.2$ [25,28,29].

1.2.4 Parallel Magnetic Field Effects

Another unusual property of dilute 2D systems is its response to a parallel magnetic field. It was found that a relatively weak parallel field could greatly suppress or even totally destroy the metallic behavior, causing the resistivity to increase by orders of magnitude [30–32].

Fig. 1.8 shows a typical behavior of the response of the resistivity to a parallel magnetic field for the Si MOSFETs. The resistivity increases rapidly with the parallel magnetic field. An order of magnitude increasing is observed in this sample. Even higher change of the resistivity is observer at lower temperatures. The resistivity saturates at a certain magnetic field. The response to the parallel magnetic field is qualitatively similar on both metal and insulator sides.

The behavior in p-GaAs/AlGaAs hole systems is qualitatively same as in the Si MOSFETs [20,33]. The difference is that the resistivity does not saturates at high magnetic field, instead increases with the magnetic field at a slower rate. Fig. 1.9 shows the behavior.

A strong parallel magnetic field destroys the metallic behavior. Fig. 1.10 shows the temperature dependence of resistivity for a given density which is metallic in zero

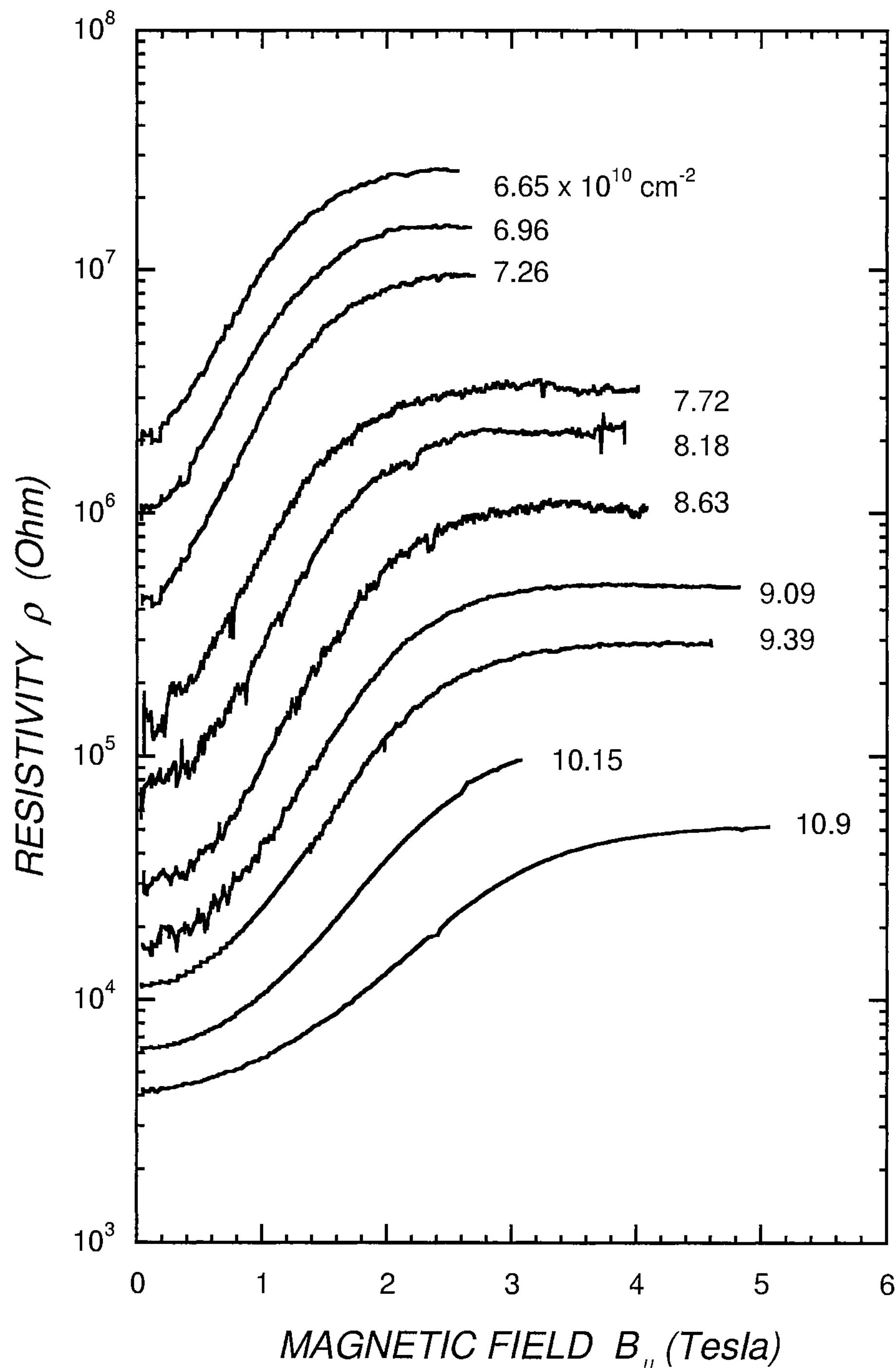

Figure 1.8. Resistivity as the function of the parallel magnetic field for a Si MOSFET. The densities across the metal and insulator sides. From Metres *et al.* [32].

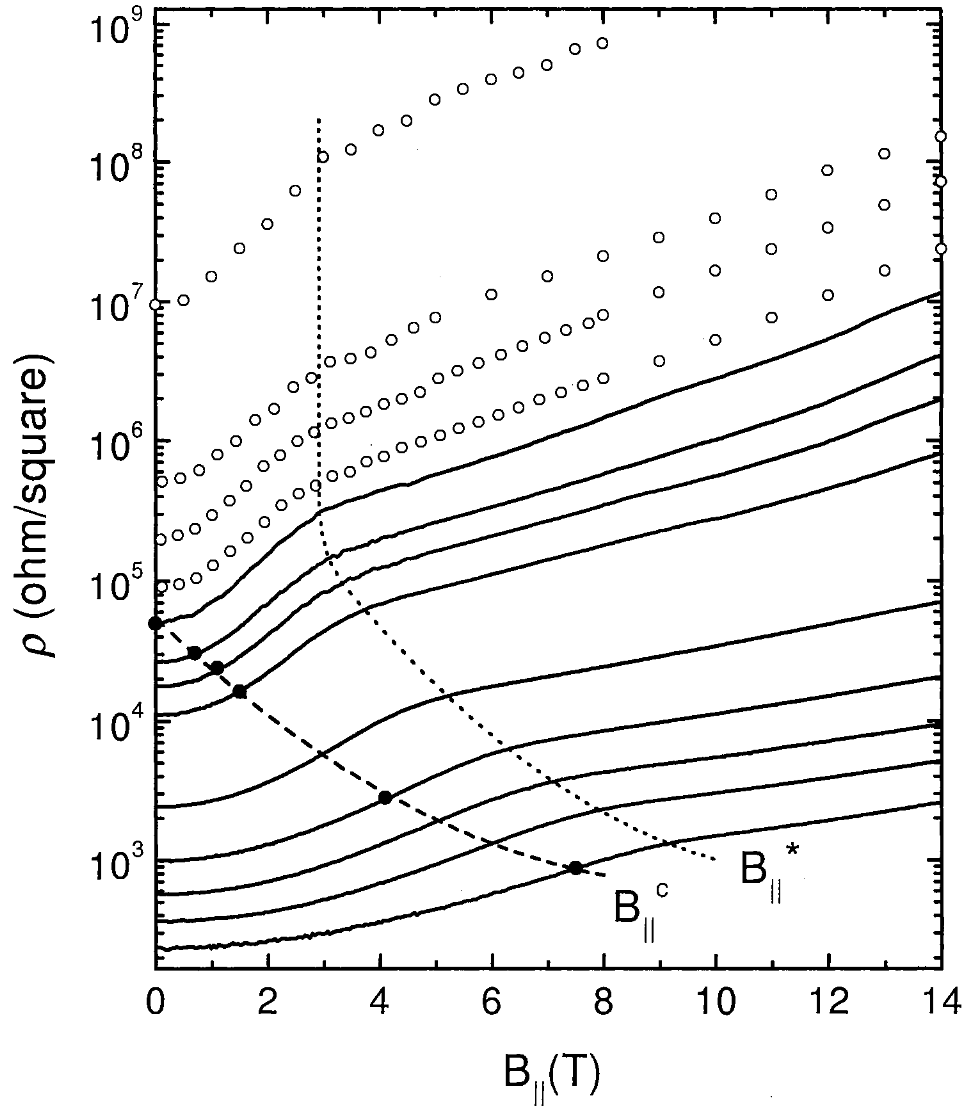

Figure 1.9. Resistivity as the function of the parallel magnetic field for a p-GaAs/AlGaAs heterostructure. The solid lines are for densities above the critical density, and open circles are for densities below the critical density. From Yoon *et al.* [33].

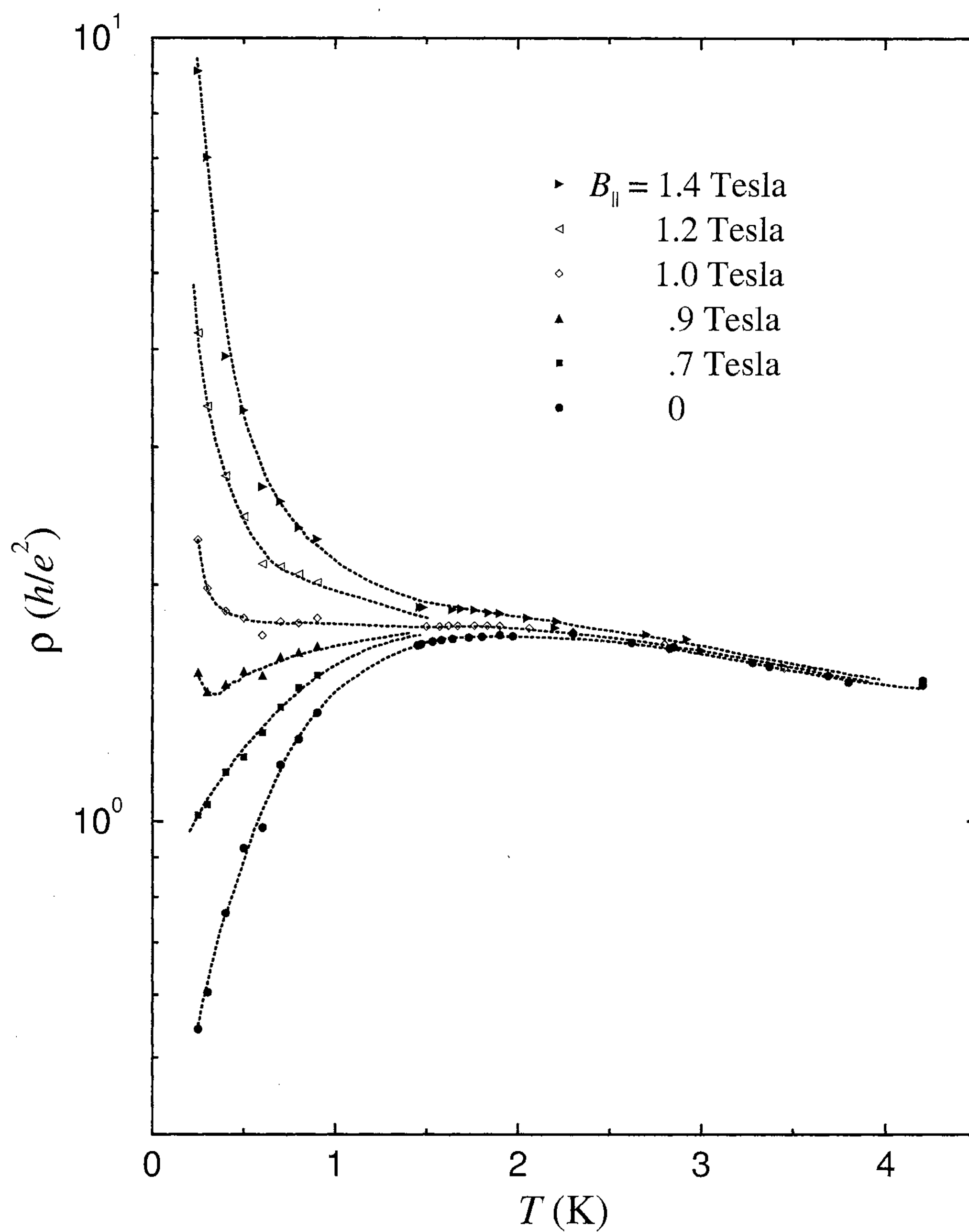

Figure 1.10. Temperature dependence of resistivity of five different magnetic fields for a Si MOSFET. From Simonian *et al.* [30].

field turns to insulating behavior at a strong field. Yoon *et al.* [33] show that there exists a critical field above which the metallic behavior is destroyed.

Since the parallel magnetic field only couples with the spins of electrons (provided magnetic field is not so strong that the finite thickness effect becomes important), the observed behavior must be related to the electronic spin polarization. It is found that the magnetic field which is required to saturate the resistivity is about the same value as the field needed to fully polarize the electron spins [34,35].

1.2.5 Measurements Other Than Resistivity

The experiments discussed so far are all based on measurements of resistivity. Although resistivity is easily accessible to experimentalists, other measurements may also shed some light on the nature of the metal-insulator transition.

Dultz and Jiang [36] measured the compressibility κ in GaAs/AlGaAs systems. The compressibility can be written as,

$$\frac{1}{\kappa} = n^2 \frac{\delta \mu}{\delta n},$$

where μ is the chemical potential of the system, and n is the electron density. Within the Hartree-Fock approximation,

$$\frac{\delta \mu}{\delta n} = \frac{\pi \hbar^2}{m} - \left(\frac{2}{\pi}\right)^{\frac{1}{2}} \frac{e^2}{4\pi\epsilon} n^{-1/2}.$$

$1/\kappa$ becomes negative at low densities and decreases with a decreasing density. However, it is found in the experiment that the negative $1/\kappa$ at low densities reaches a minimum at the critical density n_c of the 2D MIT, and then increases dramatically with further decreasing density, as shown in Fig. 2.8. Although this surprising upturn of $1/\kappa$ was observed much earlier in a pioneering work by Eisenstein *et. al.* [37,38], this is first time that the minimum point in $1/\kappa$ is identified as the critical density for the 2D MIT.

Ilani *et al.* [39,40] measured the local compressibility of the GaAs/AlGaAs heterostructures. They found that local compressibility deviates the Hartree-Fock prediction by an order of magnitude when the system enters into the insulator regime.

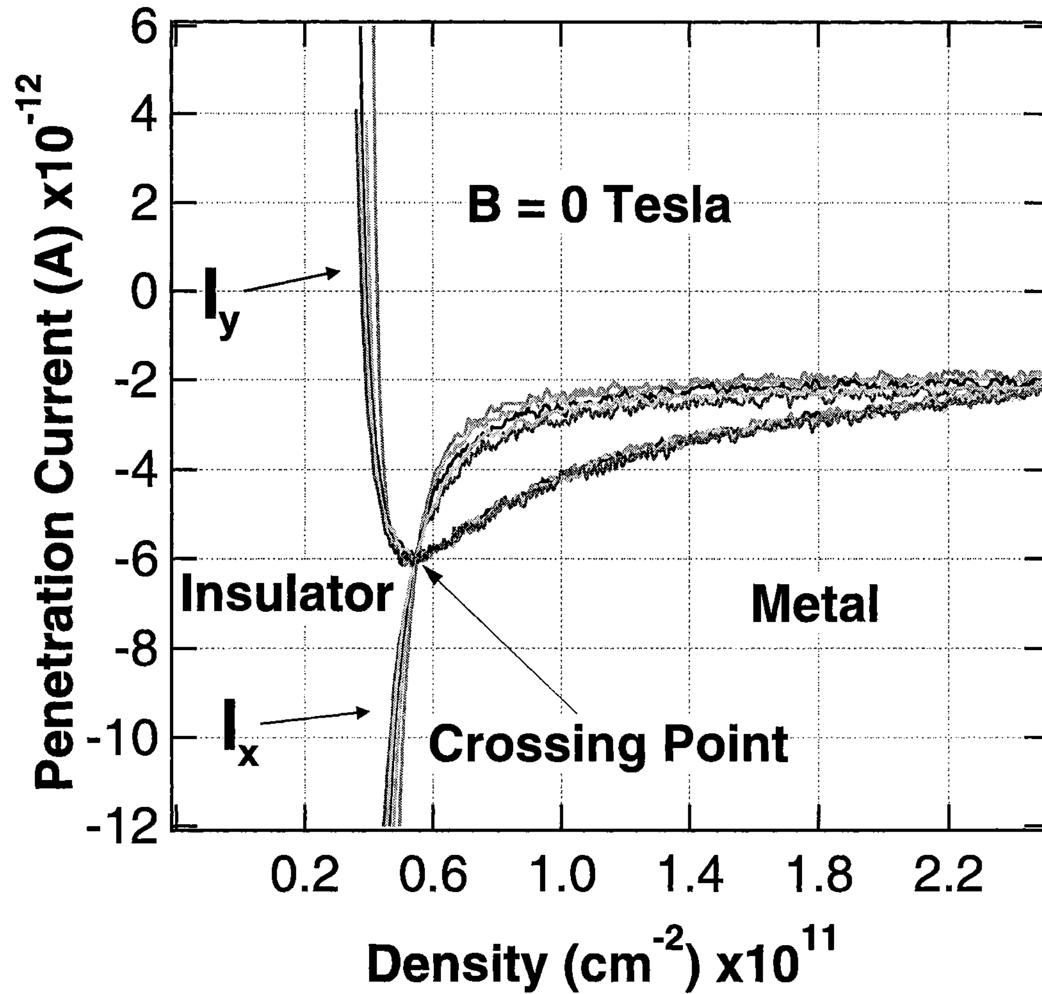

Figure 1.11. I_x and I_y vs density for five temperatures at an excitation frequency of 100 Hz: blue- 0.33 K, green- 0.56 K, black- 0.82 K, orange- 1.02 K, red- 1.28 K. $I_y \propto \delta\mu/\delta n$. The crossing point of the five dissipation channel curves (I_x) corresponds to the metal-insulator phase transition at $B = 0$. The minimum in the inverse compressibility channel occurs at the same density of $p = 5.5 \times 10^{10}$ cm^{-2}. From Dultz and Jiang [36].

They also show that the spatial distribution of electron density is not homogeneous. They concluded that the system near the metal-insulator transition consists of the localized charge which coexists with the surrounding metallic phase. When the density is lower into the insulating state, the proportion of the localized charge increases while the metallic phase disappears. It strongly suggests that the metal-insulator transition is connected with the microscopic restructuring inside the system, and is the percolation transition of two phases.

1.2.6 Quantum Phase Transition or Not?

Although the evidences that support the 2D MIT seem to be overwhelming, there are emerging experiments arguing that the 2D MIT may not be quantum transition in nature, instead some other classical or semi-classical mechanisms cause the apparent metallic behavior.

From the scaling theory of localization, the quantum effect causes a weak temperature dependence of the conductivity,

$$\sigma(T) = \sigma_0 - \sigma_1 \ln T \, ,$$

which drives the system into an insulating state at zero temperature. However, if there exists a classical or semi-classical mechanism which causes strong increase of the conductivity with decreasing temperature at a finite temperature, the weak localization effect may be smeared. On the other hand, by the original definition of the quantum metal-insulator transition, the system is considered as a metal only when its zero temperature resistivity is finite. In practice, the metallic and insulator states are judged by the sign of $d\rho/dT$. It is not necessarilly an equivalent condition to the original criterion. Although a strong resistivity drop is observed on the metallic side, the fate of the resistivity at zero temperature is unknown. It could be argued that the resistivity curve of the metallic phase may turn up again at low temperatures, and reenters into an insulator regime.

Simmons *et al.* [41] investigated the weak localization effect in the p-GaAs/AlGaAs systems. The upturn of the resistivity on the metallic side is indeed observed in the

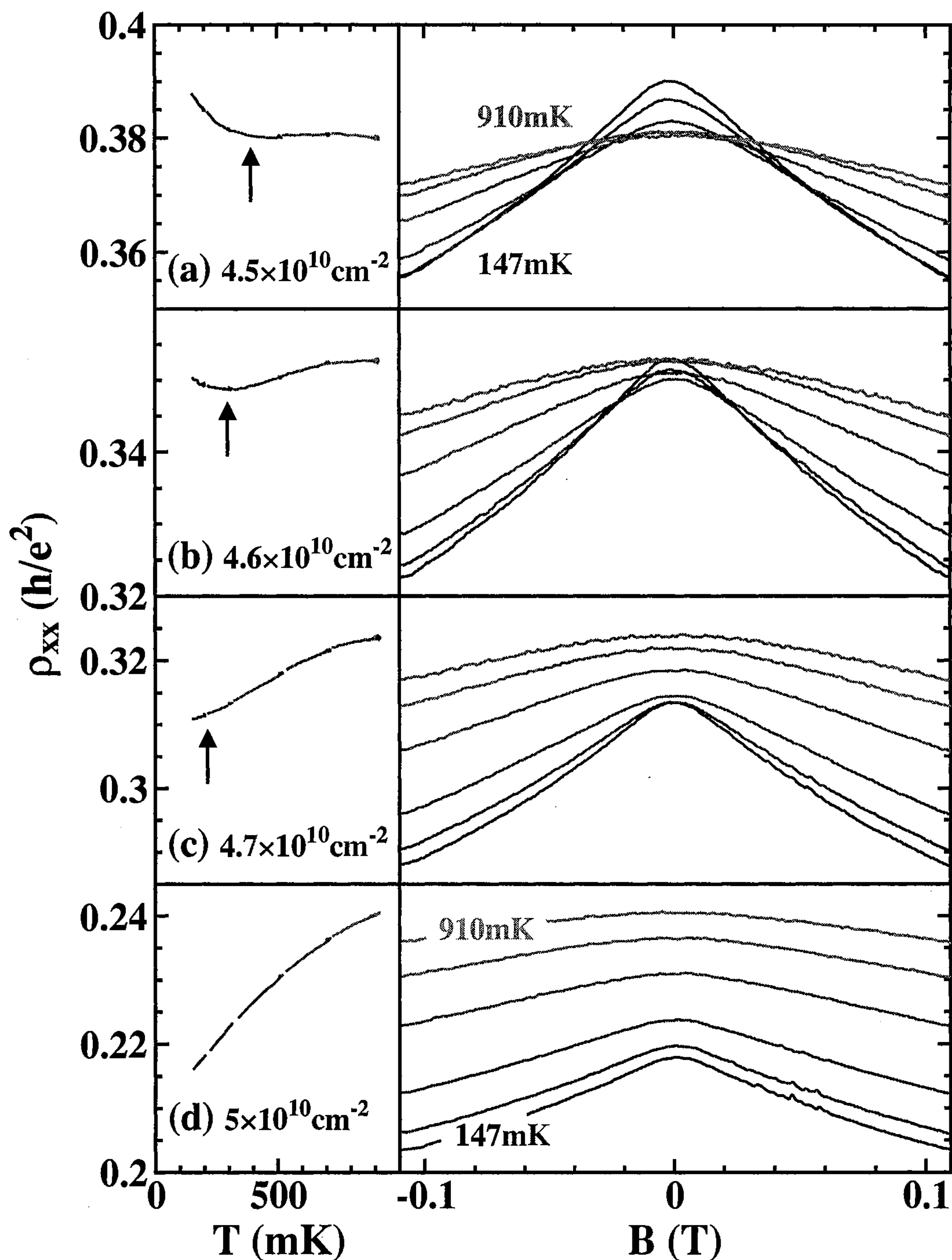

Figure 1.12. (a)-(d) The left hand panels show resistivity at B=0 versus temperature data, illustrating the transition from insulating to metallic behavior as the density increases. (a) is just on the insulating side, and (b)-(d) are in metallic side. The right hand panels show the corresponding magnetoresistance traces for temperatures of 147, 200, 303, 510, 705 and 910mK. From Simmons *et al.* [41].

low temperature limit, as shown in Fig. 1.12b. By investigating negative magnetoresistance of the 2D system [42], they show that the upturn is caused by the weak localization effect, while there is no evidence of weak localization in the region where the resistivity strongly drops. It indicates that the system will become insulator again at low temperatures even at high density, and the strong resistivity drop observed is not related to the single particle quantum interference effect.

Brunthaler *et al.* [43] investigated the quantum effect in Si MOSFETs. They found that the strong resistivity drop, which is considered as the signature of the metallic behavior, occurs at the temperature well above the regime where the quantum effect is important. Fig. 1.13 shows two temperature boundaries for the quantum effects. It indicates that the strong resistivity drop is caused neither by single electron quantum interference effect ($\tau_\varphi = \tau$ boundary) nor by the electron-electron induced quantum interference effect ($kT_{ee} = \hbar/\tau$ boundary).

Both experiments suggest that the apparent metallic behavior is caused by semi-classical mechanisms. When the quantum effect takes hold of the system, the system may reenter into the insulating state. In other words, there will be no metal-insulator transition at zero temperature.

1.3 Theory

The most important feature of the 2D MIT systems is that it is a *strongly correlated system.* The typical density at which the metal-insulator transition is observed in Si MOSFET is about $n_s = 10^{11}$ cm^{-2}, and the the electron-electron interaction energy is estimated to be,

$$E_{\text{e-e}} \sim \frac{e^2}{\epsilon}\sqrt{(\pi n_s)} \approx 10\text{meV},$$

and the Fermi energy is,

$$E_F = \frac{\pi \hbar^2 n_s}{2m^*} \approx 0.58\text{meV},$$

where ϵ is the dielectric constant, m^* is the effective mass of electron in Si MOSFET. The ratio between the electron-electron interaction energy to the Fermi energy is,

$$r_s \equiv \frac{E_{\text{e-e}}}{E_F} = \frac{1}{a_B^* \sqrt{\pi n_s}} > 10, \tag{1.8}$$

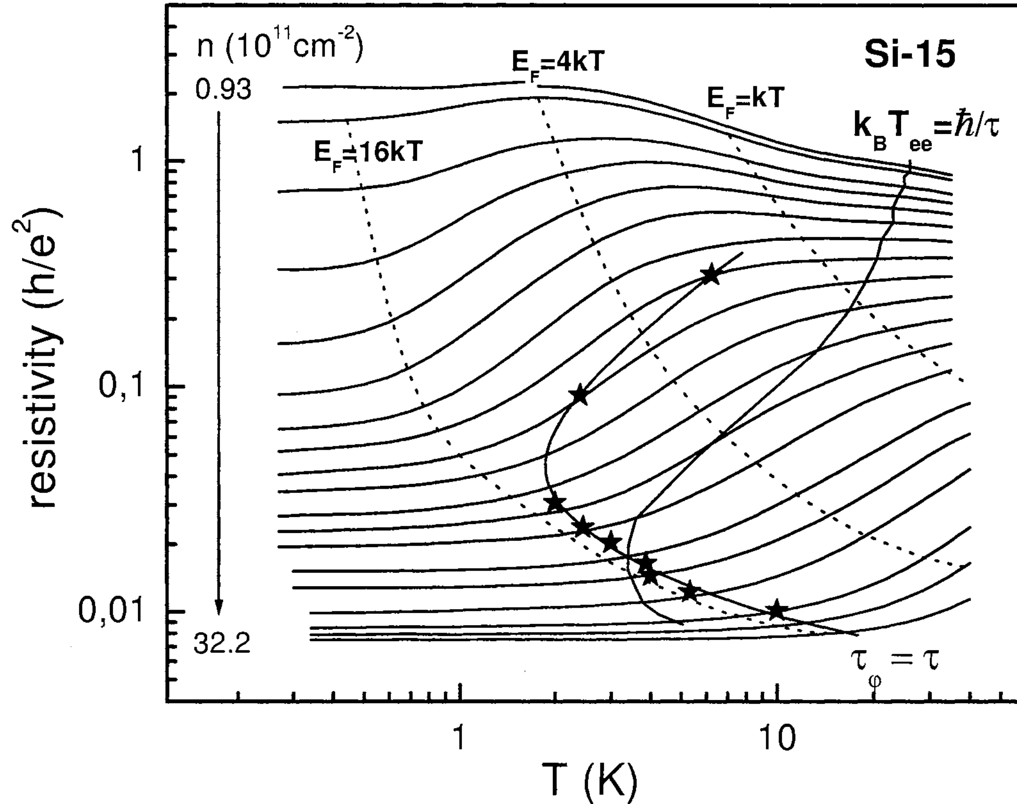

Figure 1.13. Temperature thresholds in the ρ versus T plane for Si MOSFET. The asterisks mark the threshold T_q for single-electron quantum interference, and the $k_B T_{ee} = \hbar/\tau$ line indicates the threshold for quantum interference effects due to $e-e$ interaction. Dashed lines mark $E_F/i = k_B T$, with $i = 1, 4$, and 16. Experimental ρ vs. T curves are shown for $n = 0.928$, 0.970, 1.09, 1.18, 1.30, 1.45, 1.64, 1.89, 2.22, 2.64, 3.18, 3.88, 4.79, 6.30, 7.95, 10.2, 15.7, 21.2, and $32.2 \times 10^{11}\,\mathrm{cm}^{-2}$. From Brunthaler *et al.* [43].

where $a_B = \epsilon\hbar^2/m^*e^2$ is the effective Bohr radius of the system. The electron-electron interaction energy is much larger than the Fermi energy.

Unfortunately, a reliable theoretical method for such strongly correlated systems is yet to be developed. In most cases, one has to depend on the model instead of the *ab initio* theory.

Various models have been proposed to understand the unusual behavior. There are two trends in constructing the model: quantum transition theories and classical transition theories. The quantum transition theories range from the non-Fermi liquid state to a superconducting state, suggesting that the transition observed is a quantum transition which will survive to zero temperature. On the other hand, the classical transition theories believe that the apparent metallic behavior could be understood by the classical or semi-classical mechanisms, and the metallic behavior may disappear at extremely low temperature.

1.3.1 Quantum Mechanisms

Dobrosavljevic *et al.* [44] present a phenomenological theory about the 2D MIT. After analyzing the scaling theory of localization (Sec. 1.1.2), they concluded that there is no fundamental principle requiring the scaling function $\beta(g)$ be monotonic or negative in 2D for large g limit for 2D systems. Instead, they propose that the scaling function $\beta(g)$ has the expansion,

$$\beta(g) = d - 2 + a/g^{\alpha} + \cdots, \qquad a > 0.$$

Unlike the assumption used in the non-interacting systems, $\beta(g)$ is positive in the large g limit. The corresponding temperature dependence in the metallic phase is,

$$g(T) \sim \ln^{1/\alpha}(T/T_0).$$

To justify the unconventional behavior of β-function, Chakravarty *et al.* [45] proposed that the metallic state is a 2D non-Fermi liquid, which is the result of the strong electron-electron interaction, and could be stable against the weak disorder presented in the system.

The insulating state is supposed to be the Wigner crystal [46]. For a pure system, the Wigner crystallization occurs at extremely low density ($r_s \approx 37$) [6]. However, A recent Quantum Monte Carlo (QMC) calculation shows that the transition could occur at higher density comparable to the observed metal-insulator transition density ($r_s \sim 10$) in the presence of disorder [47]. The Wigner crystal is pinned by the disorder, resulting an insulating behavior. The metal-insulator transition is supposed to be the melting of the Wigner crystal to the non-Fermi liquid.

Although the model provides a complete picture about how the transition occurs, one can get little knowledge about the metallic phase and the insulating phase, since we know little about the *non-Fermi liquid* or disordered Wigner crystal.

A number of models have been based on the superconductivity [48–50]. They considered that the metal-insulator transition is in fact the superconductor-insulator transition. This provides an easy explanation to the existence of the apparent metallic phase, and the strong suppression of the conductivity under the magnetic field. However, there is no experimental evidence that the superconductivity exists in the systems. The existence of the weak localization effect [41,43] at low temperatures directly contradicts to a superconducting state.

Some other theories are based on the perturbative renormalization group approaches. They investigated the interplay between the electron-electron interaction and the disorder. The early work by Finkelstein [51] predicted that the electron-electron interaction may lead to delocalization in a disordered 2D system. The problem was reconsidered by Castellani *et al.* [52] recently and had limited success in predicting the temperature dependence and magnetic field dependence of the metallic phase. A recent analysis by Si and Varma [53] suggests that the electron-electron interaction will be unscreened at low electron densities, at which the system becomes insulating and the compressibility becomes zero. The theory does not provide a explanation to the metallic phase. All the analyses share a common problem that the predicted regime are far beyond the applicable regime of the perturbation. So the applicability of the theories to the 2D MIT is still questionable.

Some numerical simulations have been carried out to study the systems. Benenti *et al.* [54] employ the exact diagonalization on a small lattice cluster with interacting spinless fermions. They found a intermediate density regime between the Wigner crystal phase and the Fermi liquid phase, which may be responsible to the metallic phase observed in the experiments. Denteneer *et al.* [55] carried out a quantum Monte Carlo calculation on a 2D disordered Hubbard model, and found the repulsion between electrons can significantly enhance the conductivity, and $d\sigma/dT$ may change sign at a low temperature. These calculations provide some hints about the behavior of a disordered interacting system. However, due to the great difficulties in calculating the strongly correlated systems, the size of systems and the number of electrons in the simulation are generally very small, so the results are inconclusive.

1.3.2 Semi-classical Theories

Contrary to the quantum transition theories, the semi-classical theories believe that the apparent metallic behavior (strong resistivity drop) is due to semi-classical mechanisms. The fate of these apparent metallic states at the low temperature is thus questionable.

Klapwijk and Das Sarma [56] proposed a theory based on the scattering between the electrons and the charge impurities. They showed that it could lead to very large magnetoresistance if the electrons number is comparable to the number of impurities. The system becomes insulating if all electrons are captured by the charged impurities. Following the line, Das Sarma and Hwang [57] calculated the temperature dependence of the resistivity on the metallic side. They found the non-monotonic behavior of the temperature dependence of the resistivity, which is observed in experiments, can be deduced from the model if a temperature dependent screening of the scattering between the electrons and the impurities is supposed. However, the theory tends to overestimate the temperature where the strong resistivity drop occurs.

Another line of the semi-classical theory is percolation theory [26,58], which will be discussed in detail in Sec. 1.4. The basic idea is that the strong electron-electron interaction and the disorder lead to the redistribution of the electrons: they form

some high density conducting regions and some low density insulating regions. The metal-insulator transition is the percolation transition of the high density conducting regions. The theory can explain many aspects of the experiments, and is consistent with some recent experiments [39,40].

1.4 Percolation Model

The percolation mechanism provides a new understanding to the observed metal-insulator transition. The model was proposed by He and Xie [26].

One of the striking features of the system is the I-V nonlinearity (see Sec. 1.2.2) at average electric fields much weaker than the expected value determined by the effective temperature of the electrons [25]. This raises questions of whether the system can be described by a theory for homogeneous systems. On the other hand, a slowly-varying disorder potential combined with electron-electron interaction may favor macroscopic inhomogeneity in the system, which will be discussed in detail in next chapter.

Once the system becomes inhomogenous, the electrons will form some high and low density regions. High density region has higher local conductivity comparing with the low density region. The system could be considered to be composed by two phases, high density *liquid* phase and low density *gas* phase. The liquid phase has lower energy with a cohesive energy Δ_c, while the gas phase could be disorder-pinned Wigner crystal phase. When increasing the density, the liquid phase percolates through the system, and drives the system into the metallic state.

Some simple arguments can be made to explain the experimental findings.

1.4.1 Temperature Dependence of The Resistivity

One of the most striking features of the experiments is that the temperature dependence of the resistivity changes from insulator-like to metal-like as the average electron density increases. This is readily understood in the theory. At a low enough average density, the system is in the two-phase regime. When the average density

is below the threshold density of the percolation, the conduction in the system is dominated by the phonon-assisted hopping through the localized gas phase. At low enough temperatures, this gives the Coulomb-gap behavior [12]

$$\rho \sim e^{\sqrt{E_0/T}},$$

where E_0 is an energy scale determined by the localization length and the Coulomb interaction. On the other hand, when the average density is above the threshold density, the metallic liquid phase percolates through the whole system. The system is able to conduct electric current. Using a simple two-fluid model for the conduction, we have

$$\sigma = f_l \sigma_l + f_g \sigma_g \quad \text{and} \quad f_l + f_g = 1,$$

where f_l and f_g are respectively the fractions of the electrons in the liquid and the gas phases. σ, σ_l, and σ_g are respectively the total conductivity, the conductivity of the liquid and the conductivity of the localized gas. If supposed At temperatures much lower than the cohesive energy Δ_c of the liquid, we estimate f_g to be

$$f_g \simeq A e^{-\frac{\Delta_c}{T}}.$$

Combining the above equations, we obtain the low temperature behavior of the resistivity on the metallic side

$$\rho = \tilde{\rho}_0 + \tilde{\rho}_1 e^{-\frac{\Delta_c}{T}},$$

where $\tilde{\rho}_0 = 1/\sigma_l$ and $\tilde{\rho}_1 = A\tilde{\rho}_0(1 - \sigma_g/\sigma_l)$. This temperature dependence of ρ on the metallic side is consistent with the experimental findings. On the other hand, For higher temperature $T > \Delta_c$, the liquid phase is evaporated and ceases to exist. The resistivity of the system depends weakly on temperature.

1.4.2 Scaling and Duality

When the system approaches the critical point n_c, there is a diverging length scale ξ and a vanishing energy scale $\varepsilon \sim e^2/\xi$. Using the usual arguments [27], in the region close to the critical point, we write the finite temperature resistivity of the

system in the scaling form

$$\rho(T,n) = \tilde{\rho}(\delta/T^{1/\nu}),$$

where $\delta = (n - n_c)$ and ν is the correlation length exponent. The value of ν predicted by the percolation theory is $\nu = 4/3$. This is very close to the measured values of $1.5 - 1.9$ (see Sec. 1.2.3).

The duality observed in the experiments can be readily understood by the following argument. Because there is no other critical point at a finite temperature, the function $\tilde{\rho}(x)$ is an analytic function of its variable. Taylor expanding it at $x = 0$, we have

$$\rho(T, n_c + \delta) = \tilde{\rho}^{(0)} + \tilde{\rho}^{(1)}\frac{\delta}{T^{1/\nu}} + \frac{1}{2}\tilde{\rho}^{(2)}(\frac{\delta}{T^{1/\nu}})^2 + \cdots,$$

where $\tilde{\rho}^{(0)} = \tilde{\rho}(0)$, $\tilde{\rho}^{(1)} = \frac{d\tilde{\rho}(x)}{dx}|_{x=0}$, and $\tilde{\rho}^{(2)} = \frac{d^2\tilde{\rho}(x)}{dx^2}|_{x=0}$. Immediately we have

$$\rho(T, n_c + \delta)\rho(T, n_c - \delta) = (\tilde{\rho}^{(0)})^2 + O(\delta^2).$$

Obviously, this operationally defined duality relation is a generic feature of the critical region.

1.4.3 Electric-Field Dependence of The Resistivity

There are two important features associated with the electric-field experiments [25]. First, the nonlinear $I - V$ occurs at very small electric field. Second, the nonlinear resistivity exhibits scaling as a function of electric field in both the metallic and insulating sides. There are two known mechanisms through which nonlinearity can occur in a homogeneous system [27]. The first one requires that the energy scale determined by the electric field to be the dominant energy scale in the system. In the critical region, this energy should be larger than the temperature. However, in a typical nonlinear $I - V$ experiment in Si MOSFETs, the nonlinearity occurs at electric fields as low as 0.25 mV/cm [25]. Using a phase breaking length of 10000Å, one estimates the nonlinear electric field energy scale to be about 0.3mK, much smaller than the temperature 220mK. No nonlinearity should result from this mechanism. The second mechanism is due to Joule heating. Joule heating raises the effective

temperature T_e of the electrons according to $T_e \sim E^{1/2}$ [59]. The experiments indicate that T_e is about 2K at an electric field of 50mV/cm. Using an electric field of 0.25mV/cm, one estimates T_e to be 150mK. This is lower than the lattice temperature 220mK. Therefore Joule heating is not significant at such an electric field and no nonlinearity should result. The above arguments indicate that the nonlinear $I-V$ may be caused by the intrinsic inhomogeneity in the system.

The scaling behavior appeared at large electric fields can be readily understood by the following arguments [27]. Close to the critical point, the vanishing energy scale $\epsilon \sim e^2/\xi$ is cut off by the electric field through $\epsilon \sim eE\xi$. Thus, the zero temperature resistivity can be written in the scaling form

$$\rho(E,n) = \tilde{\rho}(\delta/E^{1/\nu(z+1)}),$$

where $z = 1$ because the vanishing energy scale at the critical point is given by $\epsilon \sim e^2/\xi$. Using the classic value of $\nu = 4/3$, it is found $\nu(z+1) = 8/3 \simeq 2.66$, which is very close to the experimental value of 2.70 [25].

1.4.4 Effects of An In-Plane Magnetic Field

When an in-plane magnetic field is applied, the electrons begin to be polarized. On the other hand, the gas phase is much easier to be polarized than the liquid phase, as shown in the quantum Monte Carlo calculation by Tanatar *et al.* [6]. So for the small magnetic field, the energy gap between the liquid and gas phases decreases linearly with the magnetic field. When the Zeeman energy of the magnetic field is larger than the Fermi energy of the gas phase, it fully polarizes the electrons in the gas phase. The portion of electrons in the gas phase at low temperatures can be estimated to be

$$f_g \sim e^{\frac{g\mu_B S_z H_{||} - \Delta_c}{T}}$$

when $g\mu_B S_z H_{||} < \Delta_c$. Using the two-fluid model above, we find the in-plane magnetic field dependence of the resistivity on the metallic side at low temperatures to be

$$\rho \sim \rho_0 + \rho_1 e^{g\mu_B S_z H_{||}/T}$$

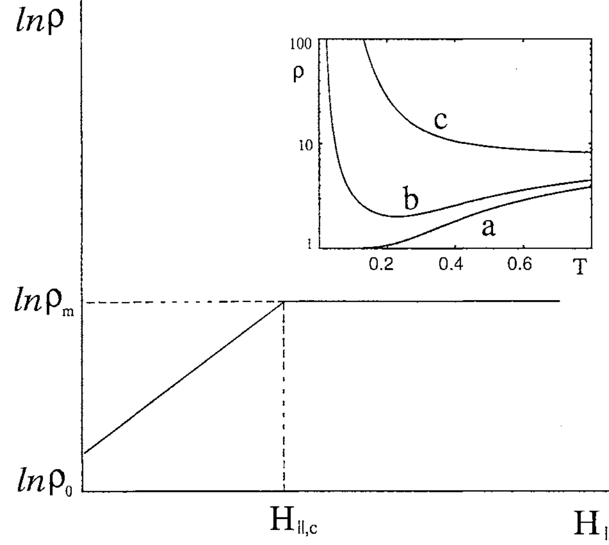

Figure 1.14. In-plane magnetic field dependence of the resistivity. The Inset shows the temperature dependence of ρ for various in-plane magnetic fields: (a) $H_{||} \ll \tilde{H}_{||,0}$, (b) $H_{||} < \tilde{H}_{||,0}$, (c) $H_{||} > \tilde{H}_{||,0}$. The temperature is measured in unit of $g\mu_B S_z H_{||,c}$. From He and Xie [26].

When the Zeeman energy goes beyond Δ_c, the liquid phase ceases to exist because the critical temperature T_c is zero. The system is a fully polarized gas and it is not affected by further increases of $H_{||}$. Fig. 1.14 shows this generalized situation for a given temperature T. The resistivity increases exponentially with H from its zero-field value $\rho_0(T)$ to the saturated value $\rho_m(T)$ at the critical field $H_{||,c}$ given by $g\mu_B S_z H_{||,c} = \Delta_c$, *i.e.*

$$\ln\rho(T, H_{||}) = \begin{cases} \ln\rho_0(T) + \frac{H_{||}}{H_{||,c}}(\ln\rho_m(T) - \ln\rho_0(T)) & \text{if } \mathrm{H}_{||} < \mathrm{H}_{||} \\ \ln\rho_m(T) & \text{if } \mathrm{H}_{||} > \mathrm{H}_{||,c} \end{cases} \tag{1.9}$$

When $T \ll g\mu_B S_z H_{||,c}$, $\rho(T, H_{||})$ should be exponential in $H_{||}/T$ for intermediate values of $H_{||}$. Using this we have

$$\ln\rho_m(T) \sim \ln\tilde{\rho}_m + \frac{g\mu_B S_z H_{||,c}}{T}. \tag{1.10}$$

Next we look at how the low temperature behaviors of the resistivity on the metallic side evolve for different in-plane magnetic fields. Using Eqn. 1.9 and Eqn. 1.10, we have

$$\ln\rho(T, H_{||}) = (1 - \frac{H_{||}}{H_{||,c}})\ln\rho_0(T) + \frac{g\mu_B S_z H_{||}}{T} + \frac{H_{||}}{H_{||,c}}\ln\tilde{\rho}_m.$$

This equation predicts different behaviors of $\rho(T, H_{\|})$, shown in the inset of Fig. 1.14, for $H_{\|} < H_{\|,0}$ and $H_{\|} > H_{\|,0}$, where $H_{\|,0} = \tilde{\rho}_1 H_{\|,c}/(\tilde{\rho}_0 + 2\tilde{\rho}_1)$. Using the experimental data of $\tilde{\rho}_1/\tilde{\rho}_0 \simeq 10$ and $H_{\|,c} \simeq 20$ kOe in the experiments of Simonian *et al.*, we predict $H_{\|,0} \simeq 10$ kOe. This is consistent with the experiments. For $H_{\|} \ll H_{\|,0}$, the temperature T_m at which $\rho(T, H_{\|})$ reaches a minimum is given by

$$T_m \sim \frac{\Delta_c}{\ln(\frac{\Delta_c}{g\mu_B S_z H_{\|}})}.$$

1.4.5 Further Works

The percolation theory provides a framework to understand the experimental findings. However, some issues have to be addressed:

(1) The formation of the two phases. One has to understand the underlying mechanism in the formation of the inhomogenous ground state. The problem will be discussed in Chapter 2.

(2) The transport behavior of the system. The percolation model provides a classical mechanism to understand the experiments. However, at low temperatures, the quantum effect becomes more and more important. In a typical experimental setup, the lowest temperature could reach 30 mK. How a classical model can be valid for a low temperature system and the quantum effect to a semi-classical system are the problems to be discussed in Chapter 3.

CHAPTER 2

Droplet State

A noticeable character of the electron system in the experiments is that r_s, the parameter measuring the strength of the Coulomb interaction (Eq. 1.8), is fairly large. The electron system may be unstable against phase separation at these large values of r_s. For a two-dimensional (2D) electron system, there believed to be two phases: a high density Fermi gas phase and a low density insulating Wigner crystal phase. The dielectric constant of the liquid phase becomes negative when $r_s \simeq 2$ [60], which indicates that the liquid phase is unstable. At lower densities, the Wigner crystal phase appears around $r_s \simeq 37$ in the absence of disorder [6]. This critical value of r_s appears to be reduced with disorders [47]. In the intermediate values of r_s, we believe that there is a phase separation which we think is responsible for the observed MIT.

We propose that a droplet state of the electron system resulted from the phase separation of the electrons into this new liquid phase and a low density "gas" phase. Here we call the low density phase "gas" purely for the reason that its density is low. In fact, in the presence of impurities, the "gas" phase may be disordered Wigner crystal. In this chapter, we study the energetics of such a droplet state. We find that both electron-electron interaction and disorder potential are crucial for the formation of the droplet state. Moreover, A density functional calculation based on local density approximation (LDA) is carried out the simulate the density distribution of the system.

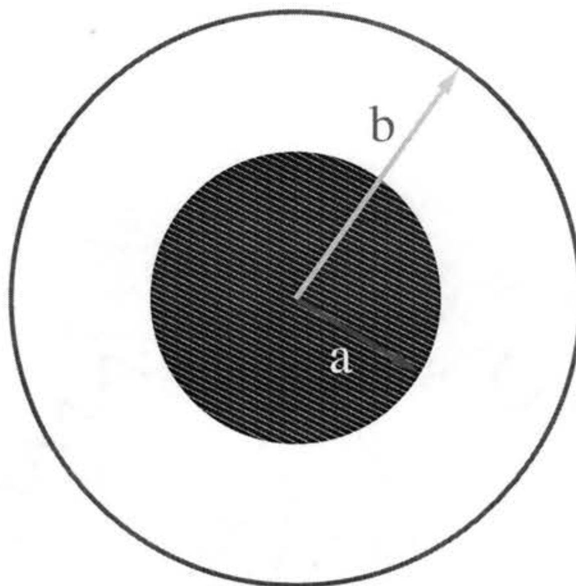

Figure 2.1. A simple model to investigate the shrinking of the electron distribution. The electron is uniformly distributed in a disc with radius b, and is shrunk to a smaller radius a.

2.1 Energetics Consideration

2.1.1 Model

An obvious condition for the droplet state is that the electron gas is unstable. To investigate what possibilities of the instability leads to, we study a simple but physically motivated model. Let us consider electrons in the disc of radius b with uniform positive background. Imagining that the electron system is shrunk to a new radius $a < b$ while the positive background remains intact. Clearly the charging energy due to the separation of the electrons from the positive background increases the energy of the system. However there can also be energy gained (decreasing total energy): since for a uniform electron gas the ground state energy E_g is at its minimum when $r_s \simeq 2$ [60], for $r_s > 2$ the system gains energy by shrinking the area occupied by electrons. Furthermore, in the presence of disorder, electrons tend to occupy the valleys of the disorder landscape. Thus, a slowly varying disorder potential is in favor for the formation of the droplet state. We calculate the energy changes when electron

disc is shrunk from b to a to determine whether a spontaneous shrinking can take place.

For electron-electron or electron and positive background interaction, we use screened Coulomb potential. For Si MOSFETs, the image charge in the metal substrate induces the screening and the interaction in the momentum space can be written as [61]

$$V(k) = \frac{1}{\varepsilon}\frac{2\pi e^2}{k}\frac{1-e^{-2kD}}{1-Ke^{-2kD}},$$

where D is the thickness of the SiO_2 insulating layer and $\varepsilon = \frac{1}{2}(\varepsilon_1+\varepsilon_2)$, $K = (\varepsilon_1-\varepsilon_2)/(\varepsilon_1+\varepsilon_2)$, with ε_1 and ε_2 being the dielectric constants of Si and SiO_2, respectively. For other systems, such as GaAs/AlGaAs, the screened interaction can be well represented by the following form:

$$V(r) = \frac{e^2}{\varepsilon r}e^{-\lambda r},$$

and the corresponding moment space representation is,

$$V(k) = \frac{2\pi e^2}{\varepsilon}\frac{1}{\sqrt{k^2+\lambda^2}}.$$

Both forms of the interactions define an interaction range ξ. For Si MOSFETs, $\xi = (\varepsilon/\varepsilon_2)D$, and for the screened Coulomb potential, $\xi = 1/2\lambda$. Outside the range the interaction is strongly screened.

2.1.2 Ground State Energy

To calculate the ground state energy of the electron gas with the screened Coulomb interaction, we use the variational correlated-basis-function (CBF) method [62]. This method has been applied to the bare Coulomb interaction and is proved to provide rather accurate result for the ground state energy of 2D electron system. The accuracy of the ground state energy is found to within 10% comparing with the best available quantum Monte-Carlo results [6] for densities down to $r_s = 20$. In the CBF approach, there is a variational variable α for which the ground state energy E_g has to be minimized,

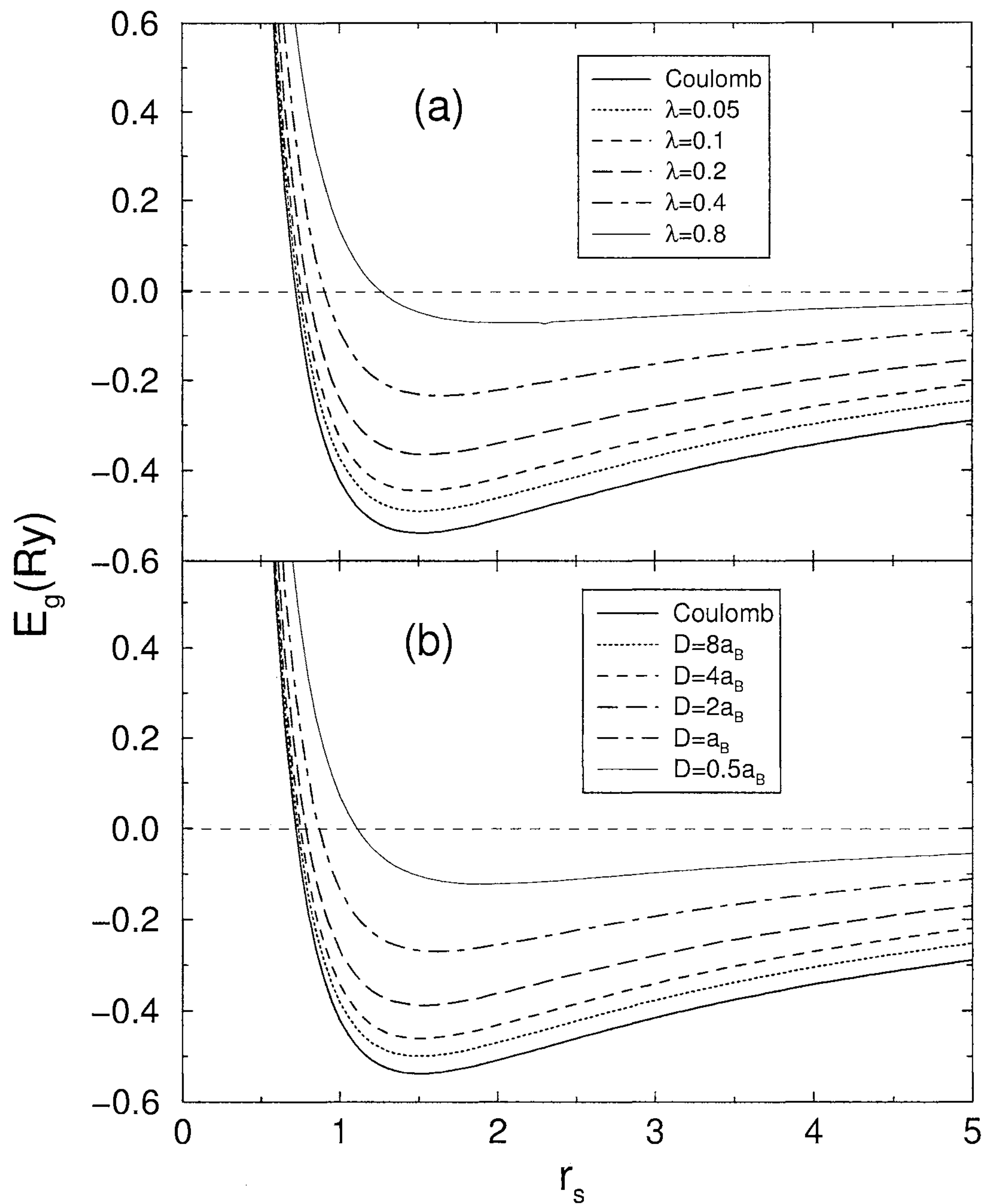

Figure 2.2. The ground state energy of electron system for different screening strength: (a) for screened Coulomb interaction, (b) for Si MOSFETs.

$$
\begin{aligned}
E_g(r_s,\alpha) &= \frac{A(\alpha)}{r_s^2} - U_c\left(\frac{\sqrt{\alpha}}{r_s}\right) \quad \text{(Ry.)} \\
A(\alpha) &= A_0^B(\alpha) + A_{01}^F(\alpha) + A_{02}^F(\alpha) + A_{03}^F(\alpha) + \cdots \\
A_0^B(\alpha) &= \alpha^2 \left[\sum_{n=0}^{\infty} \frac{\alpha^n}{(n+2)^2} + \frac{\pi^2}{6} - \frac{5}{4}\right] \\
A_{01}^F(\alpha) &= 1 \\
A_{02}^F(\alpha) &= -\frac{16}{\pi}\int_0^1 \left[2\arccos(y) - y(1-y^2)^{1/2}\right] \\
&\quad \times y^3 e^{-2y^2/\alpha} dy \\
A_{03}^F(\alpha) &= -\frac{2}{\pi}\int_0^1 dy_1 \int_0^1 dy_2 \int_0^1 dy_3 \int_0^{\pi} d\theta y_{12}^2 \\
&\quad \times \left\{1 - \exp\left[-y_{12}^2/2\alpha\right]\right\} \\
&\quad \times \exp\left[-\left(y_1^2 + y_2^2 + 2y_3^2\right)/2\alpha\right] \\
&\quad \times I_0\left[\alpha^{-1}\left(y_1^2 y_3^2 + y_2^2 y_3^2 + 2y_1 y_2 y_3^2 \cos\theta\right)^{1/2}\right],
\end{aligned}
$$

where $1\text{Ry} = e^2/2\varepsilon a_B$, $a_B = \varepsilon\hbar^2/m^* e^2$, and $y_{12} = y_1 - y_2$. U_c is the cohesive energy which depends on the special form of the interaction,

$$
U_c(x) = \frac{1}{2}\int \exp\left[-\left(\frac{k}{2x}\right)^2\right] V(k) \frac{d^2k}{(2\pi)^2}.
$$

Fig. 2.2 shows the calculated results for the ground state energy. The screening effect raises the ground state energy because the electron correlation is suppressed.

For the low density (large r_s), it can be clearly seen that the ground state energy will be lower if the electron disc is shrunk to higher density.

2.1.3 Electrostatic Energy

However, the shrinking of the electron disc will cause the redistribution of the charge, which will raise extra electrostatic energy due to the fixed positive background. The charge distribution in the momentum space can be written as

$$
\rho(k) = 2N\left(\frac{J_1(ka)}{ka} - \frac{J_1(kb)}{kb}\right),
$$

where N is the total number of the electrons in the disk. The charging energy is

$$E_c = \frac{1}{2N}\int \frac{d^2k}{(2\pi)^2} V(k)|\rho(k)|^2$$
$$= \frac{1}{\pi a_B^2 r_s^2}\int_0^\infty \frac{dx}{x} V\left(\frac{x}{b}\right)\left(\frac{J_1(\gamma x)}{\gamma} - J_1(x)\right)^2,$$

where $\gamma = a/b$ is the ratio of the radii after and before shrinking electron disc. The charging energy shows distinct forms for different interaction ranges. When the interaction range ξ is much larger than the radius of the disk, $\xi \gg b$, the electron-electron interaction can be roughly considered as the bare Coulomb interaction. In this case, the electrostatic charging energy is

$$E_c \approx \frac{4b}{r_{s0}^2}\left(0.290545 - \frac{1}{\pi}\ln|1-\gamma|\right)(1-\gamma)^2 + \cdots \quad \text{(Ry)}.$$

In the other limit $b \gg \xi$, the interaction is well screened and the electrostatic energy has the form,

$$E_c = 4\xi\left|\frac{1}{r_s^2} - \frac{1}{r_s'^2}\right| \text{ Ry},$$

where r_s and r_s' are the inverse density parameters before and after the shrinking.

2.1.4 Shrinking Without Disorder

The total energy difference can be written as

$$\Delta E_{tot} = E_c(\gamma) + \Delta E_g.$$

For a small initial radius $b \ll \xi$, the energy gain ΔE_g dominates over the energy loss E_c, thus, there is always finite shrinking.

However, the above conclusion is not true in general as demonstrated in Fig. 2.3. Fig. 2.3 shows the shrinking distance $\Delta b = b - a$ versus initial radius b. Δb approaches a constant for large b. However, the shrinking shown here can not be considered as a macroscopic shrinking because the typical Δb is only about $2a_B$, which is far smaller than the average distance between the electrons, which is $r_s = 15a_B$ for this calculation. Similar behavior has also been observed for other values of r_s.

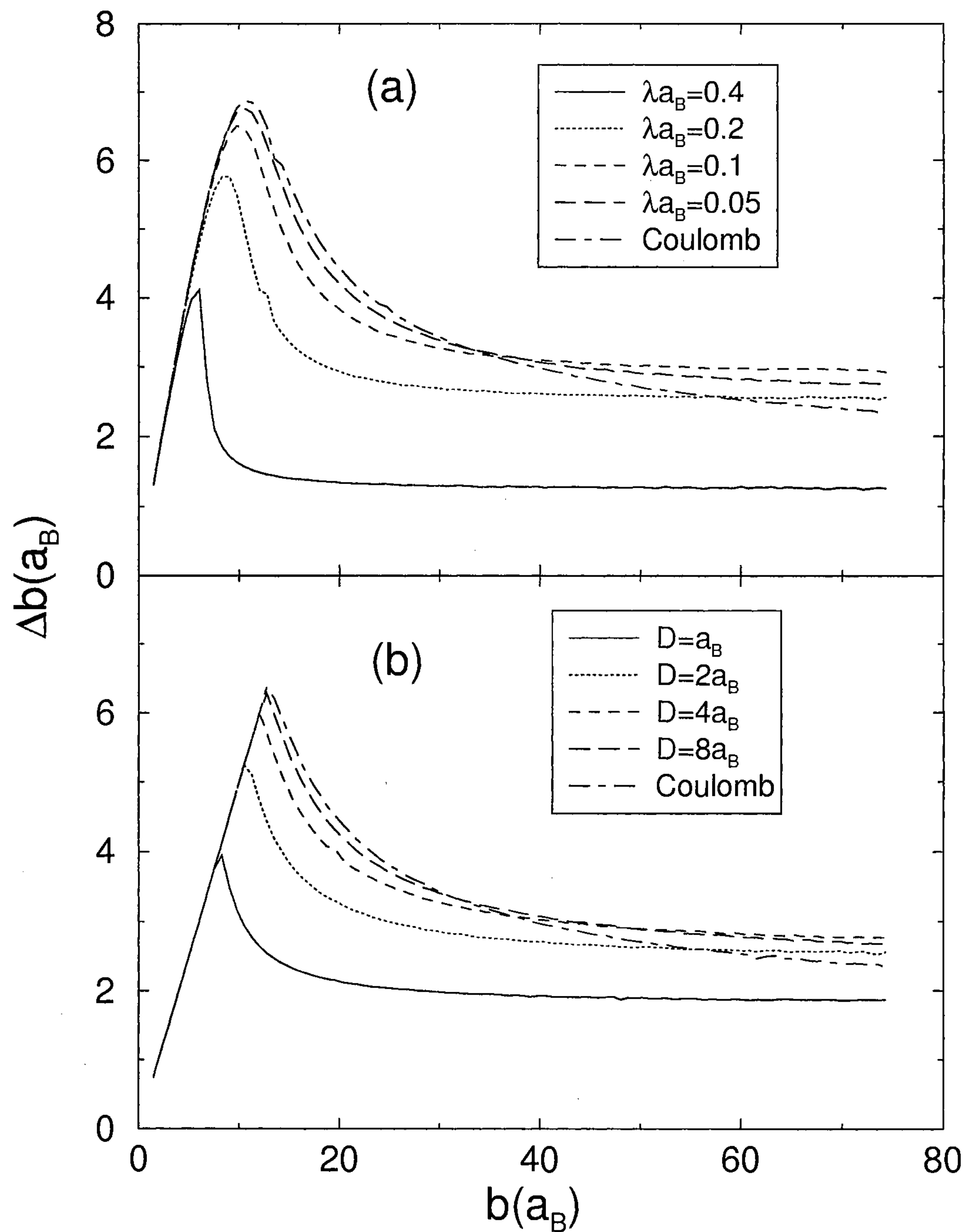

Figure 2.3. The shrinking distance $\Delta b = b - a$ versus disc radius b for different screening strength. (a) for screened Coulomb potential; (b) for Si MOSFETs. The initial density parameter $r_s = 15a_B$.

2.1.5 Disorder Effect

Thus the intrinsic instability is not sufficient to overcome the charging energy cost in order to form the electron droplet state. The system is in a marginally stable situation. However, in real systems, there are always disorders. The low frequency component of a disorder potential forms the potential landscape, and electrons tend to occupy the low potential valleys. We assume that around each local minimum, the disorder potential is isotropic and slowly varying. We expand the disorder potential around the local minimum up to the quadratic term. Therefore, we adopt the following simple model for disorder potential

$$W(r) = V_0 \frac{r^2}{b^2},$$

where V_0 is the potential depth from center to edge of the disc. The energy gain by shrinking to a radius a can be evaluated as

$$\begin{aligned} \Delta E_W &= \Delta \frac{1}{N} \int W(r) \rho(r) dS \\ &= \frac{V_0}{2} \left(\gamma^2 - 1\right). \end{aligned}$$

The total energy difference in the limit $b \gg \xi$ can be written as

$$\Delta E_{tot} = -\left(\frac{V_0}{2} - \frac{4\xi}{r_{s0}^2}\right)(1-\gamma^2) + \Delta E_g.$$

The effect of the electrostatic energy will be suppressed by the potential fluctuation. Large value of V_0 is in favor for the disc to shrink.

Fig. 2.4(a) plots the $\Delta b = b - a$ as a function of the initial radius b for Si MOSFETs with $D = 10a_B$ and $r_s = 15a_B$. There exists a critical V_0^c (~ 0.08) above which $\Delta b \propto b$. Thus, for large b there is a macroscopic shrinking for $V_0 > V_0^c$. Similar result has also been obtained for the screened Coulomb interaction with $1/\lambda$ places the role of D. In Fig. 2.4(b) we plot the energy change as a function of the initial radius b. It is clear that larger value of V_0 gives rise to larger energy gain. We have carried out the calculations for many values of r_s and the resulting phase diagrams are plotted in Fig. 2.5.

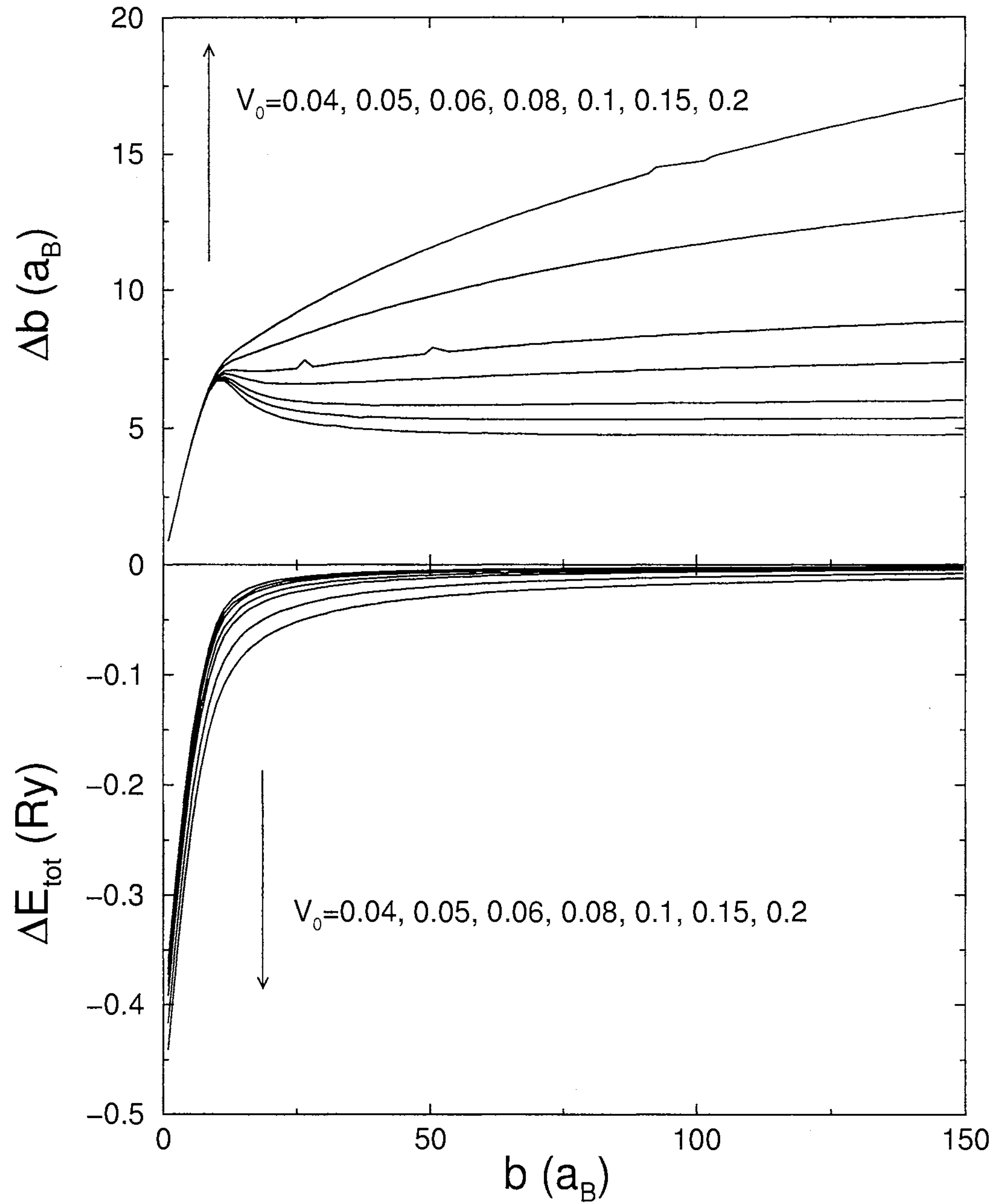

Figure 2.4. (a) The shrinking distance $\Delta b = b - a$ versus radius b for Si MOSFETs with $D = 10a_B$. Top curves are for larger disorder potential V_0's. (b) ΔE_{tot} versus radius b. Lower curves are for larger disorder potential V_0's. The initial electron density parameter $r_s = 15a_B$.

Fig. 2.5 shows the phase diagram in the $r_s - \xi$ plot for the case of $b \gg \xi$. Each value of V_0 corresponds to a curve in the figure. The curves for larger V_0 are above those for smaller V_0. On the right side of the curve for a given V_0, the electron disc will have a macroscopic shrinking, thus, an electron droplet phase is stable. To form the electron droplet state, the screening of the electron-electron interaction and the potential fluctuation are both crucial. The smaller interaction range between the electrons and the lower electron density, the easier to form the droplet phase.

2.1.6 Conclusion

From the energetics consideration, it is possible to have a droplet phase for 2D electron systems at low densities. Both electron-electron interaction and disorder potential fluctuations are important for the formation of the droplet phase.

We would like to make several comments.

(i) We only consider one electron disc, corresponding to one drop in the droplet state. In real systems, electrons tend to occupy valleys of potential fluctuations to give rise many such drops. The size of each drop is determined by local potential depth.

(ii) We only consider zero temperature effect, so the "gas" phase is empty. At a finite temperature, The "gas" phase is occupied by lower density electrons. Thus, a finite temperature enhances the possibility for the droplet state since the density difference between the liquid and the "gas" is smaller and the charging energy is less costly. However, in order to form the droplet state, the temperature has to be below the cohesive energy (the energy cost to remove an electron from the liquid phase to the "gas" phase [26]).

(iii) In order to have a percolation, the "gas" phase needs to have a much smaller local conductivity than the liquid phase. This requires that a typical length scale of the "gas" region is larger than the localization length of the "gas" phase. The "gas" phase is low in electron density which gives rise to a short localization length. Thus, one may not need a large shrinking of electron drops to realize a percolation transition.

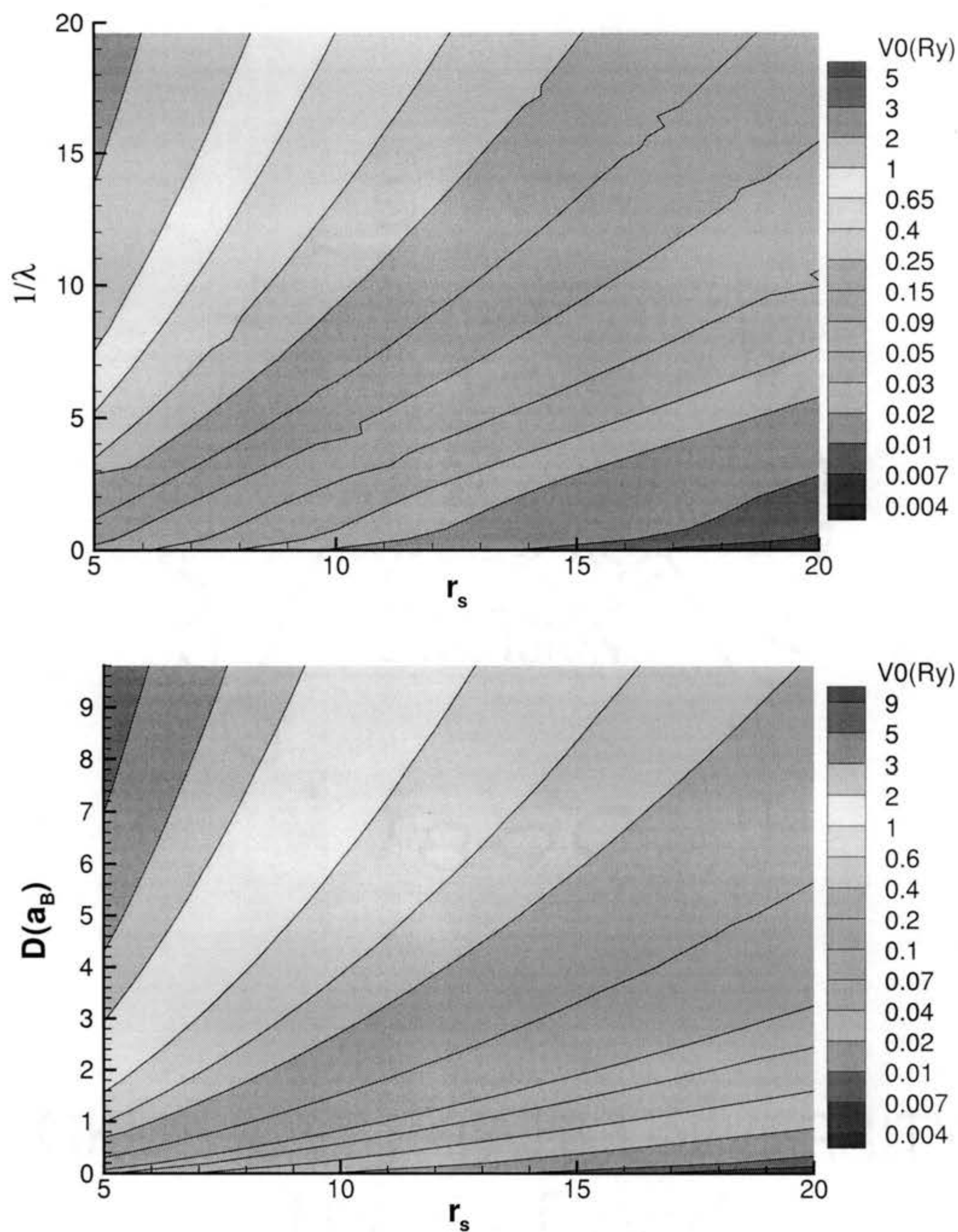

Figure 2.5. The phase diagram in the $r_s - \xi$ plot. r_s is the initial density parameter of the electron disc. D or $1/\lambda$ represents the interacting range ξ of the electron-electron interaction. Each value of V_0 corresponds to a curve in the figure. On the right side of the curve, the electron disc will have a macroscopic shrinking.

2.2 LDA Calculation And Compressibility

The energetics consideration suggests that the 2D system could form the droplet state at the low densities with the help of disorder. In this section, we investigate the space distribution of electron density of 2D electron systems by using the local density approximation. At the same time, the compressibility of the system is calculated, and is found to be consistent to the experimental finding [36].

2.2.1 Model

For the systems with the 2D metal-insulator transitions, it is crucial to deal with the electron-electron interaction in a satisfactory way. Since the theoretical tool to deal with strongly correlated systems is yet to be developed, approximations have to been made in a real world calculation. Local density approximation (LDA) is a good candidate to deal with this class of problems, and is found to be quite accurate in getting the total energy and electron density distribution comparing to the exact diagonalization results [63].

To investigate the density distribution of a disordered 2D electron system, we use the density functional theory. The total energy functional reads,

$$E[\mathbf{n}] = E_T[\mathbf{n}] + E_{ee}[\mathbf{n}] + E_d[\mathbf{n}] + E_x[\mathbf{n}] + E_c[\mathbf{n}].$$

Here $E_T[\mathbf{n}]$ is the functional of the kinetic energy, $E_{ee}[\mathbf{n}]$ is the direct Coulomb energy due to the charge inhomogeneity and $E_d(\mathbf{n})$ is the potential energy due to the disorder. The strong correlation effect caused by the electron-electron interaction is included in the final two terms: $E_x[\mathbf{n}]$ is the exchange energy and $E_c[\mathbf{n}]$ is the correlation energy. The ground state density distribution can be obtained by minimizing the total energy functional with respect to the density.

Using the local density approximation, the total exchange and correlation energies are approximated to depend only on the local density,

$$E_{x(c)}[\mathbf{n}] \approx \int d\mathbf{x} \epsilon^0_{x(c)} \left[\mathbf{n}(\mathbf{x})\right] \mathbf{n}(\mathbf{x}),$$

where $\epsilon^0_{x(c)}(n)$ is the exchange (correlation) energy density for a homogeneous 2D electron system at a given density n, which can be determined by quantum Monte-Carlo calculations. We use the result from Tanatar and Ceperley [6],

$$\begin{aligned} \epsilon^0_x(n) &= -\frac{8}{3}\sqrt{\frac{2}{\pi}}\sqrt{n} \\ \epsilon^0_c(n) &= a_0\frac{1+a_1x}{1+a_1x+a_2x^2+a_3x^3} \end{aligned}$$

where $x = 1/(\pi n)^{1/4}$. The energy unit is $1Ry^* = m^*e^4/2\varepsilon^{*2}\hbar^2$, and the parameters $a_0 = -0.3568$, $a_1 = 1.13$, $a_2 = 0.9052$, $a_3 = 0.4165$.

The kinetic energy functional can be written as

$$E_T[\mathbf{n}] = \int d\mathbf{x} \sum_{s,i} \psi^\dagger_{is}(\mathbf{x}) \left(-\nabla^2\right) \psi_{is}(\mathbf{x}),$$

where the sum is over all occupied quasi-particle energy levels (i) and the spin index (s).

The energy functional for the disorder potential $V_d(\mathbf{x})$ can be written as

$$E_d[\mathbf{n}] = \int d\mathbf{x} V_d(\mathbf{x})\mathbf{n}(\mathbf{x})\,.$$

To simulate the disorder landscape in a real 2D system, two kinds of the disorder are used,

(i) The off-plane charge impurity potential.

$$V_d(\mathbf{x}) = -\sum_i \frac{1}{\sqrt{|\mathbf{x}-\mathbf{x}_i|^2+d^2}}\,,$$

where d is the distance between the electron and the impurity planes, and the impurities are randomly distributed with a density n_i.

(ii) The correlated disorder potential with the correlation between the different positions:

$$\langle V_d(\mathbf{x})V_d(\mathbf{x}')\rangle = V_s^2 \exp\left(-\frac{|\mathbf{x}-\mathbf{x}'|}{\xi}\right)\,,$$

where V_s is the amplitude of the potential fluctuation, and ξ is the correlation length of the disorder. The model simulates a slowly varied disorder potential, and ξ is roughly the average size of valleys in a disorder landscape.

The density distribution of the ground state can be obtained by minimizing the energy functional under the constraint of a constant total electron number. One gets the effective single particle Schödinger equation,

$$\left[-\nabla^2 + V_{sc}[\mathbf{n},\mathbf{x}]\right]\psi_{is}(\mathbf{x}) = \epsilon_{is}\psi_{is}(\mathbf{x}) \tag{2.1}$$

where

$$V_{sc}[\mathbf{n},\mathbf{x}] = V_d(\mathbf{x}) + \frac{\delta}{\delta\mathbf{n}}\left[\epsilon_x^0[\mathbf{n}]\mathbf{n} + \epsilon_c^0[\mathbf{n}]\mathbf{n}\right]$$

is the potential self-consistently determined by the density distribution. The density distribution can be written as,

$$\mathbf{n}(\mathbf{x}) = \sum_{is}|\psi_{is}(\mathbf{x})|^2,$$

where the sum is over all occupied quasi-particle energy levels and the spin index.

To further simplify the calculation, we make an approximation to the kinetic energy so that it can be written in the form of a density functional [64],

$$E_T[\mathbf{n}] \approx \int d\mathbf{x}\left[\pi\mathbf{n}(\mathbf{x})^2 + \frac{1}{4}\frac{|\nabla\mathbf{n}(\mathbf{x})|^2}{\mathbf{n}(\mathbf{x})} + \cdots\right]. \tag{2.2}$$

The first term provides the local density approximation for the kinetic energy, while the second term includes the effect of the density gradient.

To minimize the total energy functional with the constraint of a constant total electron number, we introduce the new variable χ so that,

$$\mathbf{n}(\mathbf{x}) \equiv N\frac{\chi(\mathbf{x})^2}{\int d\mathbf{x}'\chi(\mathbf{x}')^2},$$

where N is the total number of the electrons in the system. The constraint for the constant total electron number is automatically satisfied with the new variable. The steepest descent method [64] is used to minimize the total energy functional to χ,

$$\chi^{m+1}(\mathbf{x}) = \chi^m(\mathbf{x}) - \gamma\frac{\delta E[\chi]}{\delta\chi}\Big|_{\chi=\chi^m(\mathbf{x})},$$

where γ is the iteration constant which is chosen so that the interaction is convergent, and

$$\frac{\delta E[\chi]}{\delta\chi} = \frac{2N}{\int d\mathbf{x}\chi(\mathbf{x})^2}\left[-\nabla^2 + 2\pi\mathbf{n} + V_{sc}[\mathbf{n},\mathbf{x}] - \mu\right]\chi(\mathbf{x}),$$

where

$$\mu = \frac{\int d\mathbf{x}\chi(\mathbf{x})\left[-\nabla^2 + 2\pi\mathbf{n} + V_{sc}[\mathbf{n},\mathbf{x}]\right]\chi(\mathbf{x})}{\int d\mathbf{x}\chi(\mathbf{x})^2}$$

is the chemical potential of the system.

The calculation is carried out in a 128×128 discrete space. The size of the system is set as $L = 256a_B^*$, where a_B^* is the effective Bohr's radius, $a_B^* = \varepsilon\hbar^2/me^2$, with ε being the dielectric constant and m the effective mass of an electron. The periodic boundary condition and the Ewald sum for the Coulomb interaction are applied to minimize the finite size effect. The electron density is adjusted by changing the total electron number N. The density distribution is calculated by using the wave function method (Eq. 2.1), and the chemical potential is calculated by using the gradient approximation (Eq. 2.2), which is found to be accurate in calculating the chemical potential comparing to the results got from wave function method.

The compressibility of the system is calculated by

$$\frac{1}{\kappa} = \frac{N^2}{S}\frac{\partial\mu}{\partial N},$$

where S is the total area of the system.

2.2.2 Density Distribution

Figure 2.6 shows the density distribution of the system. It can be clearly seen that the electrons form some high density regions, while the density of other regions are essentially zero. The boundary of each high density region can be easily identified because the density rapidly decays to zero beyond the boundary. The electron number contained in each high density regions depends on the detail landscape of the disorder. For the specific disorder potential used in the calculation, there are 3-10 electrons in each high density region. Depending on the average density of the system, the high density regions may connect each other together ($r_s = 10$), or form some isolated regions ($r_s = 19$). There exists a certain density ($r_s = 14$) where the high density regions starts to percolate through the system, and form a conducting channel. The calculation clearly demonstrates that the metal-insulator transition observed in the 2D electron systems is the percolation transition of the electron density.

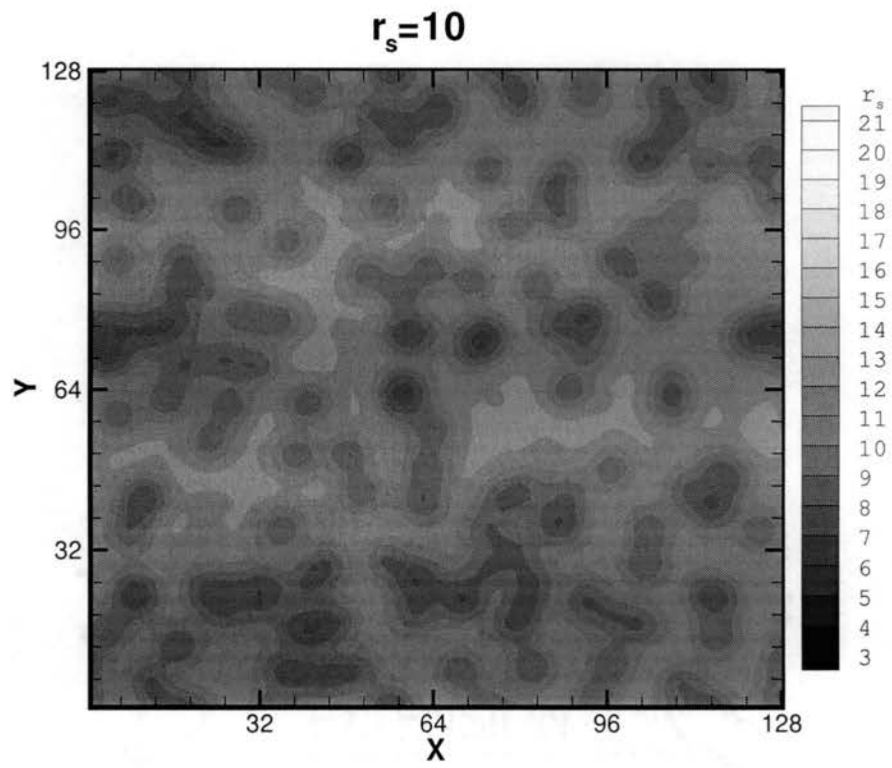
r_s=10
128
96
Y 64
32
32
64
96
128
X
r_s
21
20
19
18
17
16
15
14
13
12
11
10
9
8
7
6
5
4
3

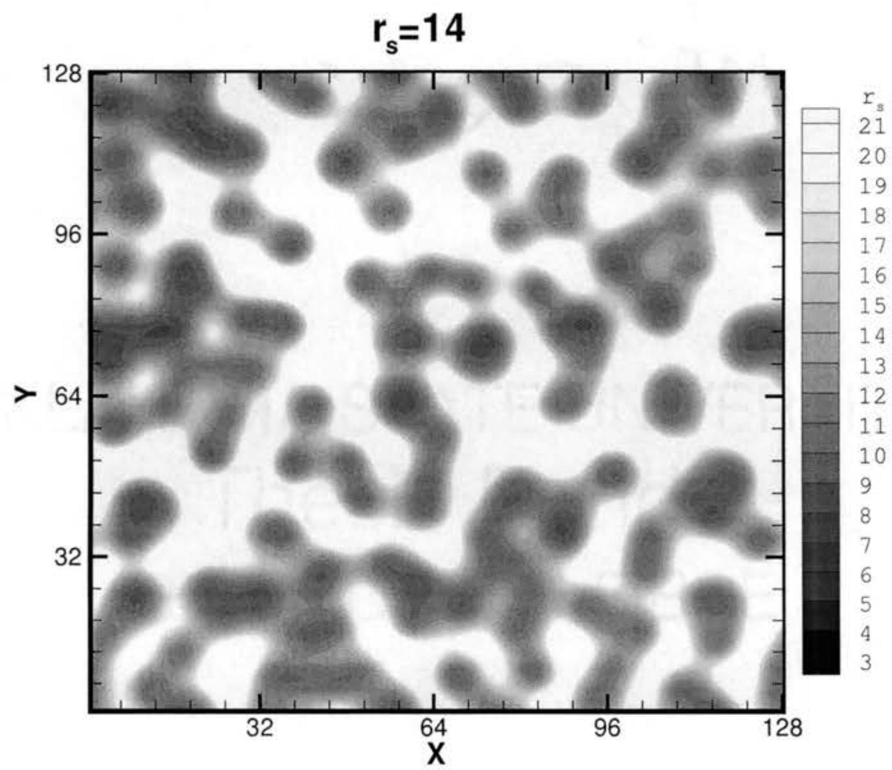
r_s=14
128
96
Y 64
32
32
64
96
128
X
r_s
21
20
19
18
17
16
15
14
13
12
11
10
9
8
7
6
5
4
3

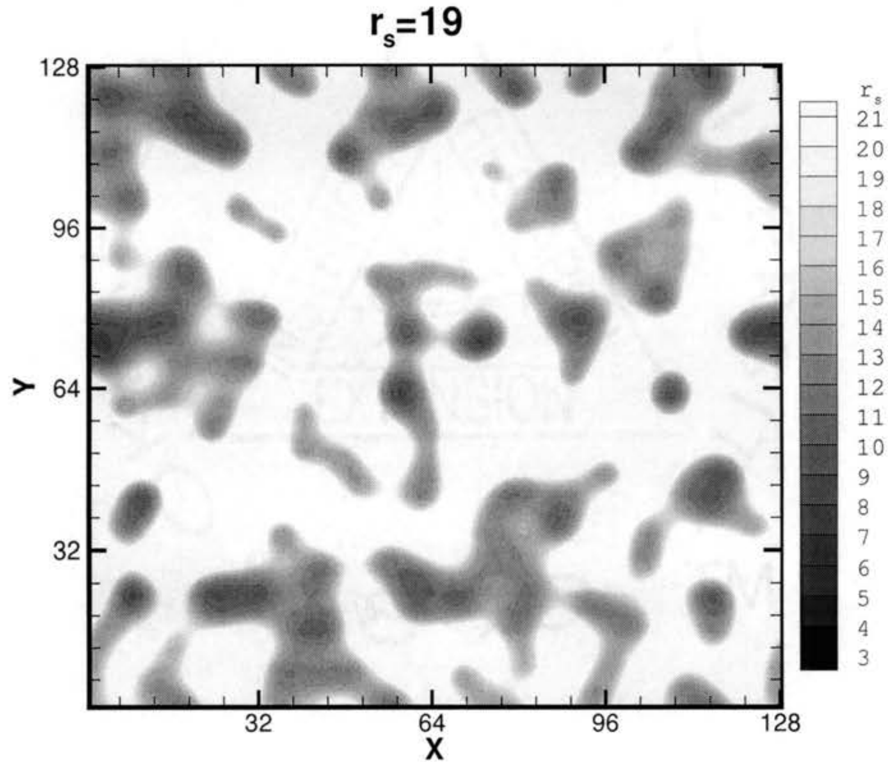

Figure 2.6. The density distributions for the different electron densities. We use the contour plot for the local density parameter $r_s = 1/\sqrt{\pi n}$. The density of the white area decreases rapidly to zero. The disorder potential is generated by off-plane charge impurities with $d = 10a_B^*$, $n_i = 2.5 \times 10^{-3}/a_B^{*2}$.

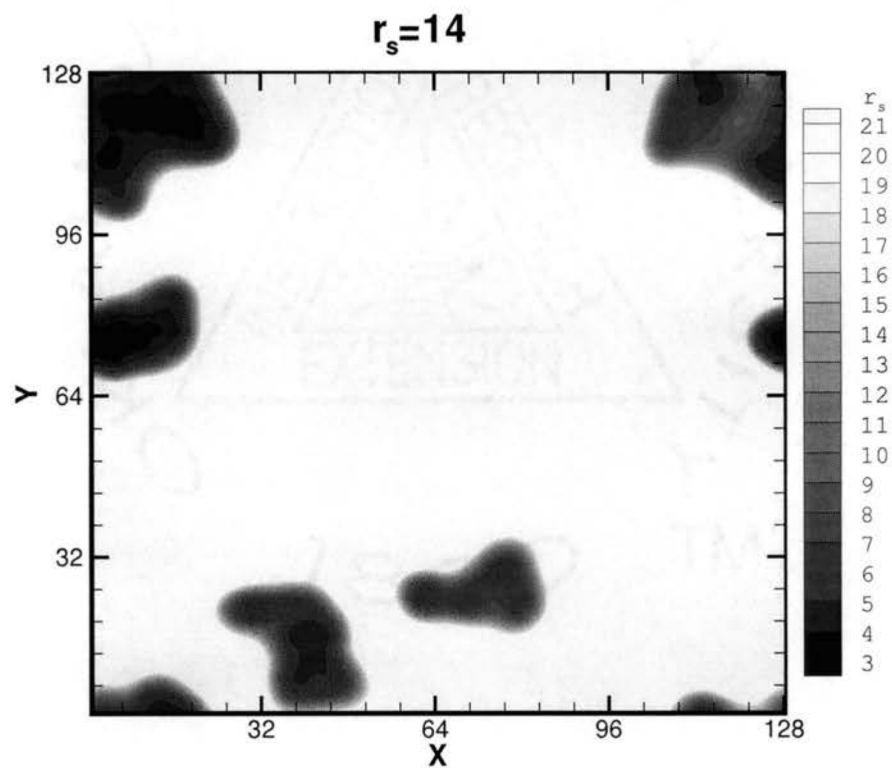

Figure 2.7. The density distribution for the free electron gas on the same disorder landscape as the Fig.2.6 at density $r_s = 14$.

The electron-electron interaction is important for the conducting behavior of a dilute electron system in the sense that it makes the density distribution more extended because of the Coulomb repulsion. Figure 2.7 shows the density distribution for the free electron gas with the same density as in Fig. 2.6(b) by turning off the electron-electron interaction. The system only forms some isolated high density regions at the disorder valleys, while the density distribution of the corresponding interacting system (Fig. 2.6(b)) is quite extensive at the same density. At a given disorder strength, the critical density for the free electron gas is much higher than its interacting counterpart.

2.2.3 Compressibility

Figure 2.8 shows the compressibility of the systems. To compare with the experiments [36–38] (see Sec. 1.2.5), we calculate $\delta\mu/\delta N$, which is the direct measured quantity in the experiments. It is well known that the compressibility of a uniform electron gas is negative in the low density region due to the effect of the exchange and correlation energies, as shown by the solid line in Fig. 2.8(a). However, when the disorder is present, the behavior changes greatly. In the low density, the electrons tend to occupy the valleys of the disorder landscape, and the local density, instead of the average density, determines the compressibility of the system. On the other hand, at higher densities, all of the valleys are filled, one can expect the compressibility of the system to resume the behavior of a uniform electron gas. We have a non-monotonic behavior for $\delta\mu/\delta N$, as shown by the dots in Fig.3(a), which are in good agreement with the experimental measurements [36–38]. Comparing with Fig. 2.6, we find that the turning point of the compressibility ($N \approx 100$, $r_s \approx 14$) coincides with the percolation threshold of the system. At low densities, the data points in the plot show strong fluctuation, indicating the effect of the local fluctuation of the disorder potential.

The behavior can be understood by a simple theory. Following the definition, the chemical potential μ is the energy needed to add an electron into the system,

$$\mu(N) \quad = \quad E(N+1) - E(N)$$

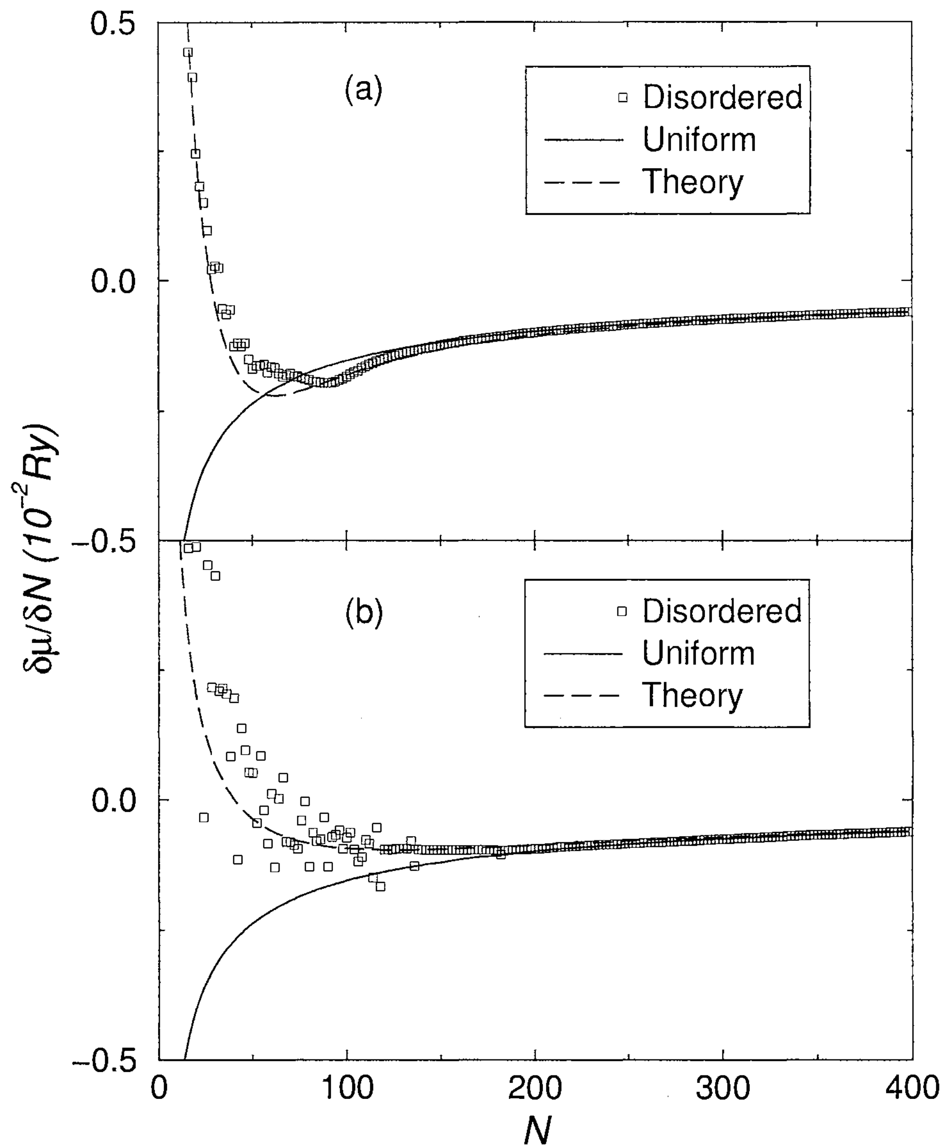

Figure 2.8. $\delta\mu/\delta N$ as a function of the electron density. Solid lines are for the uniform electron gas, squares are the data points for the disordered system, and the dashed-lines are the results from the theory discussed in the text. Two kinds of the disorder are used in the calculation: (a) The off-plane charge impurities. The same parameters as the Fig. 2.6 are used; (b) The correlated disorder potential with $V_s = 0.2Ry^*$, $\xi = 0.2L$. The parameters in the dashed-lines: (a) $n_0 = 0.5 \times 10^{-3}/a_B^{*2}$, $\alpha = 2.3$; (b) $n_0 = 10^{-3}/a_B^{*2}$, $\alpha = 1.5$. N is the total number of the electrons in the simulation box. $N = 60$ corresponds to $r_s = 19$; $N = 100$ corresponds to $r_s = 14$; $N = 200$ corresponds to $r_s = 10$.

$$\approx \varepsilon_0 \left[n_{eff}(N+1)\right](N+1) - \varepsilon_0 \left[n_{eff}(N)\right] N$$
$$= \frac{\delta}{\delta N}\left\{\varepsilon_0 \left[n_{eff}(N)\right] N\right\},$$

where we suppose that the electron energy is determined by the local density of the electrons. $E(N)$ is the total energy of the system, $\varepsilon_0(n)$ is the energy per electron for the uniform electron gas, and n_{eff} is effective local density. For the inhomogeneous system as shown in Fig. 2.6, the effective local density can be estimated by $n_{eff}(n) \approx n/f(n)$, where $f(n)$ is the fraction of the high density region. After some algebra, we have

$$\mu(n) = \mu_0\left(\frac{n}{f}\right)\left[1 - \frac{d\ln f}{d\ln n}\right] + \varepsilon_0\left(\frac{n}{f}\right)\frac{d\ln f}{d\ln n},$$
$$\frac{\delta\mu}{\delta n} = \mu_0'\left(\frac{n}{f}\right)\frac{1}{f}\left[1 - \frac{d\ln f}{d\ln n}\right]^2 - \varepsilon_0'\left(\frac{n}{f}\right)\left(\frac{n}{f}\right)^2\frac{d^2 f}{dn^2},$$

where μ_0 is the chemical potential for a uniform electron gas. In the low density limit, $f(n) \to 0$, the local effective density is greatly different from the average density of the system. As a consequence, the density dependence of the chemical potential, $\delta\mu/\delta n$, changes greatly. In general, supposing $f(n) \sim n^\alpha$ in the low density limit, the analysis shows that $\delta\mu/\delta n$ will have a non-monotonic behavior if $\alpha > 1$. The behavior of $f(n)$ is determined by the local disorder potential profile. In a 2D system, the infinite harmonic potential has $f(n) \sim n$. So the requirement $\alpha > 1$ is equivalent to the condition that the local disorder potential has a weaker confinement effect than the harmonic potential. The condition can be easily satisfied in a typical experimental system. For instance, the Coulomb potential has $f(n) \sim n^4$. In Fig. 2.8, we use the above equation for $\delta\mu/\delta n$ with the following relation of $f(n)$ to fit the data,

$$f(n) = \frac{1}{1 + \left(\frac{n_0}{n}\right)^\alpha}.$$

This form has a correct behavior in the high density limit, $f \to 1$, and the low density behavior is controlled by α. By carefully choosing the values for α and n_0, we obtain a good agreement with our numerical data as shown in the dashed line in Fig. 2.8(a).

To show the effect of the detail potential profile, we plot the compressibility for two kinds of disorder potentials in Fig. 2.8. Indeed, they have different indexes α. The index for off-plane charge impurity is greater than the correlated random potential.

2.2.4 Conclusion

To conclude, we have studied the electron space distribution and the compressibility of disordered dilute 2D electron systems by using the local density approximation. Electron distribution confirms the formation of the droplet state that consists of high and low density regions. Our calculated compressibility is in good agreement with the experimentally observed behavior showing unexpected anomaly at low densities. The turning point of the compressibility happens around the percolation threshold.

CHAPTER 3

Quantum and Semi-Classical Transportation

Within the droplet model, the 2D metal-insulator transition can be considered as the percolation transition of the high density phase. In this chapter, we study the percolative transport in detail.

In the first section, a simple classical percolative resistance network model is used to calculate the temperature dependence of the resistance. At low temperature, the quantum effect becomes important. The semi-classical percolation with the quantum correction is studied in detail in the following sections to understand the low temperature behavior.

3.1 The Classical Model

3.1.1 Model

A straightforward percolative model can be built based on a random resistance network. Fig. 3.1 shows the mapping between an inhomogeneous 2D system and a random resistance network. The system is divided into blocks, and each block maps to a resistance: those high density blocks (black regions) are mapped to liquid phase resistances (black resistances), and those low density blocks (white regions) are mapped to gas phase resistances (unfilled resistances).

The liquid phase is considered as conductive, and its resistance is supposed to be roughly independent of temperature,

$$R_{\text{liquid}} = 1, \tag{3.1}$$

where we set the unit of resistance as the resistance of the liquid phase. For the low density gas phase, the conduction is through the hopping of the localized electrons,

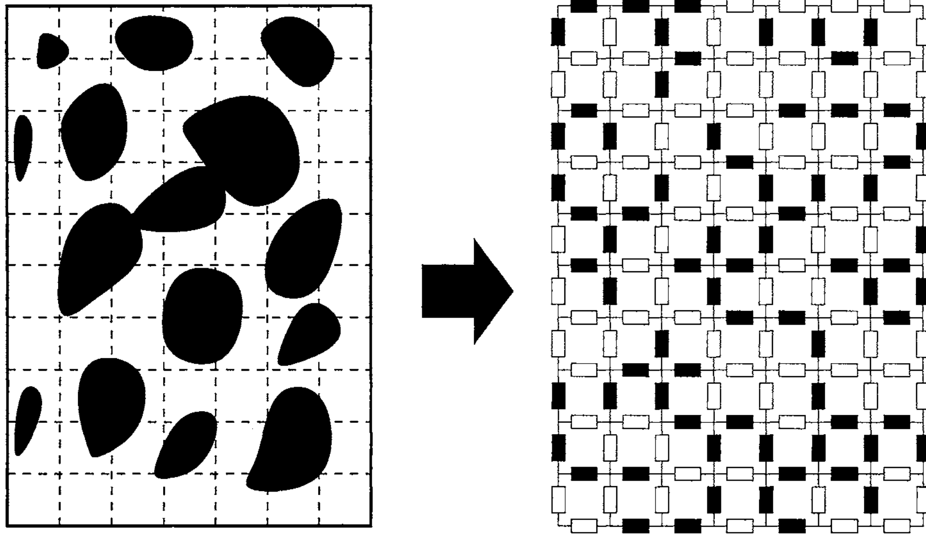

Figure 3.1. Mapping from an inhomogeneous 2D system to a resistance network. Left: black denotes the high density liquid phase, white denotes low density gas phase. The system is divided into blocks. Right: black denotes the resistance of a high density block, white denotes the resistance of a low density block.

for which the temperature dependence of the resistance is of the form,

$$R_{\text{gas}} = \rho_g \exp\left(\sqrt{\frac{T_0}{T}}\right), \tag{3.2}$$

where ρ_g and T_0 are constant parameters.

The proportion of the liquid phase is determined by the electron density. We denote the proportion of the high density liquid phase at the zero temperature as P_0, which is a function of the electron density. At a finite temperature, the high density liquid phase is excited to the gas phase (see Sec. 1.4), the temperature dependence of the proportion of the high density liquid phase is then,

$$P_{\text{liquid}} = P_0(1 - e^{-\Delta_c/T}), \tag{3.3}$$

where Δ_c is the cohesive energy of the liquid phase, which is the energy gap between the liquid phase and the gas phase.

Eq. 3.1-3.3 define a random resistance network as shown in Fig. 3.1. The average conductance of the network could be calculated by using transfer matrix method [65].

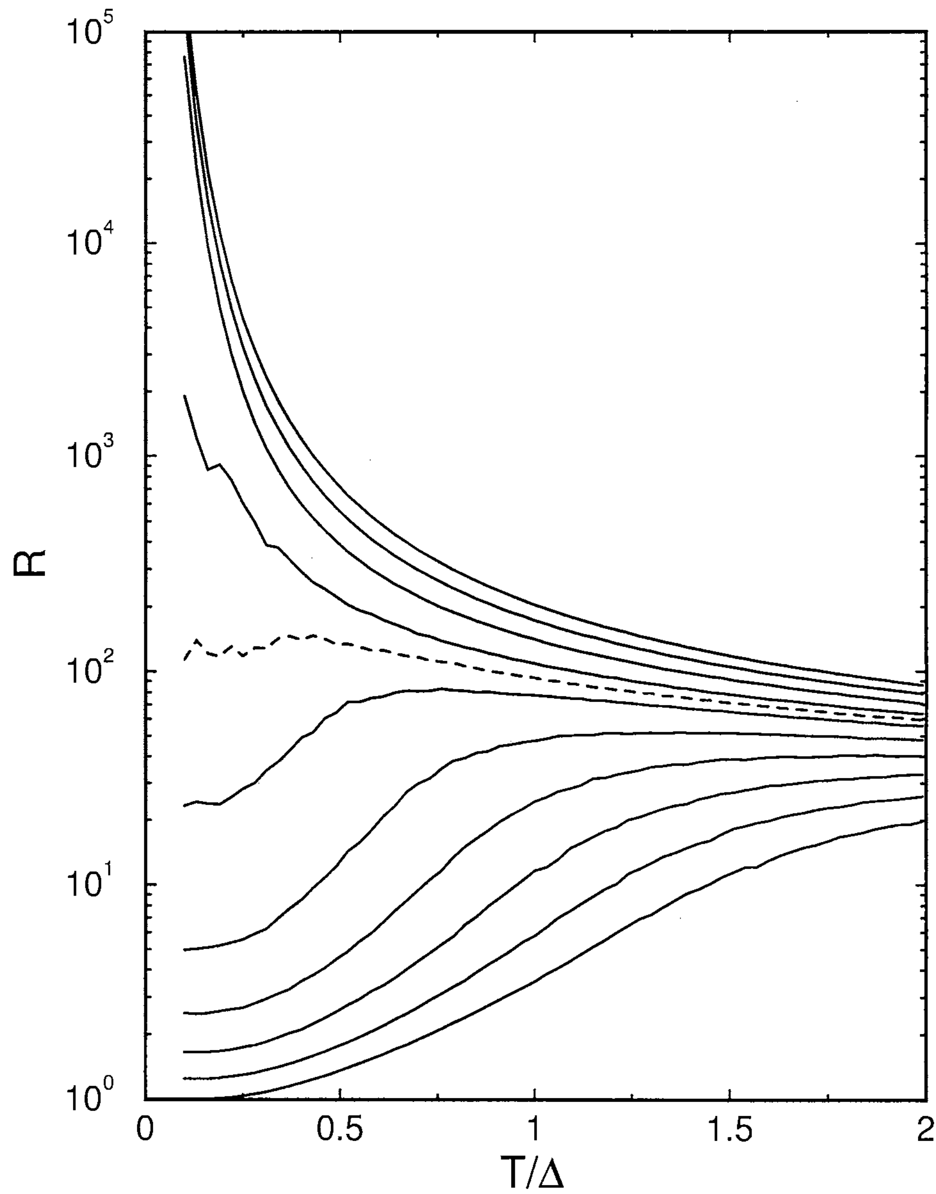

Figure 3.2. The resistance of the model resistance network vs. temperature. The calculation is carried out on a stripe with width 20 and length 20000. For solid lines, P_0 = 0.1, 0.2, 0.3, 0.4, 0.5, 0.6, 0.7, 0.8, 0.9, 1.0. For dashed line, $P_0 = 0.45$. parameters are: $T_G/\Delta = 10$, $\sigma_g = 0.1$.

3.1.2 Results

The calculation result is shown in Fig. 3.2. The great resemblance with the experimental results (see Fig. 1.3 and Sec. 1.2.1) is observable. The most important features of the experimental findings can be reflected in this simple model:

(i) Several orders of drop of the resistance can be found at the low temperature for high densities (large P_0). This is the result of the evaporation of the liquid phase to the gas phase. When $P_0 > P_c$, where $P_c = 0.5$ is the percolation threshold for the network model used here, the conductance of the system can be written as,

$$R(T) = R(P_{\text{liquid}}) \approx R(P_0) + [-R'(P_0)P_0]\, e^{-\Delta_c/T},$$

where we ignore the effect of the resistance of the gas phase, which is much larger than the resistance of the liquid phase at low temperatures.

(ii) There exists a curve that is almost independent of temperature, as shown as dashed line in Fig. 3.2. The curve has $P_0 = 0.45$, which is a little bit lower than the percolation threshold of the corresponding percolation network at $P_c = 0.5$.

(iii) When $P_0 \ll P_c$, the system enters into the insulating regime. The conductance of the system is determined by the resistance of the gas phase, as shown in Eq. 3.2.

(iv) The re-entry of insulating state at the high temperature observed in the experiments is also present in this simple models. For $P_0 \gtrsim P_c$, the proportion of the liquid decreases with temperature, and there exists a temperature T_1, when $T > T_1$, $P_{\text{liquid}}(T) < P_c$. So the system re-enters the insulating phase at high temperature.

3.1.3 Conclusion

The experimental findings can be well reflected by a simple model with few parameters based on the classical percolation model. The most striking features of the metal-insulator transition, *i. e.*, the resistivity drops several orders at low temperatures, can be easily explained in the percolation picture.

However, the model is purely classical, with no quantum effect present. As the temperature getting lower, the quantum effects become more and more important.

Moreover, according to the scaling theory of localization, there will be no percolation transition in a 2D quantum percolation network. On the other hand, for a real system, there always exists a finite dephasing effect, which is caused by the electron-electron scattering and electron-phonon scattering at finite temperatures. The behavior of such systems, where the quantum effects compete with the classical effects, is interested.

3.2 Quantum Effects: One-Dimensional System

In the classical calculation as shown in last section, the system is supposed to consist of inhomogeneous density distribution with high density conducting regions and low density insulating regions, and the resistance of system can be simulated by a simple random resistance network. This calculation is only valid when the electron phase is totally incoherent in each separate region. The dephasing of electrons is essential for the model since a pure quantum system will never percolate according to the well-known scaling theory of localization [1].

It is not obvious that a system can be considered as a classical system at low temperatures. A recent experiment [66] on 2D systems shows that the phase coherence length is quite long, typically 600-1000 nm. Thus, it is more likely that a real system is in the regime where quantum effects compete with classical effects. Classical effects are manifested by a finite phase coherence length, which may be due to a finite temperature or other novel mechanisms. For instance, there are experiments indicating that the dephasing rate may be finite even at zero temperature [67,68]. On the other hand, in a disordered 2D system, the quantum effect always causes the localization length to be finite. For a 2D system with metal-insulator transition, the localization length strongly depends on the electron density. Actually, by changing electron density, the conductance of the system may change several orders of magnitude, indicating the localization length may strongly depend on the electron density. The behavior of the system is determined by two competing length scales: localization length and phase coherence length. Therefore, it is important to study the system

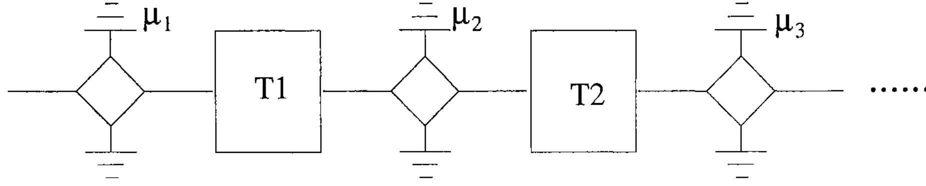

Figure 3.3. The model to simulate the system with dephasing and disorder. The rectangles represent the normal random scatters, and the diamonds represent the dephasing scatters.

with any given strength of disorder and dephasing, and determine the effect of the finite localization length and phase coherence length.

In this section, we study the interplay of disorder and dephasing of one-dimensional (1D) systems in transport properties. We limit ourselves to 1D models to reduce the severe finite-size effect in numerical results for higher dimensions, although our conclusion can be carried over to higher dimensions.

3.2.1 Model

Our 1D model (Fig. 3.3) consists of normal random scatters and dephasing scatters, alternatively. While the normal random scatters give rise to a finite localization length, the dephasing scatters randomize electron phase. The normal random scatters are constructed by M δ-barriers with random height q_i, which has the distribution

$$P(q_i) = \begin{cases} \frac{1}{\Delta q}, & \text{if } -\frac{\Delta q}{2} \leq q_i \leq \frac{\Delta q}{2} \\ 0, & \text{otherwise} \end{cases} .$$

In the model Δq controls the randomness of the system. The transmission and reflection coefficients for the normal random scatters can be calculated from the transfer-matrix for individual δ-barrier [69],

$$U_i = \begin{bmatrix} \frac{1}{t^*} & \frac{r}{t} \\ \frac{r^*}{t^*} & \frac{1}{t} \end{bmatrix} = \begin{bmatrix} 1 - i\frac{q_i}{2k} & -i\frac{q_i}{2k} \\ i\frac{q_i}{2k} & 1 + i\frac{q_i}{2k} \end{bmatrix},$$

where t and r are the transmission and reflection amplitudes for the barrier, and k is the momentum of the injected electron. The transfer matrix for M sequential δ-barriers can be calculated from

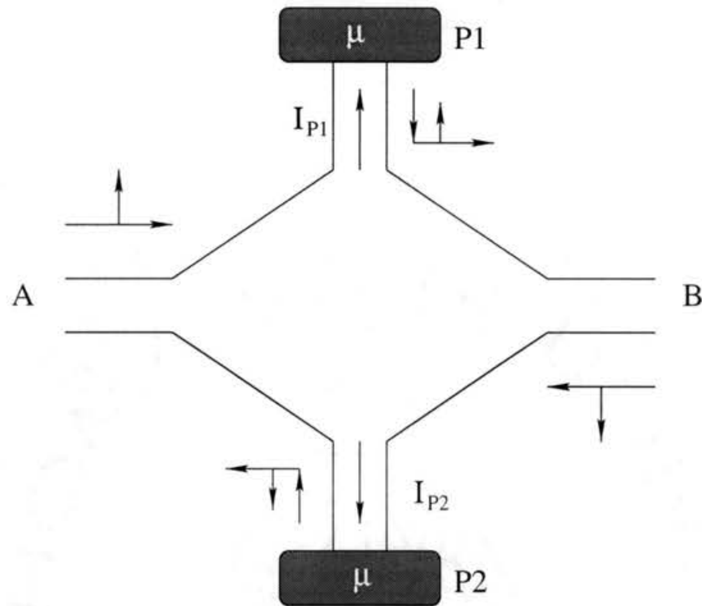

Figure 3.4. The structure of an individual dephasing scatter. The system is connected to two identical external electron reservoirs P1 and P2. An electron can be scattered along the directions shown by the arrows. There is no backscattering caused by this dephasing scatter.

$$U^M = U_M X U_{M-1} X \cdots U_1 X,$$

where X is the transfer matrix describing the propagation of the electron from one δ-barrier to the next. Assuming the spacing between the neighboring barriers is unity, X is

$$X = \begin{bmatrix} e^{ik} & 0 \\ 0 & e^{-ik} \end{bmatrix}.$$

Using the transfer-matrix technique, the localization length can be determined analytically [69].

To introduce the dephasing effect into the system, one has to include the interaction between the system and the environment. The Büttiker model [70,71] shown in Fig. 3.4 is the simplest way to achieve that. In this approach, the system is connected to the external electron reservoirs via the dephasing scatters. With a certain possibility, an electron is scattered into the external reservoirs, totally losing its phase memory, and then re-injected into the system. Two restrictions are imposed to reflect

physical reality. First, the net current between the system and the reservoirs should be zero so that each scattered electron will finally return to the system. To do so, one can adjust the chemical potential μ of the external reservoirs such that $I_{P1}+I_{P2}=0$, where $I_{P1}(I_{P2})$ is the current between the system and the external reservoir P1 (P2). Second, the system is connected to two identical electron reservoirs P1 and P2, and the S-matrix between the system and the reservoirs is designed so that the electron is only scattered forward, thus the dephasing scatters will not cause any momentum relaxation. The S-matrix reads [71]

$$S = \begin{array}{c} A \\ B \\ P1 \\ P2 \end{array} \begin{bmatrix} 0 & \sqrt{1-\alpha} & 0 & -\sqrt{\alpha} \\ \sqrt{1-\alpha} & 0 & -\sqrt{\alpha} & 0 \\ \sqrt{\alpha} & 0 & \sqrt{1-\alpha} & 0 \\ 0 & \sqrt{\alpha} & 0 & \sqrt{1-\alpha} \end{bmatrix},$$

where α is the possibility that the electron is scattered to the reservoirs, namely, the dephasing rate. The phase coherence length is estimated by $L_\varphi \simeq M/\alpha$.

The localization length of the system is determined by the normal random scatters, while the phase coherence length is determined by the dephasing scatters. For a system with N dephasing scatters, there are $N+2$ external chemical potentials μ_i with $i = L,\ R,\ 1,\ 2,\ \cdots N$, where $\mu_{L(R)}$ is the chemical potential for the left (right) measurement electrode. The system satisfies the multi-lead Ohm's law,

$$I_i = \sum_j \sigma_{ij}\mu_j, \quad i,\ j = L,\ R,\ 1,\ 2,\ \cdots N.$$

The conductance between the leads, σ_{ij}, is determined by the Landaur-Büttiker formula,

$$\sigma_{ij} = \frac{2e^2}{h} T_{ij} \quad \text{for}\, i \neq j,$$

where T_{ij} is the transmission coefficient between the leads. For the leads attached to the dephasing scatters, the transmission coefficient is the sum of all transmission coefficients between leads P1 and P2,

$$\begin{aligned} T_{ij} &= T_{i\,P1,j\,P1} + T_{i\,P1,j\,P2} + T_{i\,P2,j\,P1} + T_{i\,P2,j\,P2}, \\ &\quad \text{for}\, i,j = 1,\ 2,\ \cdots N. \end{aligned}$$

The gauge invariance, namely shifting each μ_i by a constant should not affect the result, is satisfied through the condition

$$\sigma_{ii} = -\sum_{j\neq i} \sigma_{ij}.$$

The total conductance of the system is calculated by imposing the condition

$$I_i = 0 \quad \text{for}\, i = 1,\, 2,\, \cdots N.$$

After some algebra, the total conductance of the system can be written as

$$\sigma_{tot} = \sigma_{LR} - \begin{bmatrix} \sigma_{L1} & \cdots & \sigma_{LN} \end{bmatrix} \begin{bmatrix} \sigma_{11} & \cdots & \sigma_{1N} \\ \vdots & \ddots & \vdots \\ \sigma_{N1} & \cdots & \sigma_{NN} \end{bmatrix}^{-1} \begin{bmatrix} \sigma_{1R} \\ \vdots \\ \sigma_{NR} \end{bmatrix}.$$

Although we start from a seemly artificial model, the total conductance formula actually reflects physical reality. It contains two kinds of contributions: the first is the direct conductance σ_{LR} coming from direct quantum tunneling; the second is the correction due to the dephasing effect caused by classical sequential tunneling. Thus, the conductance formula is consistent with the general picture of the dephasing effect on a conductance.

3.2.2 Conductance

The typical behavior of the conductance for the system is shown in Fig. 3.5, where we plot the conductance as a function of the dephasing rate α. In a real system, the dephasing rate is a monotonic function of temperature, so the plot can also be considered as the temperature dependence of the conductance. We have systematically calculated the conductance for different sets of parameters, and the results show qualitatively similar behavior, although the peak position depends on the parameters. The most important feature of the plot is that the conductance is not a monotonic function of the dephasing rate, or temperature. The plot can be divided into two regions, the gray and white regions. In the gray region, the dephasing rate is low and the phase coherence length is long. The electron is localized within the

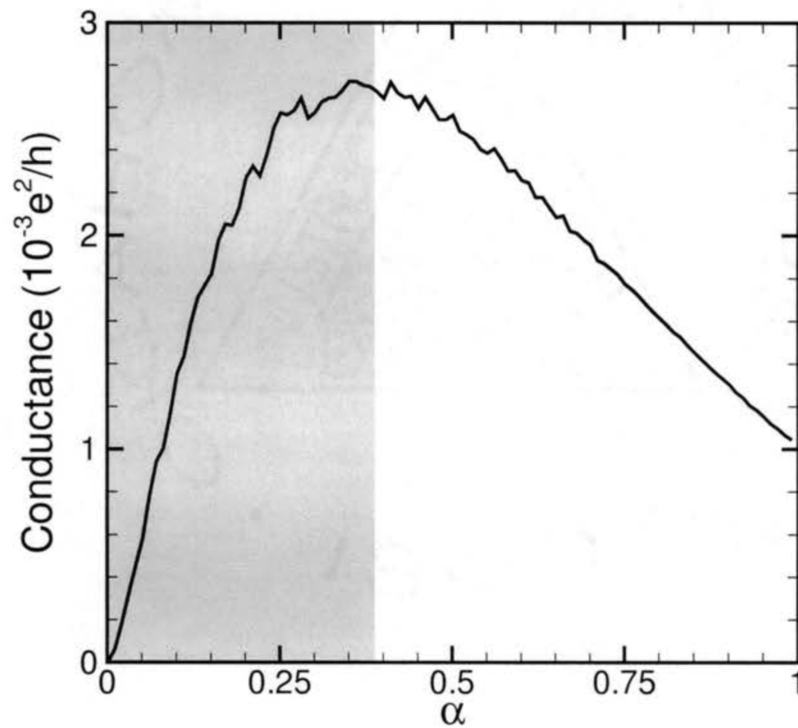

Figure 3.5. The typical behavior of the conductance. We use the parameters $Q_0 = \overline{q/2k} = 1.1$, $\Delta q = 0.5$, $M = 5$, $N = 100$, and average over 500 samples. The gray and white regions show the quantum and classical regime respectively.

phase coherence length, so the system shows quantum localization with insulator-like behavior, namely, the conductance decreases as temperature drops. This region can be considered as the quantum region. On the other hand, when the dephasing rate becomes higher, the system enters into the classical regime and the conductance increases with decreasing temperature, a typical metallic behavior.

The turning point between the quantum and classical regimes can be determined by comparing the phase coherence length L_φ with the localization length ξ calculated from the transfer matrix formalism [69]. The result is shown in Fig. 3.6. It turns out that the transition occurs at the point where $L_\varphi \sim \xi$. From Fig. 3.6 and Fig. 3.6, one can clearly see that by changing the phase coherence length or the localization length, it is possible to observe the transition from the metal-like behavior to the insulator-like behavior, and the behavior of the system is determined by the competition between the localization length and the phase coherence length. Therefore, it is the transition between the quantum and the classical phases.

3.2.3 Connection With Experiments

Great resemblance could be found when comparing the experimental observation to the result from this simplified model. In Fig. 3.7 we plot the dephasing rate (or temperature) dependence of the resistance. Different curves are for different scattering parameter $Q = q/2k$. Changing the carrier density is equivalent to changing the Fermi momentum, which in turn changes Q. Thus, different curves correspond to different carrier densities. In the plot, we impose a finite cutoff of the dephasing rate α, which makes lower α inaccessible (gray region in the plot). For α above the cutoff, the phase coherence length L_ϕ is always finite. Depending on whether L_ϕ is larger or smaller than the localization length ξ, one can either observe the metal-like or the insulator-like behavior, as shown in Fig. 3.7. When the finite cutoff falls upon the turning point (the maximum conductance point in Fig. 3.5), the system shows the "critical" behavior, where the resistance is nearly flat within a certain temperature range. In Fig. 3.8, we show the density dependence of the conductance for different

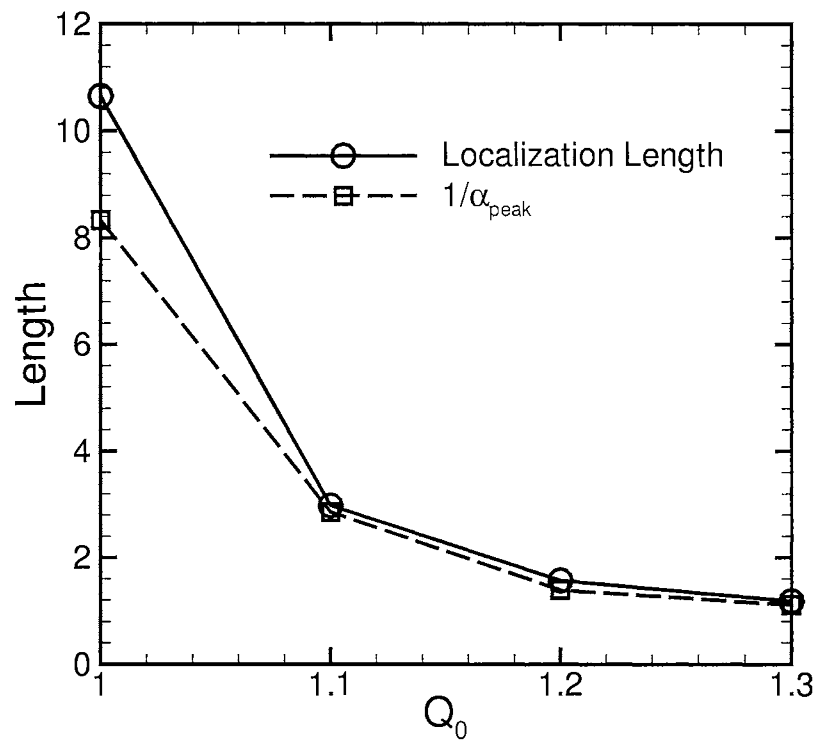

Figure 3.6. The comparison between the localization length and the $1/\alpha_{peak}$, which is equivalent to the phase coherence length. $Q_0 = \overline{q_i/2k}$, and $\Delta q = 0.5$.

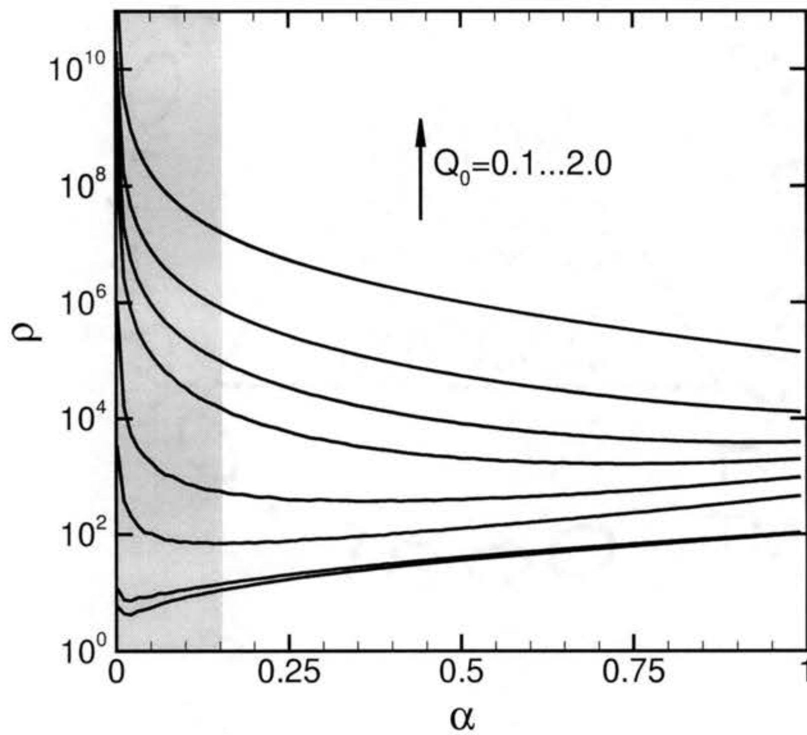

Figure 3.7. The dephasing rate (or temperature) dependence of the resistance for different carrier densities ($Q_0 = \overline{q_i/2k}$). The gray region shows inaccessible region due to the finite cutoff of the dephasing rate. We use $\Delta q = 0.5$, and Q_0 =0.1, 0.5, 1.0, 1.1, 1.2, 1.3, 1.5, 2.0.

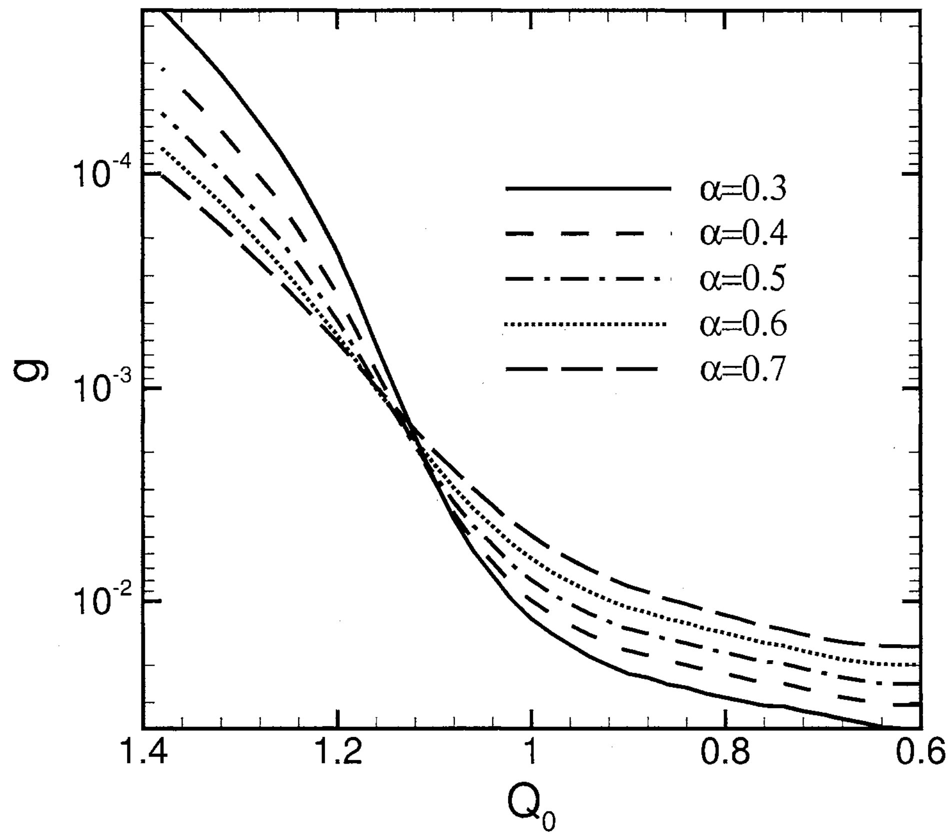

Figure 3.8. The density dependence of the conductance for different temperatures. We reverse the direction of the axes so that it is easier to compare with $n-\rho$ plot wildly used in the literatures.

α (or temperature). One can identify a "fixed" point where different curves cross at. Similar feature has been seen in many experimental plots.

3.2.4 Discussion

The finite cutoff of the dephasing rate can be justified by two possible reasons. First, the cutoff may be due to a finite temperature. In this case, if we assume the dephasing rate goes to zero when temperature approaches zero, as suggested by a simple power law $\alpha \sim T^{\nu}$, there is always an upturn of the resistance at low enough temperature as shown in Fig. 3.7 for low values of α. This suggests a re-entrance to an insulator at low temperatures. The re-entry behavior may have already been observed in the recent experiment [41]. Under the circumstance, the transition is a finite temperature effect. The second possibility is that the dephasing rate might be finite at zero temperature [67,68]. Consequently, the metallic phase will survive even at zero temperature. If we adhere to the original definition that a metal has a finite resistance at zero temperature while the resistance of an insulator diverges, the system will always be a metal. The reason is that on the low density "insulator" side, the resistance will saturate to a finite value at $T = 0$ because of the finite phase coherence length. However, in a similar plot as shown in Fig. 3.8, a "fixed" point can still be identified which can be used as an operational definition of "metal-insulator transition".

The saturation of the dephasing rate at low temperatures is still a controversial issue. Some argue that the saturation observed in the experiments is not an intrinsic effect. Nevertheless, whether it is intrinsic or extrinsic, the same factors which cause the saturation should have a similar effect on the conductance. To justify a real metal-insulator transition, one has to clearly rule out those external factors that may cause finite dephasing rate at low temperature [67,68].

In our simplified model, the detail structure of 2D electron gas is omitted. However, the same mechanism should be essential for the system at low temperature, while the percolation mechanism dominates in higher temperature, where the quantum effect is not important.

In summary, we have studied the interplay between dephasing and disorder. Based on a 1D model, we show that by changing the phase coherence length or the localization length, it is possible to observe the transition from the insulator-like behavior to the metal-like behavior, which corresponds to a transition between quantum and classical phases. The resemblance between this simplified model and the experiments suggests that the quantum effect is important at low temperature, although the high temperature behavior is dominated by the classical effect. We suggest that conductance experiment should be accompanied by a dephasing rate measurement to address the effect of a finite coherence length. Although our calculation is for a 1D model, the same physics should survive at higher dimensions.

3.3 Semi-classical Percolation In 2D Systems

In this section, we extend the calculation to a 2D quantum percolation model [72–75] with a finite phase coherence length. The dephasing mechanism is introduced by attaching current-conserving voltage leads to the system, a method widely used for one-dimensional models in mesoscopic community [70,71]. The system is no longer a Hamiltonian system since the voltage values at voltage leads are allowed to vary in order for the current conservation to be satisfied. The conductance in such a system is calculated. The transition point defined by the operational definition $d\rho/dT = 0$ is identified. The scaling property close to the crossing point is also studied, and the results are in agreement with the experimental findings.

3.3.1 Model

Our quantum percolation model is based on a tight binding Hamiltonian of a 2D square lattice,

$$H = \sum_i \epsilon_i c_i^\dagger c_i + \sum_{<i,j>} t_{ij}(c_i^\dagger c_j + c_j^\dagger c_i), \tag{3.4}$$

where $< ij >$ denotes a pair of nearest-neighbor sites and ϵ_i is the on-site energy. We choose ϵ_i to be random, ranging from $-W/2$ to $W/2$ to model an on-site disorder. The nearest-neighbor hopping matrix elements t_{ij} is a random variable which assumes the

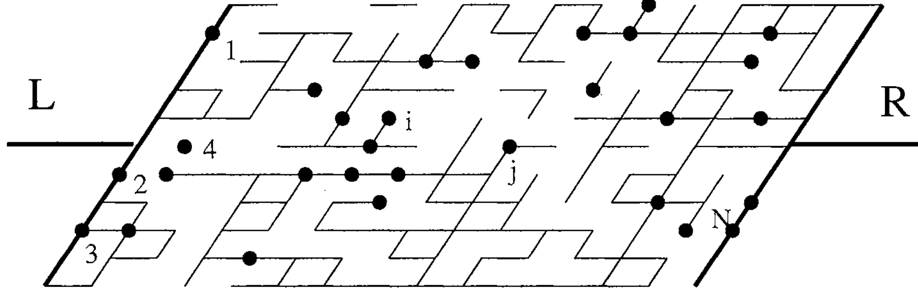

Figure 3.9. Lattice system of our study. • denotes a lattice site where a phase-breaking voltage lead is attached.

values 1 (connected bonds in Fig. 3.9) or 0 (empty bonds in Fig. 3.9) with respective probabilities P and $1-P$. In order to introduce phase-breaking mechanism, we attach current-conserving voltage leads [70,71] at random lattice sites (• sites in Fig. 3.9). The probability where a lattice site is attached with a voltage lead is denoted P_v and the hopping element between a voltage lead and a lattice site is denoted t_v. The sole role of the voltage leads is to randomize the phases of incoming and outgoing wave-functions at the lead sites while maintain current conservation. Using Keldysh Green's function formalism [71,76], it is straightforward to derive the multi-lead current-voltage relation:

$$I_i = \sum_{i=1}^{N} \sigma_{ij} V_j \quad i,\, j = L,\, R,\, 1,\, 2,\, \cdots N, \tag{3.5}$$

where

$$\sigma_{ij} = \frac{8e^2}{\hbar} \mathrm{Tr} \left[(T_{j\alpha} G^r_{\alpha\alpha} T_{\alpha i}) \rho_i (T_{i\alpha} G^a_{\alpha\alpha} T_{\alpha j}) \rho_j \right] \quad i \neq j \tag{3.6}$$

and

$$\sigma_{ii} = -\sum_{j \neq i} \sigma_{ij} \tag{3.7}$$

In the above equations, α denotes the vector space of the lattice system, $T_{\alpha i}$ is the transmission matrix, $G^{r(a)}_{\alpha\alpha}$ is the retarded (advanced) Green's function of the lattice system, and $\rho_i = \mathrm{Im} g^a_i$ are the density of states matrices for the voltage leads and measurement leads L and R, with g^a_i being the advanced Green's function at ith lead. In order to satisfy current conservation, we require that the total current through each

voltage lead to be zero, namely, $I_i = 0$ when $i \neq L, R$. This restriction fixes the values for V_i. Under these conditions, we obtain the conductance between L and R

$$g = \sigma^d_{LR} + \sigma^i_{LR}. \tag{3.8}$$

Here σ^d_{LR} is the direct conductance which can be obtained from Eq.(3) with $i = L$ and $j = R$, and σ^i_{LR} is the indirect conductance,

$$\sigma^i_{LR} = -\begin{bmatrix} \sigma_{L1} & \cdots & \sigma_{LN} \end{bmatrix} \begin{bmatrix} \sigma_{11} & \cdots & \sigma_{1N} \\ \vdots & \ddots & \vdots \\ \sigma_{N1} & \cdots & \sigma_{NN} \end{bmatrix}^{-1} \begin{bmatrix} \sigma_{1R} \\ \vdots \\ \sigma_{NR} \end{bmatrix}. \tag{3.9}$$

The σ^i_{LR} is the conductance of the conductance network obtained from the quantum lattice model. The direct conductance σ^d_{LR} represents the direct quantum hopping between the measurement electrodes, and the indirect conductance σ^i_{LR} includes the contributions from the sequential hopping.

3.3.2 Conductance

We have calculated the total conductance g numerically. In the following we present the results and discuss their implications. There are several parameters in our model as mentioned before: P (probability for $t_{ij} = 1$), P_v (probability for a voltage lead), t_v (hopping between a voltage lead and the lattice system), W (on-site disorder), and E (electron energy). The results presented below are for $t_v = 0.1$, $W = 2$ and $E = 0$. We have done systematic studies by varying these three parameters, including zero on-site disorder with $W = 0$, and we found that the qualitative results remained unchanged. In Fig. 3.10(a) we show g as a function of P for a pure quantum case with $P_v = 0$. The calculation is done on an $L \times L$ square lattice. The different curves are for different L's with $L = 10$ (solid line), $L = 20$ (dashed line) and $L = 30$ (long-dashed line). The important message from this plot is that for a given P, g decreases with increasing system size L, indicating an insulating behavior. This result is consistent with the conclusion of scaling theory of localization, namely, in a disordered quantum system, all states are localized.

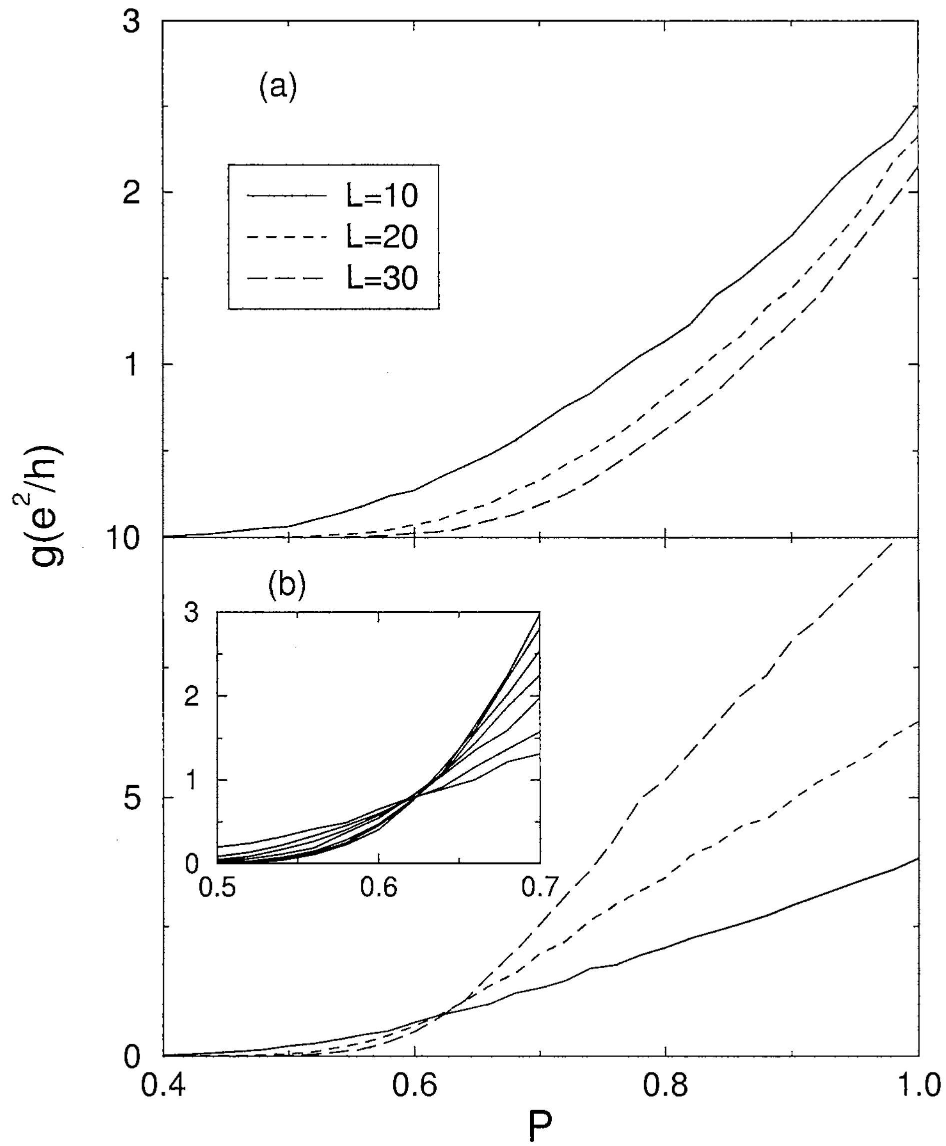

Figure 3.10. (a) Conductance g as a function of the probability P for a pure quantum system with size $L = 10$, 20 and 30. (b) Same as (a), except with $P_v = 0.2$. Inset: Plot g vs. P at the vicinity of P_c for $L = 10$, 15, 20, 25, 30, 35 and 40.

In Fig. 3.10(b) we plot the same curves as in Fig. 3.10(a), except with $P_v = 0.2$, *i.e.*, 20% of lattice sites are attached with phase-breaking voltage leads. The striking difference between the two plots is that in Fig. 3.10(b), all curves cross at a single point $P_c \simeq 0.62$. For $P > P_c$, g increases with L, while it decreases with L for $P < P_c$. We can connect the numerical results with the experimental observations, *i. e.*, changing the carrier density is equivalent to changing P, and changing temperature is equivalent to changing the system size L [77]. Thus Fig. 3.10 can be considered as the density dependence of the conductance for different temperatures. A similar crossing point has been observed in many experiments and the crossing point is identified as the metal-insulator transition point using the operational definition $d\rho/dT = 0$. Moreover, We find that the conductance at the "transition point" P_c is of the order $2e^2/h$, and weakly depends on the strength of disorder. The similar behavior is also observed in the experiments.

3.3.3 Scaling Properties

In Fig. 3.11 we show the scaling properties of our data. We use the standard finite-size scaling analysis [78]. The conductance curves for system sizes L and different P's can be scaled to the metallic and insulating branches. Those curves with $P > P_c$ ($P_c = 0.62$) on the metallic side are scaled along the L-axis so that they coincide with a particular curve chosen here for $P = 0.70$. $\xi(P)$ is determined from curve shifting. The similar procedure is also applied to insulating side, in which case we scaled the curves to coincide with the curve for $P = 0.54$. We find that all the conductance g for different size L (ranging from 10 to 45) can be collapsed in a two-branch scaling function, $g(L) = f(L/\xi(P))$, where $\xi(P)$ diverges at P_c. Fig. 3.11(a) shows the scaling function and $\xi(P)$ is shown in the inset. We find that $\xi = |P - P_c|^{-\nu}$ with $\nu = 1.4 \pm 0.2$, which coincides with the experiments.

Another important scaling property is the β function, defined as

$$\beta(g) = \frac{\partial \log g}{\partial \log L}. \tag{3.10}$$

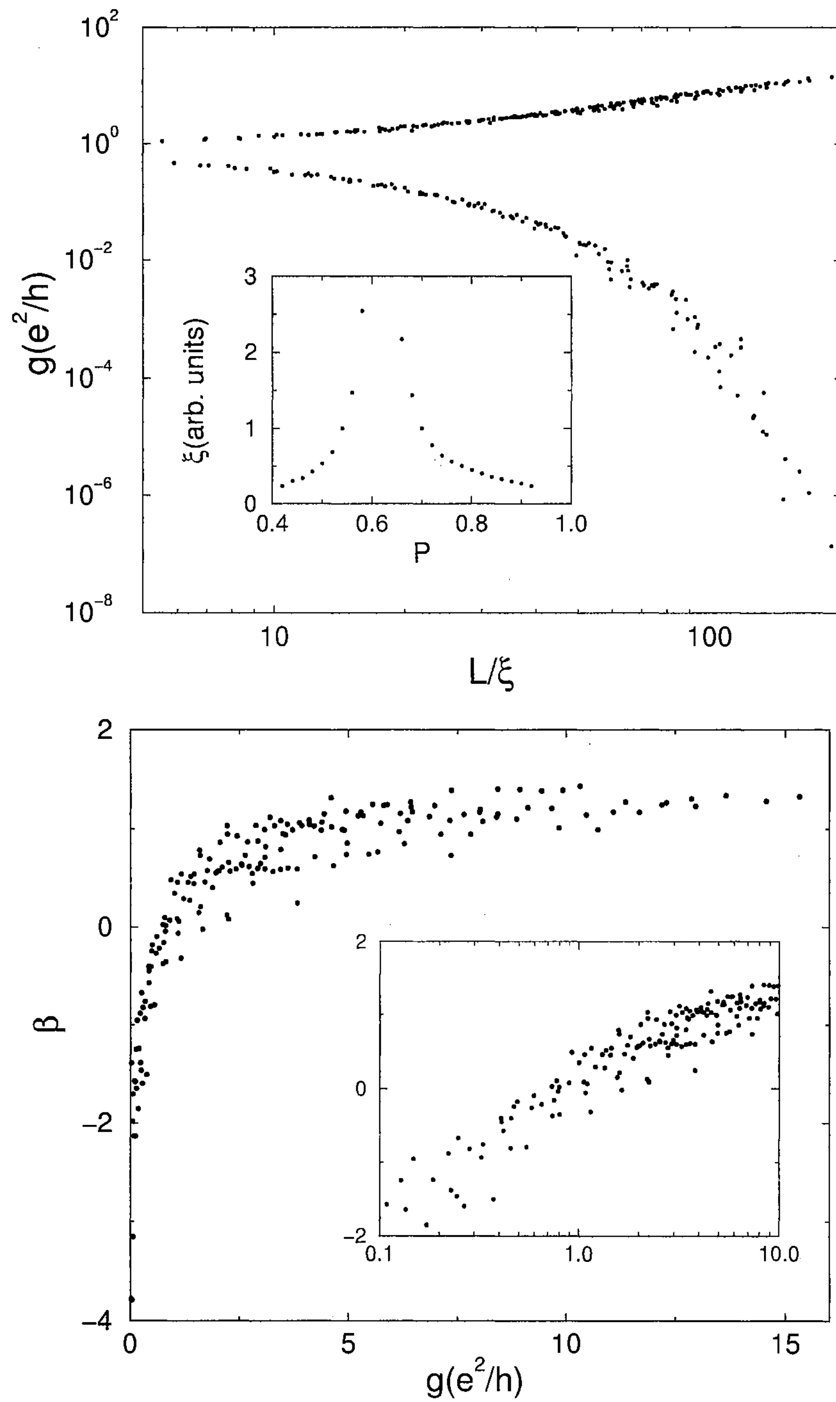

Figure 3.11. (a) Scaling plot of g vs. L/ξ for L = 10, 12, 15, 18, 20, 20, 25, 28, 30, 32, 35, 38, 40 and 45. Inset: ξ vs. the probability P. (b) Plot β function vs. g. Inset: β vs. $\log g$ near $\beta = 0$.

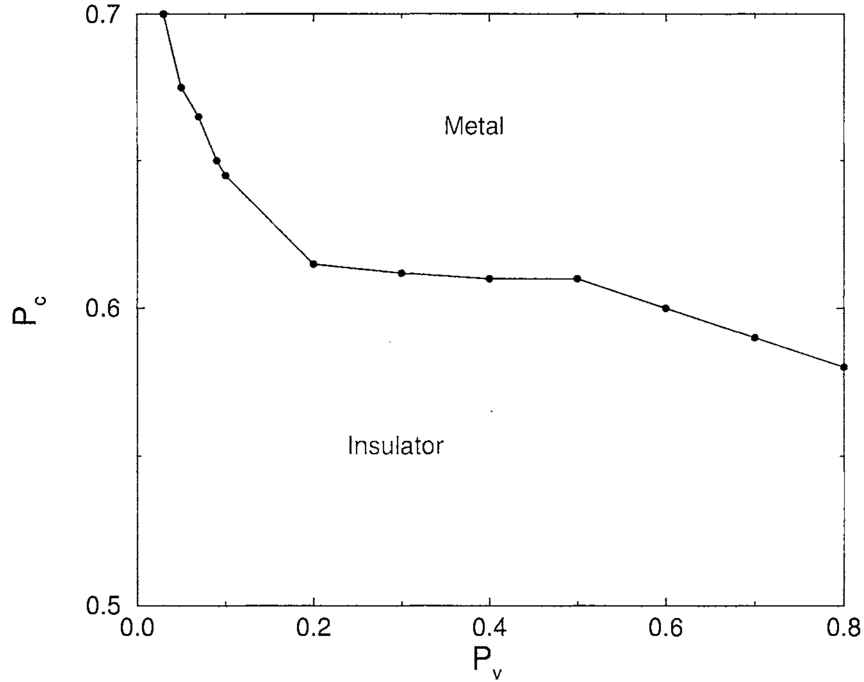

Figure 3.12. P_v versus P_c.

Fig. 3.11(b) shows $\beta(g)$. β is negative for small g and approaches a positive value for large g. In the inset, β is plotted as a function of $\log g$ and we find that $\beta \propto \log(g/g_c)$ around $\beta \simeq 0$, in common with other kinds of metal-insulator transition [79].

In our model, the phase coherence length L_ϕ is controlled by the probability of voltage leads P_v and the hopping between the a voltage lead and lattice system t_v. Although it is difficult to determine the explicit relation between L_ϕ and P_v and t_v, it is evident that for a fixed t_v, L_ϕ decreases with increasing P_v and approaches infinity (pure quantum system) at $P_v = 0$. We have carried out calculations for several values of P_v for a fixed $t_v = 0.1$ to determine the metal-insulator transition points. Fig. 3.12 presents the resulting transition points P_c versus P_v.

3.3.4 Remarks

We would like to make a few comments.

i. It is clear from the above calculation that the crossing point results from a finite phase coherence length. It is widely believed that the phase coherence length goes to

infinity when the temperature approaches zero. If this is the case, the crossing point will disappear at zero temperature, and there will be no "metal-insulator transition "even by the operational definition $d\rho/dT = 0$. However, there are recent experiments which suggest that the phase coherence length might be finite even as $T \rightarrow 0$ [67,68].
ii. The operational definition $d\rho/dT$ is widely used in experiments to determine the critical point of a metal-insulator transition. But according to the original definition of metal-insulator transition, the transition occurs at the point where zero temperature resistance becomes infinity. If we started from the original definition, the crossing point of our numerical result is clearly not a metal-insulator transition point.

In summary, we have demonstrated that it is possible to understand the metal-insulator transition by the quantum percolation model with a finite phase coherence length. Our calculation shows a crossing point, similar as seen in the experiments. The scaling property around this crossing point is also investigated and the results are consistent with the experimental findings. These results strongly suggest that the "metal-insulator transition "observed in the experiments is percolation in nature and a finite phase coherence length plays an important role in the transition.

CHAPTER 4

In-Plane Magnetic Field Effects And Spin Polaron

In this chapter, the effects of the in-plane magnetic field will be studied. We focus on those systems at the clean limit, such as p-GaAs/AlGaAs heterostructures. In this case, the droplet state proposed in the earlier chapters may be not applicable, since the disorder strength is not strong enough to overcome the Coulomb energy caused by the density redistribution. Some recent experiments about the effect of the in-plane magnetic field [80,81] reveals new details for the properties of the systems, which provide a basis to carry out detailed theoretical studies of the effects of an in-plane magnetic field.

We believe that the percolation model is still valid for these systems. However, the corresponding electron states for the high conducting phase and the low conducting phase are not corresponded to the high density and low density regions. We propose that the high conducting phase is the normal unpolarized Fermi liquid, while the low conducting phase is spin polarized. We will show that with few reasonable assumptions, the effect of the in-plane magnetic field and the metallic temperature dependence can be understood in a unified picture. The theory is valid in clean systems with less disorder effect. For those systems with strong disorder effect, such as Si MOSFETs, the droplet state is still a favorable model.

4.1 Analysis

We start from the ground state of a dilute 2D electron (hole) system on the metallic side. The experiments reveal many Fermi-liquid like behaviors in the 2D metal-insulator transition systems. For instance, it is found that the weak localization effect is present at low temperatures [41,43], which is directly contradictory to

the theoretical proposal of the superconducting ground state [48]. The other proposed ground states, such as Luttinger liquid state [45,46], get little support from the experiments. Thus we assume that the ground state of the dilute 2D electron (hole) system is still a Fermi-liquid.

To study the transport behavior of the homogeneous 2D system, it requires the knowledge of the excitation states. Unfortunately, the theoretical method is yet to be developed to deal with the excitation of strongly correlated systems. On the other hand, the experiments provide some hints concerning the properties of excited states. It is known that the temperature dependence on the resistivity at the metallic side follows [10],

$$\rho(T) = \rho_0 + \rho_1 \exp(-\Delta/T). \tag{4.1}$$

The exponential term indicates an energy gap Δ between the ground state and the excited states.

The recent experiments [80,81] on the resistivity response to the in-plane magnetic field provides more informations on the excited states. These experiments reveal that a strong magnetic field destroys the metallic phase. There exists a critical magnetic field B_c, beyond which the system enters into the insulating state. The critical magnetic field B_c is found to be connected with the energy gap Δ [80]:

$$\Delta \sim g\mu_B B_c.$$

In other words, the energy gap between the ground state and the excited states is the same as the energy to polarize the spins. If the ground state is the unpolarized Fermi liquid, the excitation states should be related to the spin polarized states. On the other hand, the in-plane magnetic field actually drives the system into the insulating state, indicating the insulating state is spin polarized.

Quantum Monte Carlo (QMC) calculations [82] provide favorable evidence to the conclusion. The QMC calculations indicate that there exists a spin unpolarized-polarized phase transition in 2D electron systems before the transition to the Wigner crystal phase. Although the QMC results provide no information about the excited states, we will show that some knowledge can be inferred from the QMC results.

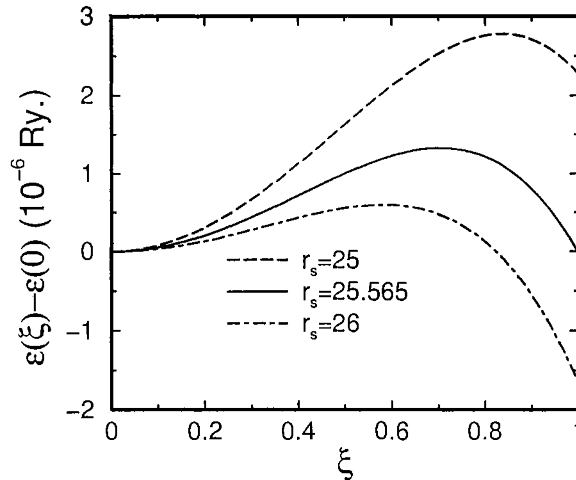

Figure 4.1. The ground state energy per particle depending on the spin polarization ξ near the transition point. From top to bottom, the densities are $r_s = 25$, $r_s = 25.565$, $r_s = 26$. The transition density is at $r_s = 25.565$. $\xi = (n_\uparrow - n_\downarrow)/n$. The figure is based on the QMC results by Attaccalit *et.al.* [82]. The ground state energy does not depend on the sign of ξ.

Besides other possibilities, two kinds of the excitations are interesting to consider. First is the density wave. The density wave causes the density redistribution, and form the spatial inhomogeneous structure. To get the excitation gap, it requires a large density redistribution. For instance, the density of some regions after the excitation becomes so low that the Wigner crystal forms in these regions. However, our earlier calculations (see Chapter II) based on the QMC results show that the redistribution of the density causes excessive Coulomb energy. Without the help of disorder, this kind of excitation is actually prohibited.

Another possibility is the spin wave excitations. As in the case of the density wave, the spin wave causes the spatial inhomogeneous structure in the sense of the spin density distribution. On the other hand, the large spin redistribution does not induce extra Coulomb energy. For a system with relatively low disorder, such as p-GaAs/AlGaAs heterostructures, the excitation is much more favorable.

The QMC results provide some hints about the spin wave excitation. Figure. 4.1 shows the spin polarization dependence of the ground state energy per particle near the transition point. It can be seen that there are three minimal points at $\xi = 0$ and

$\xi = \pm 1$. Above the transition density, $\xi = 0$ is the absolute minimal point, while $\xi = \pm 1$ are the local minimal points. At a finite temperature, it is energetically favorable to excite some regions of the uniform spin unpolarized ground state ($\xi = 0$) into fully polarized state, instead of the partially polarized states. We call this kind of excitation as the spin polaron excitation. The same conclusion is true for the density below the transition point, where some regions of the spin polarized ground state can be excited to the spin unpolarized state.

Based on these discussions, we propose: The ground state at the metallic side is the spin unpolarized liquid, while the ground state for the insulating side is spin-polarized. At the critical point of the metal-insulator transition, the system undergoes a spin unpolarized-polarized transition. Near the critical point, the spin polaron excitation, which causes the spatial inhomogeneous structure, is responsible for the observed strong metallic behavior. The picture is consistent with the percolation model [26]: the high conducting phase is the spin unpolarized phase, and the low conducting phase is spin polarized. In the following, we will show that the picture indeed reproduces the main experimental features.

4.2 Electron Distribution And Resistivity

The electron distribution of the system at a finite temperature can be calculated. The system is divided to three regions: spin unpolarized regions (u); spin polarized regions with $\xi \sim 1$ (p) and $\xi \sim -1$ ($\bar{p}$). For each region, the ground state energy per particle can be expanded near the local minimal points at $\xi = 0$ and $\xi = \pm 1$:

$$\begin{aligned}
\epsilon_u(n,\xi) &= \epsilon_u^0(n) + \frac{1}{2}\chi(n)\xi^2 + \cdots \\
\epsilon_p(n,\xi) &= \epsilon^0(n) + \Delta_c(n) + B_0(n)(1-\xi) + \cdots \\
\epsilon_{\bar{p}}(n,\xi) &= \epsilon^0(n) + \Delta_c(n) + B_0(n)(1+\xi) + \cdots
\end{aligned}$$

where Δ_c is the energy difference between the spin unpolarized and polarized states. B_0 and χ are the expanding coefficients depending on the density.

At the limit that each separated region is large, the interface energy between the different regions can be ignored, and the total energy of the system can be written

as,

$$\epsilon(n) = n_u \epsilon_u(n, \xi_p) + n_p \epsilon_p(n, \xi_p) + n_{\bar{p}} \epsilon_{\bar{p}}(n, \xi_{\bar{p}}) - B \sum_{i=u,p,\bar{p}} n_i \xi_i \,,$$

where B is an external in-plane magnetic field, and we set $g\mu_B = 1$. n_u, n_p and $n_{\bar{p}}$ are the number of the electrons at the corresponding regions, and ξ_u, ξ_p, $\xi_{\bar{p}}$ are the corresponding spin polarizations.

The entropy of the system can be calculated by counting the number of ways to distribute the electrons into three different regions:

$$s = k \left[n \ln n - \sum_{i=u,p,\bar{p};s=\uparrow,\downarrow} n_{is} \ln n_{is} \right]$$

where n_{is} is the number of electrons in each region with spin s.

The distribution can be calculated by minimizing the free energy $f = \epsilon - Ts$ under the constraint of a constant total electron number n. Introducing the new parameters: $n_u = (1-x)n$, $n_{p(\bar{p})} = xn(1 \pm \xi)/2$, $n_{i\uparrow(\downarrow)} = n_i(1 \pm \xi_i)/2$, the free energy can be minimized to x, ξ and ξ_i, where x is the fraction of the electrons in the spin polarized regions; $i = u, p, \bar{p}$. After some algebra, the distribution of the electrons at the finite temperature can be obtained,

$$\begin{aligned}
\xi_{p(\bar{p})} &= \tanh \frac{B \pm B_0}{kT} \,, \\
\xi_u &= \tanh \frac{B - \chi \xi_u}{kT} \,, \\
\xi &= \frac{\cosh \frac{B+B_0}{kT} - \cosh \frac{B-B_0}{kT}}{\cosh \frac{B+B_0}{kT} + \cosh \frac{B-B_0}{kT}} \,, \\
x &= \left\{ 1 + \frac{\cosh \frac{B-\chi\xi_u}{kT} \exp\left[\frac{\Delta_c + B_0 + \frac{1}{2}\chi\xi_u^2}{kT} \right]}{\cosh \frac{B+B_0}{kT} + \cosh \frac{B-B_0}{kT}} \right\}^{-1} .
\end{aligned} \tag{4.2}$$

Many experimental findings can be reproduced by some simple calculations. First, at low temperatures and without an in-plane magnetic field, the result can be approximately written as,

$$x \approx 2 \cosh \frac{B_0}{kT} \exp\left(-\frac{\Delta_c + B_0}{kT} \right) \approx \exp\left(-\frac{\Delta_c}{kT} \right) .$$

It can be seen that the distribution of the electrons exhibits an energy gap Δ_c, which is indeed the energy difference between the spin unpolarized and spin polarized states, as found in the experiments [80].

When the magnetic field is presence, we have $\xi_u \approx B/(\chi + kT)$, and

$$x \approx \frac{\cosh \frac{B}{kT}}{\cosh \frac{B}{\chi+kT}} \exp\left(-\frac{\Delta_c}{kT}\right)$$

For a weak magnetic field, the energy gap only depends weakly on the magnetic field. Such behavior is indeed observed in the experiments [80].

Supposing that the size of each separated region is large such that the quantum effect of the transport between different regions can be ignored, the resistivity of the system can be calculated by using a classical percolation model. The system is then mapped onto a random resistance network with three kinds of resistances (R_u, R_p, $R_{\bar{p}}$), which are corresponding to the three different regions. The occurrence probability of each resistance is determined by Eq. 4.2. The local resistivity of each region is supposed to be a function of its polarization,

$$\rho(\xi) \approx \rho_0(1 + \alpha\xi^2 + \cdots),$$

There are no odd order terms about ξ because the local resistivity is independent of the sign of the polarization. α is positive since the spin polarized region has higher local resistivity. In the following calculation, we omit the higher order terms of ξ.

Figure 4.2 shows the temperature dependence of the resistivity under different in-plane magnetic field strengths for a system which is metallic at zero magnetic field. The magnetic field polarizes the electron spins, and drives the system into the insulating phase. The critical field B_c is approximately Δ_c ($1.12\Delta_c$ in this case). We found that the temperature dependence of the resistivity can be well fitted by Eq. 4.1 before the magnetic field drives them into an insulating state. For a weak magnetic field, $\Delta \approx \Delta_c - \beta B^2$, and ρ_1 can be well fitted by equation $\rho_1(0)[1 - (B/\Delta_c)^2]$, which has no arbitrary parameter. The fitting of ρ_1 is consistent with the recent experiment [80].

When the system is driven into the insulating side, it can be seen that the resistivity saturates at low temperatures due to the full polarization of spins. From Eq. 4.2, we have $\xi_p = \tanh[(B+B_0)/kT]$. The saturation temperature is $T_s \sim B+B_0$, which linearly increases with an in-plane magnetic field. The similar behavior is observed in the experiment on the p-GaAs/AlGaAs samples [80].

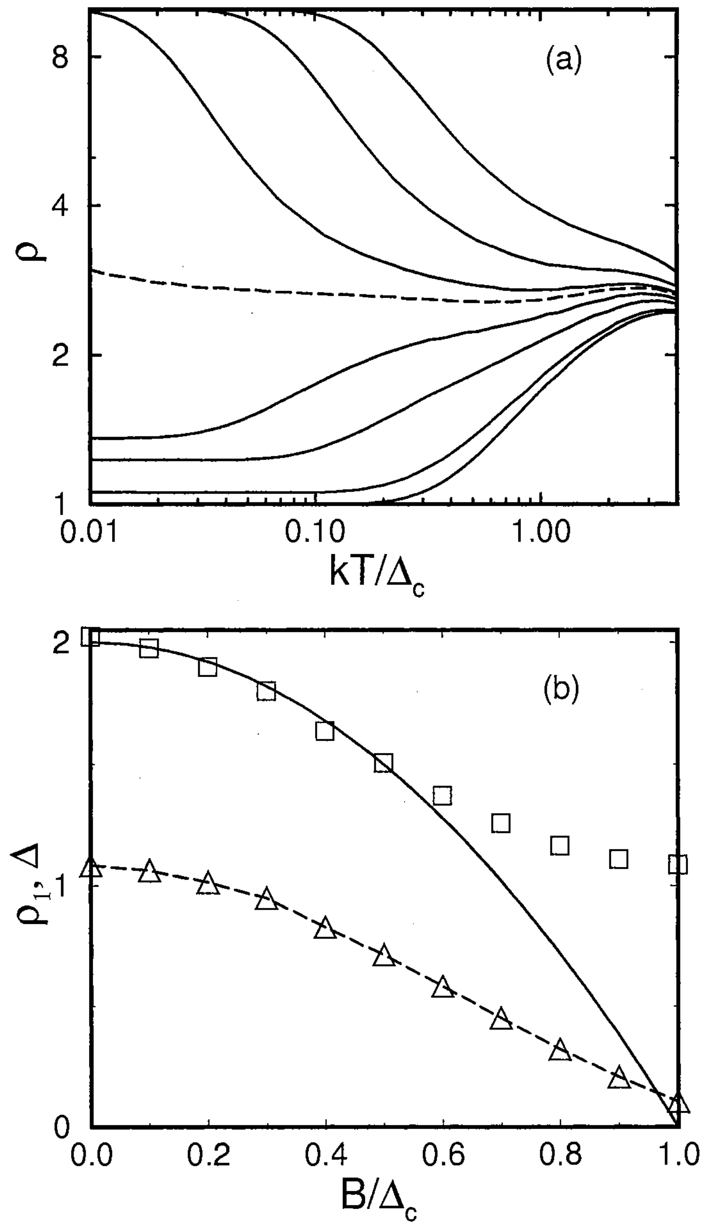

Figure 4.2. (a) The temperature dependence of the resistivity for different in-plane magnetic field strengths. From bottom to top, the field strengths are B/Δ_c = 0.0, 0.4, 0.8, 1.0, 1.12, 1.2, 1.4, 1.6. $\rho_0 = 1$, $\alpha = 9$, $\chi = 5$, $B_0 = 5$. (b) The parameters to fit the data with Eq. 4.1. Squares are for ρ_1, Triangles are for Δ. Solid line is the function $\rho_1(0)[1-(B/\Delta_c)^2]$. Dashed line is just a guide line.

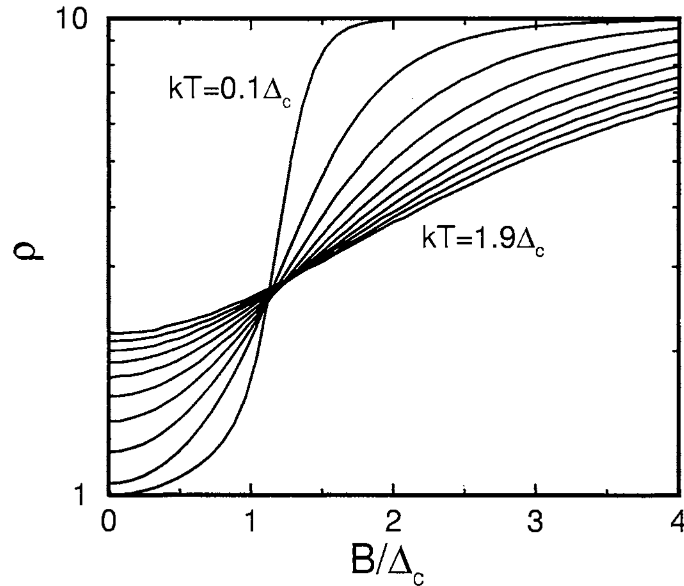

Figure 4.3. The resistivities depending on the in-plane magnetic field for different temperatures. $T = 0.1,\ 0.3,\ \cdots,\ 1.9$. The other parameters are the same as in Fig. 4.2.

Figure. 4.3 shows the resistivities depending on the in-plane magnetic field for different temperatures. For a weak magnetic field, the resistivity has the dependence $\rho \sim B^2$, as seen in experiments [81]. The behavior can be easily expected from the theory: the resistivity of system under the weak magnetic field is determined by the resistivity of the spin unpolarized regions, and $\xi_u \sim B$, $\rho \approx \rho_0(1 + \alpha\xi_u^2) \sim B^2$.

A crossover point, which is corresponding to the dashed line in Fig. 4.2(a), can be identified. The similar crossing point is also found in the experiments, and is identified as the critical magnetic fields [33]. The resistivity saturates at high magnetic field. The saturation magnetic field is different from the the critical field. This is the result of the percolation model: the system enters into insulating state if the fraction of the low conducting phase exceeds the percolation threshold.

4.3 Discussions and Summary

Before summary, we like to make few comments:

(i) We assume that the local resistivity is a function of the spin polarization. The assumption is reasonable since the spin correlation between the electrons prevents the electrons from hopping between sites. Further theoretical works is required to justify the assumption.

(ii) We suppose that the resistivity of the system can be calculated by using the classical percolation model. To make the assumption valid, it requires the size of each separated region is larger than the phase coherence length of the electrons. Some recent experiments do suggest that the strong metallic behavior occurs at the regime where the quantum effect is less important [41].

(iii) To have the spin polaron excitation, the spin polarization dependence of the ground state energy per particle should have the local minimal points at $\xi = \pm 1$. However, the QMC results indicate that the density regime satisfying the condition is very narrow ($r_s = 24.5 - 26.5$ for the QMC result we used) [82]. This could be an issue to our model. On the other hand, the energy scale involved is so small that much higher accuracy is required to get a conclusive answer from the QMC calculations.

(iv) In this study, we ignore the disorder effect. For the system that the disorder is important, such as Si MOSFETs, the density wave excitation may be more favorable than the spin polaron excitation.

In summary, we proposed the spin polaron excitation as a possible excitation state of the dilute 2D electron systems. The picture can easily explain the experimental fact that the energy gap between the ground state and the excited states is the same as the energy needed to polarize the electron spins. The temperature dependence of the resistivity can be understood as the effect of the spin polaron excitation. The theory provides a unified picture to understand the temperature dependence and magnetic field dependence.

BIBLIOGRAPHY

1. E. Abrahams, P.W. Anderson, D.C. Licciardello, T.V. Ramakrishnan, Phys. Rev. Lett. **42**, 673 (1979).

2. D.J. Thouless, Phys. Rep. **13C**, 93 (1974).

3. A. MacKinnon, B. Kramer, Phys. Rev. Lett. **47**, 1546 (1981).

4. G.J. Dolan, D.D. Osheroff, Phys. Rev. Lett. **43**, 721 (1979).

5. D.J. Bishop, D.C. Tsui, R.C. Dynes, Phys. Rev. Lett. **44**, 1153 (1980).

6. B. Tanatar, D.M. Ceperley, Phys. Rev. B **39**, 5005 (1989).

7. E. Abrahams, S.V. Kravchenko, M.P. Sarachik, Rev. Mod. Phys. **73**, 251 (2001).

8. S.V. Kravchenko, G.V. Kravchenko, J.E. Furneaux, V.M. Pudalov, and M. D'Iorio, Phys. Rev. B **50**, 8039 (1994).

9. S.V. Kravchenko, W.E. Mason, G.E. Bowker, J.E. Furneaux, V.M. Pudalov, and M. D'Iorio, Phys. Rev. B **51**, 7038 (1995).

10. V.M. Pudalov, JETP Lett. **66**, 175 (1997).

11. W. Mason, S.V. Kravchenko, G.E. Bowker, J.E. Furneaux, Phys. Rev. B **52**, 7857 (1995).

12. A.L. Efros and B.I. Shklovskii, J. Phys. C **8**, L49 (1975).

13. S.I. Khondaker, I. S. Shlimak, J.T. Nicholls, M. Pepper, D.A. Ritchie, Phys. Rev. B **59**, 4580 (1999).

14. M.P. Sarachik, S.V. Kravchenko, Proc. Natl. Acad. Sci. USA **96**, 5900 (1999).

15. S.V. Kravchenko, T. M. Klapwijk, Phys. Rev. Lett. **84**, 2909 (2000).

16. D. Popovic, A.B. Fowler, S. Washburn, Phys. Rev. Lett. **79**, 1543 (1997).

17. P.T. Coleridge, R.L. Williams, Y. Feng, P. Zawadzki, Phys. Rev. B **56**, R12764 (1997).

18. J. Lam, M. D'Iorio, D. Brown, H. Lafontaine, Phys. Rev. B **56**, R12741 (1997).

19. Y. Hanein, U. Meirav, D. Shahar, C.C. Li, D.C. Tsui, H. Shtrikman, Phys. Rev. Lett. **80**, 1288 (1998).

20. M.Y. Simmons, A. R. Hamilton, M. Pepper, E. H. Linfield, P. D. Rose, D. A. Ritchie, A. K. Savchenko, and T. G. Griffiths, Phys. Rev. Lett. **80**, 1292 (1998).

21. J. Yoon, C.C. Li, D. Shahar,D.C. Tsui, M. Shayegan, Phys. Rev. Lett. **82**, 1744 (1999).

22. Jr. A.P. Mills, A.P. Ramirez, L.N. Pfeiffer, K.W. West, Phys. Rev. Lett. **83**, 2805 (1999).

23. S.J. Papadakis, M. Shayegan, Phys. Rev. B **57**, R15068 (1998).

24. Y. Hanein, D. Shahar, J. Yoon, C.C. Li, D.C. Tsui, H. Shtrikman, Phys. Rev. B **58**, R13338 (1998).

25. S.V. Kravchenko, D. Simonian, M.P. Sarachik, Phys. Rev. Lett. **77**, 4938 (1996).

26. S. He, X.C. Xie, Phys. Rev. Lett. **80**, 3324 (1998).

27. S.L. Sondhi, S.M. Girvin, J.P. Carini, D. Shahar, Rev. Mod. Phys. **69**, 315 (1997).

28. R. Heemskerk, T.M. Klapwijk, Phys. Rev. B **58**, R1754 (1998).

29. V. Senz, U. Dyotsch, U. Gennser, T. Ihn, T. Heinzel, K. En- sslin, R. Hartmann, D. and Gryutzmacher, Ann. Phys. (Leipzig) **8**, 237 (1999).

30. D. Simonian, S.V. Kravchenko, M.P. Sarachik, V.M. Pudalov, Phys. Rev. Lett. **79**, 2304 (1997).

31. V.M. Pudalov, G. Brunthaler, A. Prinz, B. Bauer, JETP Lett. **65**, 932 (1997).

32. K.M. Metres, M.D. Simonia, M.P. Sarachik, S.V. Kravchenko, T.M. Klapwijk, Phys. Rev. B **60**, R5093 (1999).

33. J. Yoon, C.C. Li, D. Shahar, D.C. Tsui, M. Shayegan, Phys. Rev. Lett. **84**, 4421 (2000).

34. T. Okamoto, K. Hosoya, S. Kawaji, A. Yagi, Phys. Rev. Lett. **82**, 3875(1999).

35. S.A. Vitkalov, H. Zheng, K.M. Metres, M.P. Sarachik, T.M. Klapwijk, Phys. Rev. Lett. **85**, 2164 (2000).

36. C. Dultz, H.W. Jiang, Phys. Rev. Lett. **84**, 4689 (2000).

37. J.P. Eisenstein, L.N. Pfeiffer, K.W. West, Phys. Rev. Lett. **68**, 674 (1992).

38. J.P. Eisenstein, L.N. Pfeiffer, K.W. West, Phys. Rev. B **50**, 1760 (1994).

39. S. Ilani, A. Yacoby, D. Mahalu, H. Shtrikman, preprint, cond-mat/9910116.

40. S. Ilani, A. Yacoby, D. Mahalu, H. Shtrikman, Science **292**, 1354 (2001).

41. M.Y. Simmons, A.R. Hamilton, M. Pepper, E.H. Linfield, P.D. Rose, D.A. Ritchie, Phys. Rev. Lett. **84**, 2489 (2000).

42. B.L. Altshuler, D. Khmel'nitzkii, A.I. Larkin, P. A. Lee, Phys. Rev. B **22**, 5142 (1980).

43. G. Brunthaler, A. Prinz, G. Bauer, V.M. Pudalov, Phys. Rev. Lett. **87**, 096802 (2001).

44. V. Dobrosavljevic, E. Abrahams, E. Miranda, S. Chakravarty, Phys. Rev. Lett. **79**, 455 (1997).

45. S. Chakravarty, L. Yin, E. Abrahams, Phys. Rev. B **58**, 559 (1998).

46. S. Chakravarty, S. Kivelson, C. Nayak, K. Voelker, Philos. Mag. B **79**, 859 (1999).

47. S.T. Chui, B. Tanatar, Phys. Rev. Lett. **74**, 458 (1995).

48. P. Phillips, Y. Wan, I. Martin, S. Knysh, D. Dalidovich, Nature, **395**, 253 (1998).

49. D. Belitz, T.R. Kirkpatrick, Phys. Rev. B **58**, 8214 (1998).

50. J.S. Thakur, D. Neilson, Phys. Rev. B **58**, 13717 (1998).

51. A.M. Finkelstein, Z. Phys. B **56**, 189 (1984).

52. C. Castellani, C. Di Castro, P.A. Lee, Phys. Rev. B **57**, R9381 (1998).

53. Q. Si, C.M. Varma, Phys. Rev. Lett. **81**, 4951 (1998).

54. G. Benenti, X. Waintal, J.-L. Pichard, Phys. Rev. Lett. **83**, 1826 (1999).

55. P.J.H. Denteneer, R.T. Scalettar, N. Trivedi, Phys. Rev. Lett. **83**, 4610 (1999).

56. T.M. Kalwijk, S. Das Sarma, Soild State Commun. **110**, 581 (1999).

57. S. Das Sarma, E.H. Hwang, Phys. Rev. Lett. **84**, 5596 (2000).

58. Y. Meir, Phys. Rev. Lett. **83**, 3506 (1999).

59. E. Chow, H.P. Wei, S.M. Girwin, M. Shayegan, Phys. Rev. Lett. **77**, 1143 (1996).

60. A. Ishihara, *Solid State Physics*, edited by H. Ehrenreich and D. Turnbull (Academic, New York, 1989), Vol.42 p.271.

61. G. Meissner, H. Namaizawa, M. Voss, Phys. Rev. B **13**, 1370 (1975).

62. H.-K. Sim R. Tao, F.Y. Wu, Phys. Rev. B **34**, 7123 (1986).

63. K.-H. Ahn, K. Richter, I.-H. Lee, Phys. Rev. Lett. **83**, 4144 (1999).

64. Y. Wang, J. Wang, H. Guo, E. Zarembar, Phys. Rev. B **52**, 2738 (1995).

65. B. derrida, J. Vannimenus, J. Phys. A **15**, L557 (1982).

66. G. Brunthaler, A. Prinz, G. Bauer, V.M. Pudalov, E.M. Dizhur, J. Jaroszynski, P. Gold, T. Dietl, preprint cond-mat/9911011.

67. P. Mohanty, E.M.Q. Jariwala, R.A. Webb, Phys. Rev. Lett. **78**, 3366 (1997).

68. P. Mohanty, R.A. Webb, Phys. Rev. B **55**, R13452 (1997).

69. B.S. Andereck, E. Abrahams, *Physics in One Dimension*, edited by J. Bernasconi and T. Schneider (Springer-Verlag, New York, 1981).

70. M. Büttiker, Phys. Rev. B **33**, 3020 (1986).

71. S. Datta, *Electronic Transport in Mesoscopic Systems* (Cambridge University, Cambridge, England, 1995).

72. Y. Shapir, Y. Aharony, A.B. Harris, Phys. Rev. Lett. **49**, 486 (1982).

73. Y. Gefen, D.J. Thouless, Y. Imry, Phys. Rev. B **28**, 6677 (1983).

74. Y. Meir, A. Aharony, A.B. Harris, Europhys. Lett. **10**, 275 (1989).

75. Iksoo *et. al.*, Phys. Rev. Lett. **74**, 2094 (1995).

76. H. Haug, A.P. Jauho, *Quantum Kinetics in Transport and Optics of Semiconductors*, (Springer, 1996).

77. A. MacKinn and B. Kramer, Z. Phys. B **53**, 1 (1983).

78. M.N. Barber, *Phase Transitions and Critical Phenomena*, edited by C. Domb and M.S. Green, Vol. **8**, (Academic Press, London), 1983, p.145.

79. P.A. Lee, T.V. Ramakrishnan, Rev. Mod. Phys. **57**, 287 (1985).

80. Xuan P.A. Gao *et.al.*, preprint, cond-mat/0110571; preprint, cond-mat/0110608.

81. V. M. Pudalov, M. E. Gershenson, H. Kojima, preprint, cond-mat/0201001.

82. C. Attaccalite *et.al.*, preprint, cond-mat/0109492 and the references therein.

VITA

Junren Shi

Candidate for the Degree of

Doctor of Philosophy

Thesis: TWO-DIMENSIONAL METAL-INSULATOR TRANSITION

Major Field: Physics

Biographical:

Personal Data: Born in Fuding, Fujian of P.R. China on Febuary 28, 1972.

Education: Received Bachelor of Science degree in Physics from Fujian Normal University, Fuzhou, Fujian, China in July 1993; Completed the requirements for the Doctor of Philosophy degree with a major in Physics at Oklahoma State University in May 2002.